UNIVERSIDAD POLITÉCNICA DE VALENCIA

DEPARTAMENTO DE INGENIERÍA QUÍMICA Y NUCLEAR

Improving mechanical properties and microstructure development of fiber reinforced ceramic nuclear fuel

TESIS DOCTORAL

Presentada por:

Hesdras Henrique Sacramento Santana

Dirigida por:

Prof. Dr. I. I. José Ródenas Diago

Valencia, abril 2014

“Confia no Senhor de todo o teu coração e não te estribes no teu próprio entendimento.

Reconhece-o em todos os teus caminhos e Ele endireitará as tuas veredas.” Provérbios 3: 5 e 6

Agradecimentos

Quando o grande rei e salmista Davi se apresentou pra enfrentar o gigante Golias, ele proferiu algumas palavras que hoje eu tomo pra mim: “O Senhor me livrou das mãos do leão e do urso e também me livrará das mãos deste gigante”. Da mesma forma que Deus foi com Davi nestes três grandes desafios de sua vida, Ele também foi comigo em três desafios da minha vida, a saber graduação em engenharia mecânica, mestrado em aplicações nucleares e por fim no doutorado de engenharia de materiais nucleares. Confesso que se não fora o Senhor eu hoje não estaria terminando este arduo trabalho. Se não fosse o incentivo e ajuda do Espírito Santo de Deus eu já teria desistido. Somente Ele com a Sua sabedoria veio a me dar todo suporte pra realização de todo este trabalho.

Certamente a Seu suporte veio através de diversas pessoas como por exemplo o Professor Dr. José Ródenas que me orientou em todo este trabalho com muito afinco e dedicação. Seus conselhos e sugestões para o trabalho foram fundamentais para o seu desenvolvimento e término. Agradeço também aos senhores Dr. Wolfgang Dörr e Dr. Volker Lansmann e a senhora Dr. Petra Hoffmann pela oportunidade de desenvolver os trabalhos nos laboratórios da empresa AREVA NP GmbH em Erlangen, Alemanha. Ao senhores Georg Maier, Gerhard Gradel, Dr. Martin Zemek pelas orientações e discussões para o desenvolvimento dos experimentos e análises dos resultados. Aos técnicos de laboratório, Norbert Bergmann, Pia Reichel, Karl Gößwein, Gerhard Gumbert pelas instruções técnicas e também pelos momentos de descontração! Aos colegas e amigos Juliane Vidal e Eduardo Vera Garcia pelas palavras de incentivo, pelos momentos de descontração fora da AREVA e pelas discussões para melhoria do trabalho.

Quero agradecer também aos irmãos e amigos conquistados nestes últimos anos. Pessoas que me amaram e ainda me amam que tem muita importancia pra minha vida.

Aos meus amados pais Dilson e Jandira Santana e minhas amadas irmãs Myrtes e Flávia Santana por sempre me apoiarem e incentivarem nestes anos de trabalho. Muito obrigado por vossas orações e palavras de amor, saibam que elas sempre terão valor por toda a minha vida!

Por fim agradeço as minhas duas preciosidades, Bianca e Isabel Santana. Elas são pra mim hoje um grande apoio na vida. Me incentivaram, apoiaram, entenderam quando não podia em alguns momentos lhe dar a devida atenção por precisar terminar de escrever este trabalho. Muito obrigado meus amores!

Obrigado Deus pela minha família!

Acknowledgements

When the great king and psalmist David confronted Goliath, he spoke a few words that I take today to claim for myself, " The Lord who delivered me from the mouth of the lion and the bear will deliver me same way from the hand of the giant". As God has been with David in these three major challenges of his life, he has also been with me in the following three challenges of my life, namely the degree in engineering, master's degree in nuclear applications, and finally at the PhD in nuclear materials technology. I confess that if the Lord had not intervened, I wouldn't have been able to complete this hard job today. If the encouragement and help of the Holy Spirit of God would not have been present, I would have long given up.

He was the one who stood with his wisdom at my side to accomplish this work and to give me all his support.

Surely came His support by the intervention of several people such as Professor Dr. José Ródenas, who has been orientating me with devotion during the whole process. His advices and suggestions for the work were critical to the development and completion. I also thank Dr. Wolfgang Dörr, Dr. Volker Lansmann and Dr. Petra Hoffmann for the opportunity to work at the laboratory of AREVA NP GmbH, Erlangen, Germany. Thanks also to Mr. Georg Maier, Gerhard Gradel and Dr. Martin Zemek for orientation and discussions for the development of experiments and analysis of results.

Thanks to the laboratory technicians Norbert Bergmann, Pia Reichel, Karl Gößwein and Gerhard Gumbert, too for the technical instructions and also for moments of relaxation. Also thanks to the colleagues and friends Juliane Vidal and Eduardo Vera for the words of encouragement, for moments of relaxation outside of AREVA and for the talks to improve the job.

I also want to thank the friends and brethreen that I have won in recent years . People who have loved me and still love me. They are of great importance for my life.

My beloved parents Dilson and Jandira Santana and my beloved sisters Myrtes and Flávia Santana, who have always supported and encouraged me during these years of work. Thank you for your prayers and for the words of love. Know that they will always be precious in my life.

Finally, I thank my two treasures Bianca and Isabel Santana. Today, they are a great support for me and my life. They encouraged, supported and understood me as I sometimes could not pay due attention because I had you finish this work . Thank you, my Beloved onces!

I thank God for my family !

Danksagung

Als der großer König und Psalmist David sich den Riesen Goliath stellte, sprach er ein paar Worte, die ich heute für mich in Anspruch nehme: "Der Herr, der mich aus dem Rachen des Löwen und des Bären errettete wird mich aus der Hand des Riesen ebenfalls erretten". Gleichermaßen wie Gott mit David in diesen drei großen Herausforderungen seines Lebens gewesen ist, ist Er auch mit mir in den folgenden drei Herausforderungen meines Lebens gewesen, nämlich bei dem Abschluss in Maschinenbau, Master-Abschluss in Kernanwendungen und schließlich bei der Promotion in Kernmaterial Technik. Ich gestehe, dass wenn der Herrn nicht eingegriffen hätte, würde ich heute diese harte Arbeit nicht abschließen können. Wenn die Ermutigung und Hilfe des Heiligen Geistes Gottes nicht präsent gewesen wäre, hätte ich längst aufgegeben.

Allein Er mit seiner Weisheit stand mir bei um mir seine ganze Unterstützung zu geben um diese Arbeit zu realisieren. Sicherlich Seine Unterstützung kam durch mehrere Personen zustande, wie zum Beispiel Professor Dr. José Ródenas, der mich während dieser harte Arbeit mit Hingabe orientierte. Seine Hinweise und Anregungen für die Arbeit waren entscheidend für die Entwicklung und Fertigstellung. Ich danke auch Herrn Dr. Wolfgang Dörr, Dr. Volker Lansmann und Frau Dr. Petra Hoffmann für die Gelegenheit, die Arbeit im Labor der Firma AREVA NP GmbH, Erlangen, Deutschland zu erledigen. Dank auch an Herr Georg Maier, Herr Gerhard Gradel und Dr. Martin Zemek für die Orientierung und Diskussionen für die Entwicklung von Experimenten und Analyse der Ergebnisse.

Ein Dank an die Laboranten Norbert Bergmann, Pia Reichel, Karl Gößwein und an Gerhard Gumbert für die technischen Anweisungen und auch durch Momente der Entspannung. Den Kollegen und Freunde Juliane Vidal und Eduardo Vera für die Worte der Ermutigung, für Momente der Entspannung außerhalb von AREVA und für die Gespräche zur Verbesserung der Arbeit auch ein großes Dankeschön. Ich möchte auch den Freunden und Geschwistern, die ich in den letzten Jahren gewonnen habe danken. Menschen, die mich geliebt haben und immer noch lieben. Sie sind von großer Bedeutung für mein Leben.

Meinen geliebten Eltern Dilson und Jandira Santana und meine geliebten Schwestern Myrtes und Flavia Santana, die mich immer unterstützt und ermutigt haben während diesen Jahren der Arbeit. Vielen Dank für eure Gebete und für die Worte der Liebe. Wisst, dass sie immer wertvoll für mein Leben sein werden.

Schließlich danke ich meinen beiden Schätzen Bianca und Isabel Santana . Sie sind heute für mich eine große Stütze im Leben. Sie ermutigten, unterstützten und verstanden mich als ich Ihnen manchmal nicht die gebührende Aufmerksamkeit widmen könnte weil ich diese Arbeit beenden musste. Vielen Dank, meine Liebten !

Ich danke Gott für meine Familie !

Resumen

En el presente trabajo se ha estudiado y analizado ampliamente el proceso de producción de pastillas de combustible de UO_2. Los objetivos de esta investigación fueron comprender y analizar la influencia de diferentes aditivos y la variación de los pasos del proceso de producción sobre la microestructura y por consiguiente en la resistencia mecánica de la pastilla de combustible nuclear.

Por otra parte, se pretende también una mejora de las características cualitativas de las pastillas de combustible cerámico. Para este propósito, se produjeron las pastillas de UO_2 sin aditivos, las llamadas pastillas estándar, las pastillas que contienen como aditivo AZB (Azodicarbonamida), U_3O_8 negro (de uranio oxidado de las pastillas de chatarra - OS), U_3O_8 verde (polvo de uranio oxidado - OP), o fibras queratínicas (un aditivo no convencional).

La introducción de estos aditivos en la mezcla de polvo de UO_2 antes o después de la etapa de granulación y en diferentes concentraciones, produjo varias configuraciones de microestructura. Como no sería posible analizar todas las configuraciones, durante los pre-tests de investigación se separaron algunos para estudiarlos con más detalle.

Las pastillas con AZB añadido después de la granulación presentan granos más grandes y mayores poros que aquellas con el AZB añadido antes de la granulación, así como granos libres de poros y una estructura granulada en lugar de homogénea. Las pastillas con OS presentan una porosidad fina distribuida en toda la matriz de la pastilla con algunos grupos de porosidad, mientras las pastillas que contienen OP muestran en su matriz una porosidad aglomerada en forma de ganchos. En cuanto al tamaño de grano, se puede observar una distribución más uniforme del tamaño de grano en las pastillas de OS que en las pastillas con OP.

Las variaciones en la cantidad de fibras de queratina añadidas, tiempo de permanencia en la sinterización y densidad de las pastillas verdes dan lugar a diferentes microestructuras. Sin embargo, se observaron algunas características comunes entre ellas, tales como la presencia de poros alargados, grupos de porosidad y granos más grandes situados en los bordes de las pastillas, mientras que los más pequeños se concentraron más en la parte central de la pastilla. Esta distribución de los granos se identificó como estructura bi-modal.

Los aspectos de la microestructura mencionados tienen ciertamente influencia en las propiedades

mecánicas de la pastilla de combustible. Sin embargo, los parámetros de sinterización, la densidad de la pastilla verde y sinterizada y las dimensiones de las pastillas también tienen influencia en las características mecánicas de las pastillas. Para el estudio de la influencia de todos estos parámetros sobre las propiedades mecánicas de las pastillas se utilizaron cuatro procedimientos de ensayo: el denominado "squirrel-cage", donde se probó la resistencia mecánica de las pastillas no sinterizadas mediante choques mecánicos; la prueba de compresión diametral ("Brazilian Test") donde se estudió la resistencia de las pastillas sinterizadas y no sinterizadas; la "Vickers indentation technique", y el ensayo de fluencia donde se analizó la plasticidad de las pastillas, a temperatura ambiente y elevada, respectivamente.

Los resultados de la "squirrel-cage" mostraron que las pastillas con fibras de queratina eran mucho más resistentes mecánicamente que las pastillas sin ella, lo que significa que las fibras de queratina actuaron, antes de la sinterización, como un polvo aglutinante aumentando la cohesión entre los granos de polvo y proporcionando a las pastillas verdes mayor resistencia mecánica contra impactos.

El "Brazilian Test" evaluó la influencia de la longitud de la pastilla frente a su diámetro (relación L/D), la influencia de diferentes aditivos mezclados con el polvo de UO_2 y los diferentes procesos de producción de pastillas. El análisis la influencia de L/D mostró que si se fija el diámetro de las pastillas y se aumenta la longitud, también aumentará el módulo de Weibull (una medida de la fiabilidad del lote de pastillas). Mediante la comparación de las pastillas con OS, OP y $0,3\,\%$ de fibras de queratina se observó que las pastillas con OS presentan el mayor volumen de poros de menos de $10\,\mu m$, mientras las pastillas con OP y queratina presentan el mayor volumen de poros más grandes de $20\,\mu m$. Parece que esta relevante característica favorece el más alto valor de la fuerza Weibull en pastillas con OS.

En el test de "Vickers indentation", se probaron pastillas estándar, pastillas con OS y pastillas con fibras de queratina. Los resultados mostraron que la dureza calculada para las pastillas estándar es ligeramente inferior en comparación con los valores obtenidos para las pastillas con fibras de queratina. También las pastillas que contienen OS tienen en la mayoría de los casos, una dureza inferior en comparación con las pastillas con fibras de queratina. La resistencia a la fractura calculada y los valores de la energía superficial de fractura muestran también un mejor comportamiento mecánico para las pastillas con fibra de queratina que para las estándar.

Las pastillas estándar, las que tienen un $30\,\%$ OP, con el tamaño más pequeño de grano, las pastillas con fibras de queratina, con estructura bi-modal y las pastillas con óxido de cromo, con el tamaño de grano más grande, se ensayaron en el horno de fluencia. Los resultados mostraron que todas las pastillas con aditivos presentan un mejor comportamiento de fluencia que las pastillas estándar. Entre las pastillas preparadas con aditivos la comparación mostró claramente que bajo tensiones inferiores las pastillas con granos más pequeños tienen una mejor tasa de fluencia. Al aumentar las tensiones aplicadas se observa una mejora de la velocidad de fluencia de las pastillas con óxido de cromo y fibra de queratina incluso superando ligeramente a las pastillas con 30 % OP en el esfuerzo más alto aplicado.

Abstract

At the present work the UO_2 fuel production process was extensively studied and analyzed. The objectives of such investigation were to understand and analyze the influence of different additives and the variation of the production process steps on the microstructure and consequently in the mechanical strength of the nuclear fuel pellet.

Moreover, an improvement of the qualitative characteristics of the ceramic fuel pellets was also aimed. For this purpose UO_2 pellets without additives, the so-called standard pellets, pellets containing as additive for example AZB (Azodicarbonamid), black U_3O_8 (Oxidized uranium pellet scrap - OS), green U_3O_8 (Oxidized uranium powder - OP), keratin fibers (a non conventional additive) were produced.

The introduction of these additives to the UO_2 powder mixture prior or after the granulation production step and in different concentrations produced several microstructure configurations. As it would not be possible to analyze all of them here so during the investigation pre-tests some of them were separated to be studied in more detail.

Pellets with AZB added after the granulation presented larger grains and larger pores than those with AZB added before granulation, also porosity free grains and a granulate structure instead of a homogeneous one. Pellets with OS present fine porosity distributed all over the pellet matrix with some porosity clusters whereas pellets containing OP show in its matrix porosity agglomerated in form of hooks. As for the grain size, a more uniform grain size distribution can be observed in pellets OS than in pellets with OP.

The variations in the amount of keratin fibers added, sintering dwell time and green density resulted indeed in different microstructures. Nevertheless, some common characteristics among them were observed such as the presence of elongated pores, porosity clusters and larger grains located at the pellets borders while the smaller ones were concentrated more in the central part of the pellet. This distribution of grains was identified as bi-modal structure.

The mentioned microstructure aspects certainly influence on the mechanical properties of the fuel pellet. However, the sintering parameters, the green and final pellet density and the pellet dimensions also have an influence on the mechanical characteristics of the pellets. For studying the influence of all these parameters on the pellet mechanical properties four testing procedures

were utilized the so-called squirrel-cage where the mechanical resistance of the not sintered pellets against mechanical shocks was tested, the diametrical compression test (Brazilian Test) where the strength of sintered and not sintered pellets was studied, the Vickers indentation technique and the creep test where the pellet plasticity respectively at room and at elevated temperatures was analyzed.

The squirrel-cage results showed that the pellets with keratin fibers were much more mechanically resistant than those pellets without it, which means that the keratin fibers acted, prior sintering, as a powder binder increasing the cohesion among the powder granules proportionating the green pellets higher mechanical resistance against impacts.

The Brazilian test evaluated the influence of the pellet length to the pellet diameter (L/D ratio), the influence of different additives mixed to the UO_2 powder and the different pellet production processes. The L/D influence analysis showed that if one fixes the pellet diameter and increase the pellet length the Weibull modulus (here a measure of the pellet lot reliability) will also increase. By comparing pellets with OS, OP and 0.3% keratin fibers it was observed that pellets with OS presented the highest volume of pores smaller than $10\,\mu m$ while pellets with OP and keratin presented the highest volume of pores larger than $20\,\mu m$. It seems that this relevant characteristic favored to the highest Weibull strength value for pellets with OS.

In the indentation test standard pellets, pellets with OS and pellets with keratin fibers were tested. The results showed that the calculated hardness for the standard pellets is slightly lower when compared to the values obtained by the pellets with keratin fibers. Also the pellets containing OS when compared to the keratin fibers pellets have in most of the cases a lower hardness. The calculated fracture toughness and fracture surface energy values show also a better mechanical behavior for the keratin fibre pellets than in the standard pellets.

Standard pellets, pellets with $30\%\,OP$, which had the smallest grain size, pellets with keratin fibers, having the bi-modal structure and pellets with chromium oxide, which had the largest grain size, were tested in the creep furnace. The results showed that all pellets with additives presented a better creep behavior than the standard pellets. Among the pellets prepared with additives the comparison clearly showed that under lower stresses pellets with smaller grains have a better creep rate. By increasing the applied stresses we observe an improvement of the creep rate of the pellets with chromium oxide and keratin fibre even slightly overcoming the pellets with $30\%\,OP$ at the highest applied stress.

Resum

En el present treball s'ha estudiat i analitzat àmpliament el procés de producció de pastilles de combustible d'UO_2. Els objectius d'esta investigació foren comprendre i analitzar la influència de distints additius i la variació de les etapes del procés de producció en la microestructura y, per tant, en la resistència mecànica de la pastilla de combustible nuclear.

Per altra banda, també es pretén aconseguir una millora de les característiques qualitatives de les pastilles de combustible ceràmic. Per a este propòsit, s'han produït pastilles d'UO_2 sense additius, anomenades pastilles estàndard, pastilles que contenen com a additiu AZB (Azodicarbonamid), U_3O_8 negre (d'urani oxidat de pastilles de deixalla - OS), U_3O_8 verd (pols d'urani oxidat-OP), o fibres queratíniques (un additiu no convencional).

La introducció d'estos additius en la mescla de pols d'UO_2 abans o després de la etapa de granulació i en diferents concentracions, ha produït distintes configuracions de microestructura. Com no és possible analitzar totes les configuracions, durant els pre-tests d'investigació s'han separat algunes per a estudiar-les amb més detall.

Les pastilles amb AZB afegit després de la granulació presenten grans de majors dimensions i porus més grans que aquelles amb AZB afegit abans de la granulació, així com grans lliures de porus i una estructura granulada en lloc d'homogènia. Les pastilles amb OS presenten una porositat fina distribuïda en tota la matriu de la pastilla amb alguns grups de porositat, mentre que les pastilles que contenen OP mostren en la matriu una porositat aglomerada en forma de ganxos. Pel que fa a les dimensions dels grans, es pot observar una distribució més uniforme de les dimensions del gra en les pastilles d'OS que en les pastilles amb OP.

Les variacions en la quantitat de fibres de queratina afegides, temps de permanència en la sinterització i densitat de les pastilles verdes donen lloc a diferents microestructures. No obstant això, s'observaren algunes característiques comunes entre elles, tals com la presència de porus allargats, grups de porositat i grans de majors dimensions situats en les vores de les pastilles, mentre que els més xicotets es van concentrar més en la part central de la pastilla. Esta distribució dels grans es va identificar com a estructura bi-modal.

Els aspectes de la microestructura esmentats tenen certament influència en les propietats mecàniques de la pastilla de combustible. No obstant això, els paràmetres de sinterització, la

densitat de la pastilla verda i sinteritzada i les dimensions de les pastilles també tenen influència en les característiques mecàniques de les pastilles. Per a l'estudi de la influència de tots estos paràmetres sobre les propietats mecàniques de les pastilles es van utilitzar quatre procediments d'assaig: el denominat "squirrel-cage", on es va provar la resistència mecànica de les pastilles no sinteritzades mitjançant xocs mecànics; la prova de compressió diametral ("Brazilian Test") on es va estudiar la resistència de les pastilles sinteritzades i no sinteritzades; la "Vickers indentation technique", i l'assaig de fluència on es va analitzar la plasticitat de les pastilles a temperatura ambient i elevada, respectivament.

Els resultats de la "squirrel-cage"van mostrar que les pastilles amb fibres de queratina eren molt més resistents mecànicament que les pastilles sense ella, la qual cosa significa que les fibres de queratina van actuar, abans de la sinterització, com una pols aglutinant augmentant la cohesió entre els grans de pols i proporcionant a les pastilles verdes major resistència mecànica contra impactes.

"Brazilian Test" va avaluar la influència de la longitud de la pastilla enfront del seu diàmetre (relació L/D), la influència de diferents additius barrejats amb la pols d'UO_2 i els diferents processos de producció de pastilles. L'anàlisi de la influència de L/D va mostrar que si es fixa el diàmetre de les pastilles i s'augmenta la longitud, també augmentarà el mòdul de Weibull (una mesura de la fiabilitat del lot de pastilles). Mitjançant la comparació de les pastilles amb OS, OP i $0,3\,\%$ de fibres de queratina es va observar que les pastilles amb OS presenten el major volum de porus de menys de $10\,\mu m$, mentre les pastilles amb OP i queratina presenten el major volum de porus més grans de $20\,\mu m$. Sembla que esta rellevant característica afavoreix el més alt valor de la força Weibull en pastilles amb OS.

En el test "Vickers indentation", es van provar pastilles estàndard, pastilles amb OS i pastilles amb fibres de queratina. Els resultats van mostrar que la duresa calculada per a les pastilles estàndard és lleugerament inferior, en comparació dels valors obtinguts per a les pastilles amb fibres de queratina. També les pastilles que contenen OS tenen en la majoria dels casos, una duresa inferior en comparació amb les pastilles amb fibres de queratina. La resistència a la fractura calculada i els valors de l'energia superficial de fractura mostren també un millor comportament mecànic per a les pastilles amb fibra de queratina que per a les estàndard.

Les pastilles estàndard, les que tenen un $30\,\%$ OP, amb la grandària més xicoteta de gra, les pastilles amb fibres de queratina, amb estructura bi-modal i les pastilles amb òxid de crom, amb la grandària de gra més gran, es van assajar en el forn de fluència. Els resultats van mostrar que totes les pastilles amb additius presenten un millor comportament de fluència que les pastilles estàndard. Entre les pastilles preparades amb additius la comparació va mostrar clarament que per a tensions inferiors les pastilles amb grans més xicotets tenen una millor taxa de fluència. En augmentar les tensions aplicades s'observa una millora de la velocitat de fluència de les pastilles amb òxid de crom i fibra de queratina fins i tot superant lleugerament a les pastilles amb 30 % OP en l'esforç més alt aplicat.

Contents

List of Figures

List of Tables

Nomenclature

α	Powder flowability index
$\bar{R}$	Gas constant [J/molK] (8,3144621 J/molK)
$\Delta l/l_0$	Linear thermal shrinkage or expansion
$\Delta L/t$	Change in compact length per time
$\dot{\varepsilon}$	Creep rate [mm/mm/h]
γ	Surface free energy [J/m^2]
μ	Powder to die-wall friction coefficient
$\phi_{(\rho)}$	MSC parameter depending on the density
π	Pi constant (=3,14159)
ρ	Density [g/cm^3]
ρ_0	Theoretical density
ρ_g	Green density
ρ_r	Relative density
σ	Normal stress [MPa]
σ_0	Weibull characteristic strength [MPa]
σ_B	Bottom punch stress [MPa]
σ_r	Radial stress [MPa]
σ_{sp}	Stress on a speherical particle [MPa]

σ_T	Top punch stress [MPa]
σ_t	Fracture threshold stress [MPa]
σ_z	Axial normal compaction stress [MPa]
τ_{xy}	Shear stress [MPa]
$\Theta(t, T(t))$	MSC parameter depending on time and temperature
D_p	Particle diameter [m]
F_i	Indentation load [N]
F_0	Punch force [N]
K_I	Mode I stress intensity factor
K_Ic	Fracture toughness
m_w	Weibull modulus
P_0	Average compaction pressure at the punch face [MPa]
P_B	Bottom punch stress [MPa]
p_r	Particle radius [m]
P_S	Probability of survival
T_s	Sintering temperature [°C]
T_M	Melting temperature $[C]$ (UO_2= 2865 °C)
A	Material parameter determined by the microstructure
ADS	Aluminium-di-stearate
ADU	Ammonium diuranate
AUC	Ammonium uranyl carbonate
AZB	Azodicarbonamid
B	Constant of integration [MPa/m^2]
BNFL	British Nuclear Fuels Ltd

C	Compact centerline pressure [MPa]
c	Crack length [m]
D	Sample diameter [m]
d	Average imprint diagonal [m]
DC	Dry conversion
E	UO_2 Young's modulus (=224,923 GPa)
F	Applied load to the tested sample [N]
GECO	General Electric Company
Gp1	First group of pellets
Gp2	Second Group of pellets
Gp3	Third group of pellets
H	Vickers Hardness [MPa]
IDR	Integrated dry route
L	Compact length
L/D ratio	Length to diameter ratio
LVDT	Linear variable displacement transducer
LWR	Light water reactors
m	Total compact mass
N	Number of measurements
n	Stress exponent
OA	Oxidative atmosphere
OP	Oxidized uraniua powder
OS	Oxidized urania pellet scrap
P	Probability of failure

PCI	Pellet clad interaction
ppm	Particle per million
Q	Activation energy [kJ/mol]
R	Sample radius [m]
r	Radial distance from the compact axis [m]
RA	Reducing atmosphere
rpm	Rotation per minute
s	Shear modulus [GPa]
SCC	Stress corrosion cracking
SWU	Separative work units
t	Sample thickness [m]
TD	Theoretical density [%] (UO_2=10,96 g/cm^3)
V	Volume under stress [m^3]
v	Velocity of sound [m/sec] (1x10^3 m/sec)
x	Contact radius between two particles [m]
z	Axial distance from the bottom of the compact [m]

Chapter 1

Introduction

1.1 State of the Art

The nuclear fuel cycle comprises several production and processing steps from mining to the final radioactive waste storage, including the use of fuel in the reactor, main stage of the cycle as it is where energy is produced. Uranium is the most common fuel used in nuclear reactors.

The nuclear fuel cycle can be divided into four main stages:

1. Obtaining of the fuel material
2. Fabrication of fuel elements
3. Fuel management in the reactor
4. Fuel reprocessing

The name of cycle comes from the fact that not all the fuel used in the reactors is burnt in the reactor core, so that it still remains in discharged fuel some fissile nuclei that after reprocessing can undergo further fissions, that is, the depleted fuel can be recycled to the reactor for more power production. This situation arises because the fuel is discharged from the reactor before all fissile nuclei present are consumed. This happens because of fission products with high absorption cross section that prevents to maintain criticality in the reactor. Another reason for the early discharge is the physical damage suffered by the fuel in the reactor a cause of high pressure and temperature.

A general but simplified scheme of the nuclear fuel cycle is presented in figure 1.1.

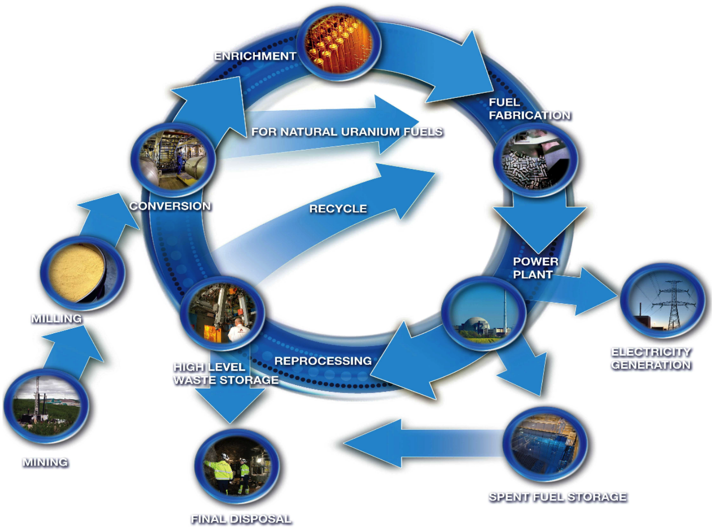

Figure 1.1: Simplified schematic of the nuclear fuel cycle [1].

The first stage of the nuclear fuel cycle includes mining, milling, obtaining of yellow cake, purification, and conversion processes to obtain the desired form for the fuel, metallic, oxide, or others. Natural uranium has an isotopic abundance by number of atoms of $0.0055\,\%\,U^{234}$, $0.720\,\%\,U^{235}$ and $99.275\,\%\,U^{238}$. Most of the reactors all over the world are LWR (Light Water Reactors), which require a fuel containing a higher concentration in U^{235}. Therefore, an enrichment process is normally necessary. Several enrichment processes have been developed since the beginning of nuclear reactors, but the only used at industrial level are gaseous diffusion and centrifuge separation. In this cases, uranium must be converted into UF_6, the material used for enrichment.

The second stage, fuel fabrication, is different for metallic and ceramic fuels. However, the most used nuclear fuels are ceramic. To fabricate this type of fuel the UO_2 powder is processed and transformed into ceramic fuel pellets, which will fill fuel rods. The fuel preparation involves the following steps:

- Addition of additives
- Pellet pressing
- Pellet sintering
- Pellet grinding

Finished pellets are introduced into fuel rods, which are bundled together forming the fuel elements, which are taken to the power plant and put in the reactor core for power production.

The third stage is the central one, as energy is released in the reactor by nuclear fission.

After withdrawing the fuel from the reactor, it starts the fourth stage of the cycle that includes separation of main components in the fuel: fission products and other radionuclides, uranium and plutonium. The first ones called radwastes are properly stored after conditioning, while uranium and plutonium can be recycled to the reactor after purification and conversion in the appropriate form.

The work developed in this Thesis is centered in the second stage, fabrication of nuclear fuel.

The nuclear power plants were constructed to have a design lifespan of approximately 40 years. However, with the technological development of the materials used in nuclear reactors, it has been possible for many countries to extend their reactor operational licenses for more than 20 years. The extension of the operational licenses comes together with new challenges to the operators of the power plants such as:

- Increase of the reactor power
- Upgrade of the reactor safety
- Reduction of the reactor downtime (reactor under maintenance)

The increase of the reactor power alone brings a series of complications to the mechanical resistance of the fuel element, which may fail during the plant start up if the power is too fast increased or even during the reactor operation.

These three challenges are seriously considered by the manufacturer of nuclear fuel. Improving the quality and resistance of the fuel element (nuclear fuel and cladding) is a must in order to have a more reliable power production.

In Light Water Reactors, the most spread and known type of nuclear fission reactors for production of electricity, nuclear elements are composed of thousands of cylindrical ceramic bodies, called pellets, in which the main raw material is uranium dioxide. Ceramics, by nature, have a poor thermal conductivity, a low tensile strength, a poor workability because they are brittle and low impact strength. On the other hand, they have a high corrosion resistance, a high hardness, a high melting point and are good insulators. So the challenge for the material developers is to find a point of equilibrium that allows the maximization of the "positive" characteristics of the ceramics relevant for their usage in a nuclear reactor and to mitigate those ones which could be prejudicial.

Development of nuclear materials is of great importance on the new reactor operational criteria where the fuel must withstand even more severe conditions in the reactor core. One part of this development consists in improving the mechanical resistance and reliability of the produced ceramic fuel pellet. Defect pellets may cause damages to the fuel cladding leading to a failure of the fuel element and in a worst situation may lead to an undesired shutdown of the power plant. Producing ceramic fuel pellets is a quite complex matter, involving many steps starting from the uranium dioxide powder production until its final dimensional adjustment at the grinding process.

1.2 Motivation

The motivating fact for the present work was the interesting investigation topic suggested by the Materials and Thermo-Mechanics department of AREVA after the completion of my Master Thesis by the University of Applied Sciences in Aachen, FH-Aachen. The proposed investigation topic, the influence of the microstructure and production parameters on the mechanical strength of UO_2 ceramic fuel, was a consolidation of the Master work research line.

The FH-Aachen does not have a PhD program; nevertheless, it belongs to the CHERNE network, which promotes an integration and cooperation among their members. Through this network a first contact to the Professor José Ródenas Diago from UPV (Universidad Politécnica de Valencia) was made. Professor Ródenas kindly accepted the invitation to visit the AREVA site in Erlangen, where we first met each other, and also where he could visit the Materials and Thermo-Mechanics department facilities, and certify himself that the proposed work was authentic and serious. In addition to that, details of the PhD work were discussed and a final agreement was achieved.

1.3 Justification

Nuclear power is an important source of electricity, already accounting for some 25–30 % of the world supply and growing. In France, over 75 % of the electricity supply is provided by nuclear power. In Europe as a whole, it is the dominant energy source. It is also becoming increasingly important in Japan and Korea. In the United Kingdom, over 20 % of the electricity is supplied from nuclear stations [10]. As for the United States, with their 103 commercial nuclear power plants producing electricity the nuclear energy represents more than 20 % [28] of their yearly national consumption.

The necessary raw materials to provide all this electricity for these and other countries can not be found everywhere. Thus, uranium, raw material for most nuclear power stations, can only be found in economically viable concentrations in a few big deposits in some countries, like Australia, Canada, Kazakhstan, South Africa, USA, Brazil, Russia and Namibia. Not all these countries dominate the entire nuclear fuel cycle and the most difficult and important part of it, the enrichment process, is still a quite well protected technology [29].

The fuel element for the nuclear power plant contains hard ceramics where the nuclear reactions take place in the reactor core. Different kinds of nuclear fuel are produced for different types of reactors. Higher burn up and longer time between refueling are the main objectives of the present fuel development. Among others there is also the economical factor, which plays an important role in the choice of the nuclear fuel.

One of the methods most used for the characterization and analysis of fuel quality is mechanical testing. In these tests, creep deformations, resistance to compression, fracture toughness and resistance against abrasion are analyzed. The obtained results can then be utilized for improving the fuel production quality minimizing defects, which could affect the in-pile fuel behavior.

Improving the final quality of the ceramic fuel is a must for the industry. A small damage to green pellets will result in damaged sintered pellets, which if not detected before leaving the manufacture plant, may lead to a not programmed reactor shut down since these defect pellets may increase thePCI (Pellet Clad Interaction) failure risk. According to Billaux [30], careful analysis of fuel rods showed that where the edge of the pellet had been chipped is just in front of the crack in the cladding. So, by developing the strength, the reliability and the quality of the ceramic fuel such situations can be reduced or even avoided.

1.4 Objectives

The objectives of the work can be synthesized in two points of relevance:

- **Improvement of the mechanical resistance of the ceramic fuel pellet**
- **Increase of the reliability and quality of a production lot**

In order to reach these objectives the following investigation and development steps are proposed:

1. **Choose of the additives to be mixed to the fuel matrix**

In most of commercial nuclear fission reactors the fuel has additives in its composition. These additives are mixed to the fuel in order to improve the fuel production performance by addition of oxidized scrap (also known as black U_3O_8), or for improving the compressibility of the fuel powder by adding small amounts of lubricants, or also to provide the formation of pores, which are relevant for the retention of gaseous fission products and finally for the control of reactor operation by adding a natural neutron absorber such as gadolinium.

2. **Determination of the pellet production process**

As a ceramic material the uranium oxide fuel should follow some production steps until being ready to be used in a nuclear reactor. In the industry many production processes are available and for this reason it is quite important to determine the most adequate one as well as to optimize it for our objectives.

3. **Determination of the sintering parameters and density of the fuel pellets**

At this point the ideal sintering particularities are going to be tested and developed. The sintering process is the most important step of the production process since it is here where the density, the pellet dimensions, etc. are determined by the variation of the sintering temperature, the sintering atmosphere and also by the sintering time.

4. **Determination of the pellet length and diameter**

The relation between length and diameter in cylindrical bodies is relevant for their strength. At this work, pellets with different dimensions are intended to be investigated, showing that with a combination of lengths and diameters the pellet mechanical strength can be improved.

5. **Determination of the testing procedures**

Several testing procedures for ceramics can be found in literature. At the present work the Vickers indentation technique and the creep test are going to be proposed for analyzing the plasticity of the fuel pellet. With the first one the plasticity of the sample will be analyzed at room temperature whereas with the creep analysis it will be analyzed at higher temperatures. The strength of sintered and not sintered pellets will be studied by the diametrical compression test (Brazilian Test), while the mechanical resistance of the not sintered pellets against mechanical shocks is going to be tested with the so-called squirrel-cage.

1.5 Structure of the Thesis

After the introductory chapter the second one brings an overview of the ceramic technology. The chapter was divided in two parts, in the first some important ceramic characteristics are presented while in the second one relevant fracture behavior aspects are mentioned and analyzed. In both parts relevant correlations and comparisons to UO_2 nuclear fuel are made.

The third chapter presents the nuclear fuel fabrication process. An especial emphasis is dedicated to the laboratory scale pellet production process. This part shows in detail the production process of the tested ceramic fuel pellets.

The fourth chapter presents each mechanical testing procedure used in the analysis of the mechanical resistance of the ceramic nuclear fuel pellets.

In the fifth chapter results are discussed. Furthermore, the microstructure analysis of the produced pellets is presented.

Finally, the sixth chapter summarizes the work presenting conclusions of the Thesis and future perspectives.

Chapter 2

Ceramics Technology

Ceramic materials are extensively used since thousand of years as pottery before metals were used. Their unique “positive” characteristics such as corrosion resistance, high hardness, high melting point and good insulation contrast to some “negative” ones e.g. poor thermal conductivity, low tensile strength, poor workability because they are brittle, exhibiting practically no plasticity and low impact strength. Those make the ceramic usage a real challenge for the industry but, nevertheless a world without them can not be imagined.

The ceramic spectrum has grown and developed a lot in the last century, starting from the simplest pottery objects made of clay, passing through the old oxide and non-oxide ceramics such as Al_2O_3 and finally reaching the actual advanced ceramics such as the semiconductors, ceramic matrix composites, refractories, fiber-glass, SiC, TiN, etc.

Ceramics are inorganic, nonmetallic solids, which develop their final properties during firing and sometimes during firing and pressing. In other words, what is neither a metal, a semiconductor or a polymer is a ceramic [4].

It would be impossible to describe in the present work all properties and characteristics of the existing ceramic types. For this purpose there are several ceramic books [4, 8, 31, 32, 33, 34, 5], which cover with property the ceramic subject as a whole.

This section was divided into two parts ceramics and fracture mechanics of ceramics. In the first one some important ceramic characteristics are presented while in the second part relevant fracture behavior aspects are mentioned and analyzed. In both parts relevant correlations and comparisons to UO_2 nuclear fuel are made.

Other relevant parameters and characteristics such as hardness and Weibull statistics are discussed in chapter 4.

2.1 Ceramics

2.1.1 Thermal Conductivity

Thermal conductivity can be defined as the capability of an object to conduct some amount of heat. This heat in a solid can be conducted by various carriers e.g. electrons, lattice waves (or phonons), magnetic excitations, and, in some cases, electromagnetic radiation [35]. In metals the conduction by free electrons is predominant while in ceramics the process is preferably done by lattice oscillations. Moreover, the thermal conductivity is temperature dependent and in metals it increases by increasing the temperature while in most ceramics it decreases by increasing the temperature [26].

Coming to the UO_2 ceramic fuel it can be seen that some very specific characteristics undergo changes during the reactor operation e.g. the production of radioactive fission products, which can form separate phases or may be dissolved in the fuel matrix [2]. Furthermore, not only fission products can affect the thermal conductivity of a ceramic nuclear fuel but also the density (porosity), the stoichiometry (O/U ratio), additives, irradiation duration, etc [36].

There are three UO_2 thermal conductivity mechanisms, the phonon conduction by means of lattice conduction, phonon conduction by means of radiation and electronic conduction [36]. According to Peierls [37] for temperatures until 1300 °C both phonon conduction processes predominate. On the other hand with even higher temperatures UO_2 will turn to a semiconductor having the phonon radiation conduction and the electronic conduction as responsible processes for the increase of the conductivity.

Figures 2.1b and 2.1a present respectively the thermal conductivity of UO_2 and of uranium-plutonium mixed oxide ($(U, Pu)O_2$) operating in a pressurized water reactor (PWR) and a fast reactor (FR).

2.1.2 Thermal Expansion Coefficient

When energy in form of heat is applied to a solid body there is a tendency of this solid to have a change in its volume. This change in dimensions by the action of heat is characterized as thermal expansion. Hence, most materials expand when heated being those which contract quite rare.

The thermal expansion coefficient is the factor representing the change in dimensions of a material by temperature variation and is usually expressed in volumetric or linear units (see equation 2.1 and 2.2).

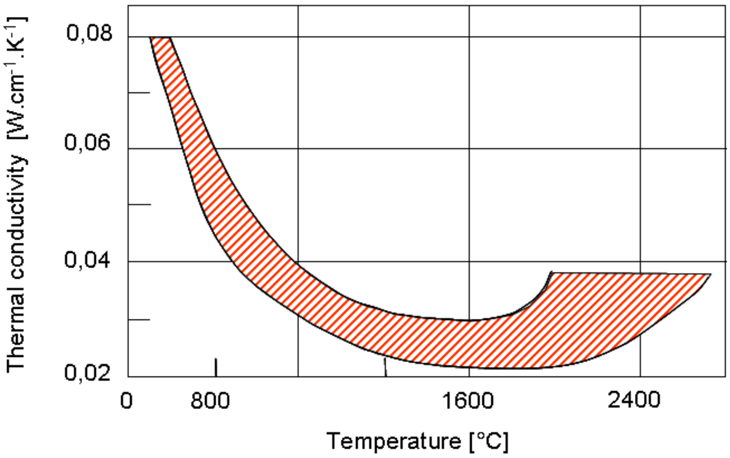

(a) UO_2 thermal conductivity dependence to the temperature [36].

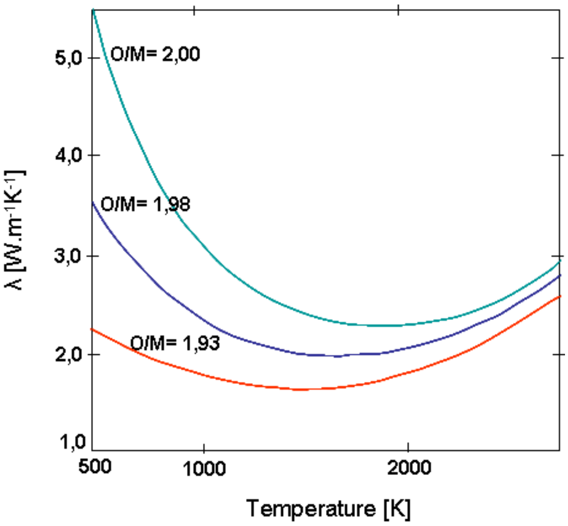

(b) Thermal conductivity of $(U, Pu)O_2$ mixed oxide and O/U ratio effect [2].

Figure 2.1: Thermal conductivity profiles.

$$\alpha_L = \frac{1}{L}\frac{dL}{dT} \tag{2.1}$$

$$\alpha_V = \frac{1}{V}\frac{dV}{dT} \tag{2.2}$$

The irradiation effect on both fuel and cladding material thermal expansion coefficients can be considered negligible [36]. During the reactor operation the thermal expansion of the ceramic fuel and of the fuel cladding is different since their expansion coefficient are distinct. Because of the much higher fuel temperature than the cladding temperature, the thermal expansion is also higher at the fuel leading to a reduction in the fuel-cladding gap affecting in return the temperature of the fuel [2] (see table 2.1). After 2 cycles of irradiation and high rod power the gap is closed in the hot state.

In figure 2.2 it is presented the temperature profiles for two reactor types a fast reactor (FR) and a pressurized water reactor (PWR). In the case of a fast reactor the central temperature (Tc) may easily exceed $2000\,°C$, while in a PWR under normal operation conditions it will rarely reach values above $1200\,°C$ [2].

2.1.3 Specific Heat

The specific heat capacity is the energy required to increase the temperature of an object or body an amount dT. This process can be under constant pressure or volume. The specific heat capacity at a constant pressure is known as C_p (eq. 2.3) and at constant volume C_V (eq. 2.4) being generally $C_p > C_V$. However, in solids, the difference between them can be negligible [26].

$$C_p = \left(\frac{dq}{dT}\right)_p \tag{2.3}$$

$$C_V = \left(\frac{dq}{dT}\right)_V \tag{2.4}$$

Table 2.1: Typical mean cladding temperatures, Tmc, mean fuel temperatures, Tmf, expansion coefficients and gap sizes in the maximum flux plane of PWR fuel elements. Data extracted from Bailly [2].

	PWR
Cladding	Zircaloy
T_{mc}	$340°C$
α(from $25°C$ to T_{mc})	$6.7e^{-6}$
αT_{mc}	$2.1e^{-3}$
Ceramic Fuel	UO_2
T_{mf}	$850°C$
α(from $25°C$ to T_{mf})	$9.7e^{-6}$
αT_{mf}	$8.3e^{-3}$
Initial gap size	$170\mu m$
Gap size under hot conditions	$120\mu m$

The specific heat is not much influenced by the grain size or shape but the porosity has a strong effect on it. A porous ceramic material will need less energy for heating than a dense one [26].

In a UO_2 ceramic nuclear fuel the specific heat capacity is a function of fuel composition, operation temperature, burnup cycle and O/U ratio. The burnup cycle and O/U ratio effect on the heat capacity are very small and can be neglected [3].

From different literature many tables and graphics can be obtained with the specific heat capacity of UO_2. Data from Fink [38], Ronchi [39, 40] and Lucuta [41], published in Popov et al. [3], are compared in the results from the software MATPRO (see figure 2.3). It shows that the specific heat capacity reaches a maximum by $3000\,°C$ and then decreases due to brake down of the crystallite structure and melting of the ceramic.

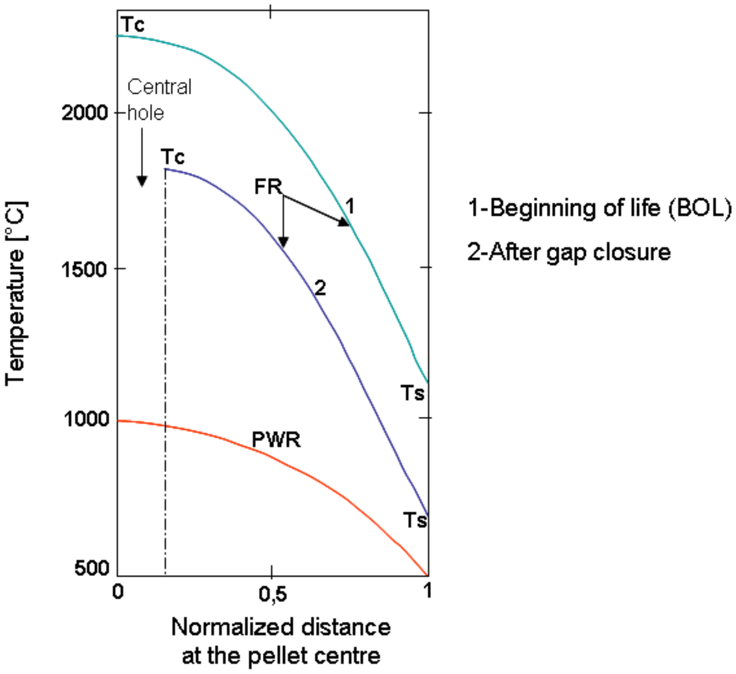

Figure 2.2: PWR and FR pellets temperature profiles [2].

2.1.4 Melting Point

The melting down of the reactor core must be avoided in any incident or accident in a nuclear power plant. The knowledge of the nuclear fuel melting point is of great relevance for a safe reactor operation since it clearly shows fuel working limits. Elevating the fuel temperature beyond its melting temperature will certainly result in the melting down of the reactor core.

The melting point of any material basically depends on the bond strength present among their atoms. The determination of the bonding in ceramic materials is not easy. It is known that a pure ionic compound does not exist since even in compounds thought to be 100 % ionic, e.g. $NaCl$ or LiF, a covalent component is present [8]. Moreover, pure covalent compounds are just possible to be formed between identical atoms, e.g. $C - C$, otherwise the elements are said to have a strong covalent character, e.g. $Si - O$ and finally, the bonding can also have a metallic or a van der Waals component [8].

Fusion or melting, evaporation and sublimation happens just when enough energy is applied

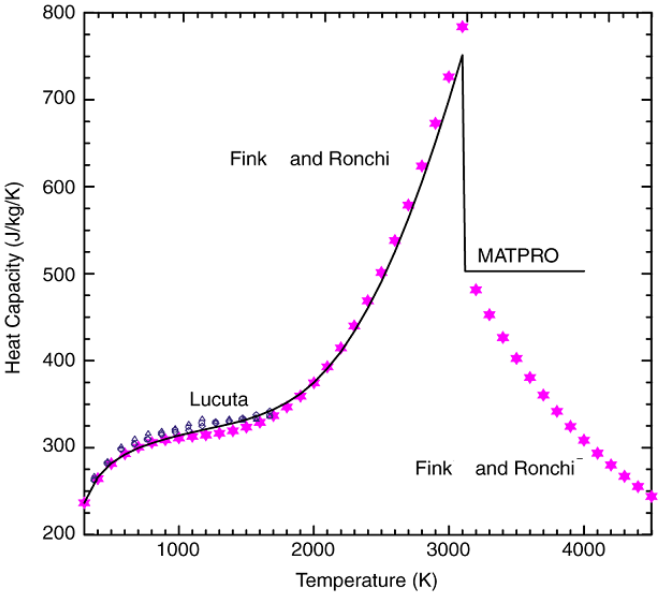

Figure 2.3: UO_2 specific heat capacity factor [3].

to the substance allowing it to overcome the potential energy holding the atoms together [4]. However, the application of pressure will influence the melting point. For this reason it is quite important that by the determination of melting points the same pressure should be applied.

Table 2.2: Bond Energy [8].

Bond type	Bond energy $[kJ/mol]$
Ionic	50 - 1000
Covalent	200 - 1000
Metallic	50 - 1000
van der Waals	0.1 - 10
Hydrogen	10 - 40

The bond type alone does not determine whether more energy will be necessary for melting. What really matters is if the covalent or ionic bonds are strong or weak in the analyzed substance, as it can be seen in table 2.2. So, by increasing the bond strength the melting point is also increased as presented in figure 2.4 extracted from Barsoum [4]. It can be seen that three substances have the same structure MY_2 but different structure arrangements (being the TiO_2 three-dimensional, the CdI_2 a layered structure and a molecular lattice for CO_2), which consequently produce distinct covalent character having TiO_2 the lowest and CO_2 the highest, which finally results in huge melting point variations.

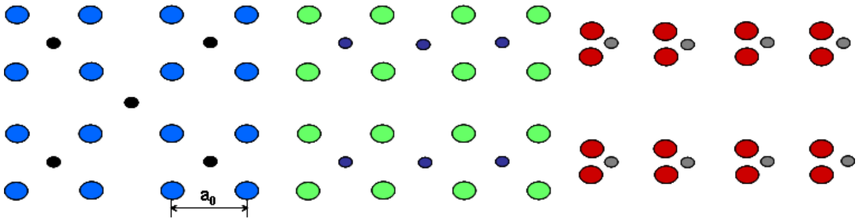

TiO_2 Melting Point = 1857 °C

CdI_2 Melting Point = 387 °C

CO_2 Melting Point = -57 °C

Figure 2.4: Polarization effect on crystal structure and melting point [4].

2.2 Fracture Mechanics of Ceramics

2.2.1 Elasticity

When a material is deformed in its geometry by the application of stress it returns to its original dimensions after the stress is removed. In such situation this material has elastically behaved.

Ceramic materials have very tight elastic strain limits. Furthermore, they have a high brittle character with no or little plastic deformation, which in many situations limits their usage.

Fracture mechanics of isotropic ceramics involves the knowledge of their elastic characteristics, which can be determined for instance by the Poisson's ratio, the Young's modulus, the rigidity modulus and the bulk modulus. Among these the most known and used moduli are the Young's modulus, the rigidity modulus and the Poisson's ratio. Hence, with the knowledge of at least two elastic moduli all the others can be calculated allowing the material characterization.

The Young's modulus represents the linear deformation of the material, i.e., the proportional limit where the applied tensile stress is directly proportional to the strain. This linear relationship is also known as Hook's elasticity law and can be calculated by the formula 2.5:

$$\sigma = E\epsilon \tag{2.5}$$

where σ is the applied tensile stress, ϵ is the strain and E is the Young's modulus.

The rigidity modulus represents the relation between shear stress and shear strain by the application of a shear stress and can be defined the formula 2.6:

$$G = \frac{\tau}{\gamma} \tag{2.6}$$

where G is the rigidity or shear modulus, τ is the applied shear stress and γ is the resulting shear strain. Finally, the Poisson's ratio is a measure of the Poisson's effect while a material is compressed or stretched. When stretched, an isotropic material usually decreases its thickness while its length is increased and when compressed the sample thickness tends to increase and the length to decrease. The ratio between the transverse strain to the axial strain is the Poisson's ratio:

$$\mu = \frac{\Delta z/z}{\Delta x/x} \tag{2.7}$$

where μ is the Poisson's ratio, $\Delta z/z$ is the transverse strain and $\Delta x/x$ is the axial strain.

Some of the factors having an influence on the elasticity of a body are the temperature, the crystal structure and the presence of porosity. According to Wachtman [5] the temperature reduction of a material towards absolute zero (see figure 2.5) will result in a maximum value of the elastic constant fulfilling the third law of thermodynamics, which states that the entropy of a system approaches a constant value as the temperature approaches zero. Furthermore, the temperature increase in most cases leads to an elastic extension of the solid and consequently an increase in the atomic separation. So depending on the crystal arrangement there will be a variation of the thermal expansion coefficient, which directly affects the elasticity [31]. As for the porosity, it is an inherent part of a ceramic body. Its presence can be justified by many reasons and the increasing amount of porosity in a solid will decrease some of its mechanical properties [5] such as the strength and the thermal conductivity.

2.2.2 Plasticity

A solid undergoes plastic deformations by the application of a load causing irreversible shape changes and do not allow its recovery to its initial dimensions. Hence, plastic deformations of crystals are quite complex mechanisms where the knowledge is still being developed especially for ceramics.

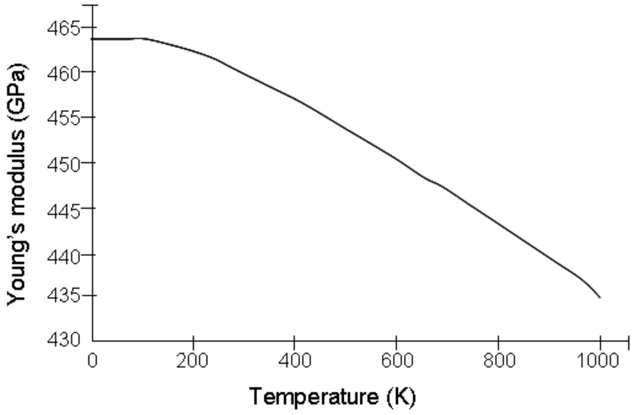

Figure 2.5: Temperature dependence of Young's modulus for Al_2O_3 single crystal [5].

Plasticity in ceramic materials is greatly influenced by the sintering process. The heating and cooling rate, the sintering temperature, the sintering atmosphere and time determine the diffusion mechanisms in the ceramics modifying grain boundaries and sizes as well as the porosity.

The sintered ceramic product will certainly behave differently when a load is applied to it at room temperature where, usually, ceramics have no or little plasticity and also when the same load is applied to it at high temperatures for instance causing creep. In fact, plastic deformations during creep situations are of a great importance for ceramics, which are used at high temperatures in engines, gas-turbines and as nuclear fuel. The creep behavior will be explained in the next section.

The plasticity of a ceramic material at room temperature can be determined by increasing the load at a constant rate until the fracture occurs. Some methods for obtaining the plasticity are the three or four point bending test, and the diametral compression test (Brazilian Test). In figure 2.6 stress-strain curves for MgO and KBr are presented and in figure 2.7 for UO_2. Curves for the first two materials were obtained from Wachtman [5] by bending tests performed by Gorum [42] and for sintered UO_2 was obtained by performing the Brazilian test at one of our tested samples. In this last case the load was raised at a constant rate of $0.2\,mm/min$ and reached a maximum deformation of $0.6\,mm$ and a maximum load of $4019\,N$ before plastic failure.

Plastic deformations in crystalline solids can be originated by many mechanisms such as crystal dislocation or slip, vacancy motion, twinning and phase transformation [8]. Nevertheless, for both single crystal and polycrystalline materials the most important plastic deformation mechanism is the slip.

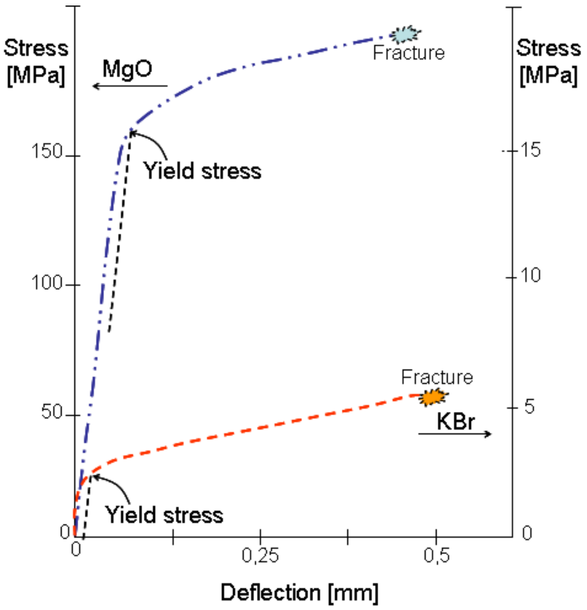

Figure 2.6: Stress-strain curves for MgO and KBr.

2.2.3 Creep

In the case of ceramic nuclear fuel the creep characteristics are quite important for the determination of the possible fuel performance potential, since during the reactor operation there will be stress increase within the fuel as a consequence of interaction with the fuel cladding, differential thermal expansion and also from volume change induced by fission products [43]. The increasing fuel cladding interaction may lead to significant plastic deformation and fracture of the cladding material, limiting then the designed lifetime of the fuel element. Finally, the presence of porosity within the fuel with the objective to accommodate, and possibly minimize, the volume increase of the pellet and its consequent strain towards the clad may not be well succeeded if the ceramic fuel ability to creep into this available porosity does not achieve the designed results [43].

The creep behavior can be measured in tension, compression, torsion and by banding and their different data can not be compared since the sample deformation type is different in each test configuration [44]. Also according to Richerson [44] the creep behavior of ceramics is influenced among others by microstructure (grain size, porosity), temperature, stress and stoichiometry. The yield strength of the material is not overcome by the applied testing stresses.

Creep of polycrystalline ceramics is a complex matter and is generally attributed to three creep mechanisms - diffusional creep, dislocational creep and grain boundary sliding - where the

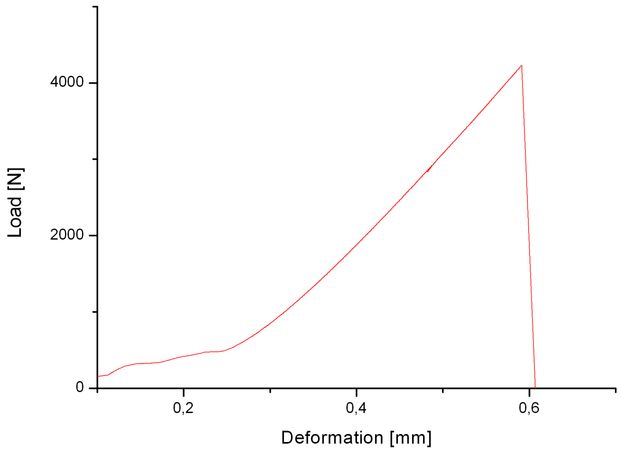

Figure 2.7: Stress-strain curve for UO_2.

dominant mechanism is directly influenced by the temperature, stress, density, grain size and impurity content [44]. When the uranium oxide fuel is considered it is found in Burton [45] that the lattice diffusional creep (Nabarro-Herring type) mechanism dominates the creep behavior at moderate temperatures and low stresses while the dislocational creep does at elevated temperatures and high stresses.

The creep behavior of ceramic materials can be depicted by the Arrheniuns equation (eq. 2.8), where $\dot{\varepsilon}$ is the creep rate, A is a constant related to the material, n is a constant dependent on the creep mechanism, Q is the activation energy, $\bar{R}$ the gas constant and T the temperature. The constant n is usually referred as the stress exponent, and together with Q provide information about the mechanism of creep in the ceramic [44]. For $n = 1$ the predominant mechanism is the lattice diffusional creep (Nabarro-Henring type), whereas when $1 < n < 2$ the predominant mechanism is the grain boundary diffusion (Coble creep type), and finally when $3 < n < 6$ the dislocational creep mechanism dominates [26].

$$\dot{\varepsilon} = A\sigma^n e^{\frac{-Q}{\bar{R}T}} \tag{2.8}$$

The determination of the creep behavior of ceramics is obtained by applying a defined load for a long period, e.g. $24h$, $48h$, etc., at a high temperature leading to a continuing deformation with time (see figure 2.8). The typical creep curve can be divided in three parts:

- Transient or primary creep: after the elastic extension where the material still elastically behaves, the primary creep stage starts. At this level a fast decrease in the creep rate is observed. This is because of the hardening of the material becoming quite saturated with new dislocations in a short time. This stage can be described by the following simple power law relation where ε_p is the primary creep strain, A and m ($m < 1$) constants and t is the time [26].

$$\varepsilon_p = At^m \tag{2.9}$$

- Secondary or steady creep: at this stage the strain increases linearly with the time at a constant creep rate for a short or long period of time. This is due to the balance between work hardening and stress annealing. This stage is the most understood and usually the creep strain rate from the tested material is referred from it. Due to the linear shape of the creep curves in the secondary creep range, a simple time relation can be derived [26],

$$\varepsilon_s = At \tag{2.10}$$

- Tertiary creep: it is where the creep rate increases rapidly prior to the failure [8, 5]. Moreover, as the temperature or stress increases, the creep rate also increases and the duration of the steady state creep decreases [44].

The creep strain is the contribution of each creep stage. For the primary and secondary creep the contributions are ε_p and ε_s. Since the onset of the tertiary creep is followed by early failure of the component it can be neglected, being the creep strain depicted as,

$$\varepsilon_c = \varepsilon_p + \varepsilon_s \tag{2.11}$$

2.2.4 Influence of the Porosity on the Mechanical Strength

The term porosity is not related to voids or free spaces among atoms but to the void fraction among macro-particles reducing the bulk theoretical density of a material. In ceramics the porosity is basically classified in open porosity, which is the type of not closed pores present on the surface of a solid body and in closed porosity, which are the intragranular or intergranular closed pores without connection to the surface.

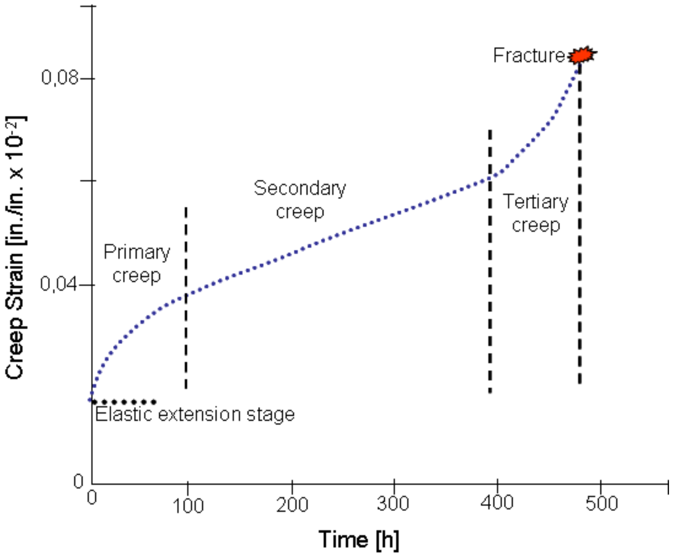

Figure 2.8: Typical creep curve [5].

The presence of pores in most ceramics is difficult to be avoided and sometimes controlled. Furthermore, porosity influences negatively the strength of the ceramics since it reduces the cross-sectional area of the material and also because it acts as a point of stress concentration, which is the point where a flaw starts its propagation until the critical stress is reached causing the failure of the material. Nevertheless, ceramics such as uranium oxides are designed to have up to 6 % in porosity because this porosity despite its negative influence is quite important for the nuclear fuel during the in-reactor operation.

Pores are to some extent also desired by ceramics, which go through high-stress gradients [31]. Under stresses, for instance, induced by thermal shock the porosity can act as crack-propagation-stopper allowing that instead of a complete failure from the ceramic body surface cracking would be obtained. This is because of the fast drop of the stress from a very high value at the surface to a low value in the interior [31]. In the case of a ceramic nuclear fuel the porosity is one of many design parameters determining the mass of the nuclear fuel in the reactor core. Hence, its determination depends on the reactor core design and construction.

According to Rice [46] pores are nowadays considered, if not always quite often, as an integral part of the failure causing flaws under tensile stress, which is a change of mind from the scientific community since previously the porosity was just considered as a stress concentrator accentuating failure from other fracture sources. In fact, understanding the entire failure mechanism of porous materials is a complex matter since many variables give their contribution to the existing failure criteria such as for example the continuum mechanics criteria mentioned by Brückner-Foit et al [47], which similarly to all other existing criteria, can just be applicable to a very specific situation.

The porosity configuration, i.e. pores shape, distribution and concentration, has a great influence on the mechanical strength of a ceramic body. Their shape is usually characterized as spherical, cylindrical or ellipsoidal and they can be distributed inside the grains, intragranular pores or at the grain boundaries, intergranular pores as can be seen in figure 2.9.

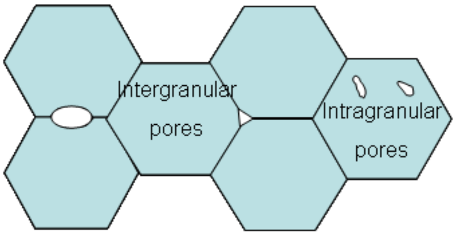

Figure 2.9: Intergranular and Intragranular pores.

In Munz [26] the porosity shape is described as a defect model. In each defect model multi axial failure criterion is applied to a large number of aleatory distributed defects. Failure will occur at that defect, which has the most favorable orientation to the stress field as can be observed in figure 2.10. In this figure an elliptical flaw type can be seen as well as an undisturbed load-path. At the uniform load-path the lines are straight and equally spaced, indicating that the load is evenly distributed. Because of the presence of the pore the line distribution is disturbed forcing the lines to go around it within a shorter distance and depending on the orientation of this pore the stress lines are going to be closer or not to one another at the tip, a clear indicator of stress concentration since more load is flowing through a smaller area. In Wachtmann [5] the maximum normal stress in y direction at the tip can be calculated by the equation 2.12

$$\sigma_{yy} = \sigma \left[1 + 2 \left(\frac{c}{\rho} \right)^{1/2} \right] \tag{2.12}$$

where σ is the applied normal stress to the body, ρ is the radius of curvature of the ellipse which can be calculated by equation 2.13 , where b and c are the length and the height of the pore. It is now clear that for pores or cracks with $c \gg \rho$ the stress concentration will be higher and consequently the measured strength of the body will be smaller than the theoretical one.

$$\rho = \frac{b^2}{c} \tag{2.13}$$

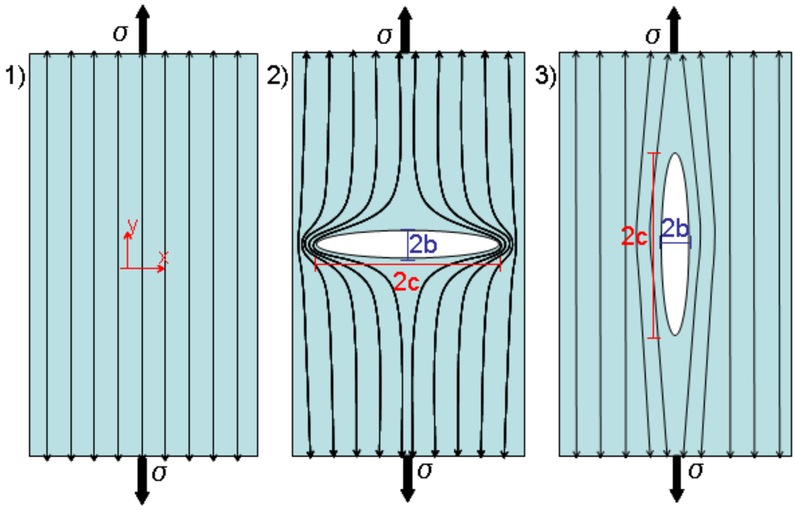

Figure 2.10: Load-path. In 1 a undisturbed and uniform load-path; in 2 a pore greatly disturb the load-path, so higher stress concentration when compared to 3 where the pore has a smaller radius of curvature perpendicular to the load-path [6].

2.2.5 Influence of the Grains on the Mechanical Strength

Despite the great influence of the porosity on the mechanical strength of ceramics as explained in the past section, the grain size also gives some contribution to the strength, toughness and hardness of ceramic materials. Actually not only the grain size is important but also their orientation, shape, distribution and the combination of all of these factors.

The grain size is basically determined by the presence of additives mixed to the ceramic powder and by the sintering procedure. By elevation of sintering temperature there is a natural grain growth and a porosity reduction as well as a change in the porosity location, i.e. in the highly porous body at the beginning of the sintering there is some porosity migration from its intergranular position to the intragranular position in a final sintered sample. Therefore the sintering isothermal duration, the sintering temperature and the sintering atmosphere are the most influencing factors on the microstructure evolution.

In the literature it is extensively described that ceramics with smaller grains have higher tensile strength than those with larger grains. However, practically, this behavior is not observed in all published studies. Furthermore, in Rice [7] the analysis was divided into two groups, larger grain samples showing clearly that with the increase of the grain size the tensile strength reduces, and samples with finer grains presenting a much smother tensile strength reduction with increasing grain size as can be seen in figure 2.11. Carniglia [48, 49] covered in his work a great grain size range and also observed the presence of both behaviors described by Rice [7] suggesting that failure mechanism for the finer grain branch was by microplasticity governed by the Hall-Petch strengthening (equation 2.14 where σ_e is the yield stress, σ_0 is the resistance of the lattice against dislocation, K_y is the strengthening coefficient and G is the average grain size), while the larger grain branch were governed by the Griffith flaw failure mechanism with the flaw dimension being approximately those of the grain size. He attributed this change in the failure mechanism to the fact that the stresses for failure from flaws being higher than the stresses to activate microplastic failure at finer grain branch, until grain size reached a certain size large enough to allow flaw failure at stresses below those needed for microplasticity. His theory, however, was proven not to be applicable in a wider range of materials, microstructure and testing procedures. In fact for both finer and larger grains branches failure comes from the change in the flaw-to-grain-size ratio where the strength can be determined by the flaw size [7].

$$\sigma_e = \sigma_0 + \frac{K_y}{G^{1/2}} \tag{2.14}$$

The toughness and hardness are also influenced by the grain morphology. The grain dependence of hardness in indentation tests primarily arises from its impact on plastic deformation, which is the key mechanism of forming permanent indent deformations [7]. The hardness to grain size relation behaves, at least theoretically, in a similar way as in the case of the tensile strength. In fact in McColm [50] it is stated that with smaller grains there will be an increment in the hardness in the indentation test because dislocations generated by the indenter are blocked by grain boundaries. In agreement to McColm [50] statement, Bennison and Lawn [51] have shown that in some pure alumina ceramic samples those with smaller grain size have higher indentation-strength. On the other hand, in Vekinis et al [52], also working with alumina, were presented results where the toughness represented by the crack resistance energy, G_{Ic}, increases with the increasing grain size. Finally, according to results from Rice [7] and from Monroe and Smith [53] presented by Wachtman [5] depending on the crystal symmetry the strength may not vary with the grain size. Rice [7] published that for cubic polycrystals, the fracture toughness is almost independent of the grain size. Both, Rice and Monroe observed that there is some tendency of a maximum toughness in some mid-grain-size cubic polycrystals whereas noncubic polycrys-

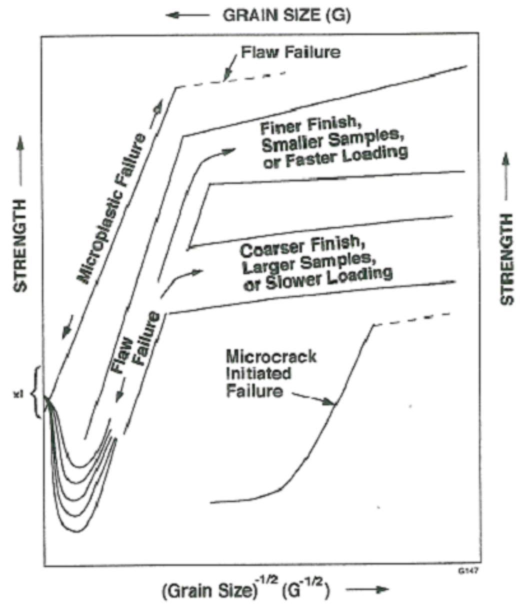

Figure 2.11: Grain size versus strength [7].

tals presented a clear toughness maximum. Moreover they have identified that at the particular grain size where the maximum occured it was primarily caused by the thermal expansion of the material.

In the case of the ceramic nuclear fuel there are also different tendencies and analysis of the influence of the grain size on the UO_2 fuel mechanical resistance and as consequence a final agreement among the scientific community to this subject is still far to be achieved.

The different tendencies and analysis in the nuclear ceramic field regarding the grain size influence on the fuel mechanical resistance are going to be exposed in in the chapter 5 where results are analyzed.

2.2.6 Fiber Reinforcement

The idea of reinforcing composite materials with fibers has been in evidence since the ancient Egyptian times or even before that period. By that time this kind of material was used for the production of bricks, which afterwards were used in civil engineering for the construction of walls, houses, monuments etc.

In the last century the development of composite materials evoluted quite fast basically because of the industrial need for new materials, which would withstand their highly severe usage conditions. The most cited material developer is the aerospace and aviation industry, but other branches also stepped forward in technological development for instance the automotive industry, the military industry, the energy industry and the construction industry. Polymeric and organic fibers can not be used in ceramic matrix composites (CMC) since their melting or degradation temperatures are below $500\,°C$, so the best type of materials to be used are the polycrystaline or amorphous inorganic fibers or carbon fibers [54].

The aerospace industry was greatly challenged to explore the unknown space outside the invisible atmosphere barrier and because of this completely new environment awaiting to be explored new materials needed to be developed and experienced in order to the future extraterrestrial explorations come true. One of the most critical situation where the developed ceramic matrix composites (CMC) were used, was at the heat shield panels of the space module since the reentry temperature can easily reach about $2000\,°C$. For this extrem situation the best material to resist is a ceramic matrix composite, which combine excellent thermal and mechanical shocks resistance with a low weight [55].

Another important material developer industry are the automotive and the military industry. The automotive industry started using CMC with the objective to reduce the total weight of the cars whereas the military were involved to develop bullet-resistant materials.

The nuclear industry also is researching and developing CMC for the future reactors such as the very high temperature reactor ($VHTR$) and the gas cooled fast reactor (GFR). Core structural materials working in these types of nuclear reactors need to resist very high temperatures and radiation damages and also need to have a low neutron absorption cross-section [54]. Moreover, for this kind of application monolithic ceramics do not offer a reasonable safety margin since they have an intrinsic brittle character. Therefore, the potential key candidates to be used in this rigorous environment as structural materials are the CMC for instance SiC, ZrC, TiC, VC, ZrN, TiN and AlN [54].

2.2.7 Brittleness

Most probably the first aspect remembered when talking about ceramics and glasses is their brittle character. Furthermore, at low temperatures not only glasses or ceramics can behave in a brittle way but also polymers and metals.

The brittle behavior of ceramics is the reason why these fragile materials should be dealed with great care while shaping or machining them after sintering. The machining process is directly dependent on the material strength, which in the case of ceramics can vary a lot even in a same production lot even though they were similarly handled and manufactured.

The brittle fracture occurs because of the low energy rate absorption of a material not enabling a deformation. In other words, a material is brittle if under a stress situation it breaks without or with little plastic deformation and unfortunately this situation often happens without any warning coming out from the material. For this reason, understanding the reliability of a brittle material is of great importance for avoiding unexpected failure, which can put lives in risk in the case of a sudden fracture.

The theoretically calculated and the experimentally measured strength of ceramics are completely different. The theoretical strength (σ_{th}) could just be reached if the analyzed ceramic had no dislocation or ceramographic defects i.e. a perfect ceramic with no flaws and no sharp corners introduced during processing. Such ceramic material unfortunately does not exist but even though it is possible to calculate, which would be the highest achievable strength. According to Carter [8] this theoretical strength for ceramics can be up to 500 times higher than the measured one just because the real ceramic samples may have dislocations and flaws directly influencing their mechanical strength.

Orowan [56, 57] developed a theory where the atoms dislocation could explain plastic deformations. The dislocation theory can explain diverse plastic deformation processes like creep, fatigue, fracture and strengthening mechanisms [58]. One simple way to calculate the theoretical strength is by using the Orowan approach as demonstrated below [8].

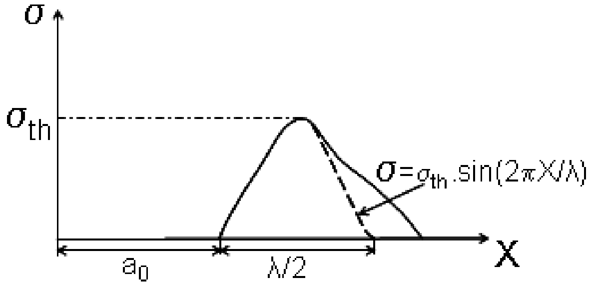

Figure 2.12: Strength versus distance curve [8]. The dotted line represents the sinusoidal approximation of the real $\sigma - X$ curve.

In figure 2.12 we have a plot of the measured strength, σ, versus the distance X between planes of atoms. λ and a_0 (see figure 2.4 for a_0) are the wavelength of the sine wave and lattice spacing respectively. By a sinusoidal approximation of the $\sigma - X$ curve close to the lattice spacing we can write:

$$\sigma = \sigma_{th} sin(\frac{2\pi x}{\lambda}) \tag{2.15}$$

where x represents the displacement of the planes beyond the equilibrium value, a_0.

The total energy for the formation of the two new surfaces is 2γ, which is the area under the curve or the integral of equation 2.15 between 0 and $\lambda/2$:

$$2\gamma = \int\limits_{0}^{\lambda/2} \sigma_{th} sin(\frac{2\pi x}{\lambda}) dx \tag{2.16}$$

$$2\gamma = -\frac{\sigma_{th}\lambda}{2\pi} \left[cos\pi - cos0 \right] \tag{2.17}$$

$$\frac{\sigma_{th}}{\gamma} = \frac{2\pi}{\lambda} \tag{2.18}$$

For low stresses the material will be elastic obeying Hook's law and Young's modulus can be written as

$$E = \frac{\sigma a_0}{x} \tag{2.19}$$

$$\frac{d\sigma}{dx} = \frac{E}{a_0} \tag{2.20}$$

In case of small displacements $sinx \sim x$ and equation 2.15 can be written as

$$\frac{d\sigma}{dx} = \frac{\sigma_{th} 2\pi}{\lambda} \tag{2.21}$$

Now combining the equations 2.20 and 2.21 we have

$$\sigma_{th}\frac{2\pi}{\lambda}=\frac{E}{a_0} \tag{2.22}$$

Finally by substitution of equation 2.18 the Orowan equation is obtained

$$\sigma_{th}=\sqrt[2]{\frac{E\gamma}{a_0}} \tag{2.23}$$

With the resulting Orowan formula one can calculate for instance the theoretical strength for UO_2. The surface energy value was calculated according to Hall's equation [59], 2.24,where T is sample temperature. By increasing the temperature there is a decrease in the surface energy. With T at $20\,°C$ the surface energy corresponds to $0.8472\,J/m^2$.

$$\gamma = 0.85 - 1.4e^{-4}T\ \left[J/m^2\right] \tag{2.24}$$

The Young's modulus also varies with the temperature and can be calculated according to the following equation [60]:

$$E = 22.43e^4 - 31.19T\ \left[N/mm^2\right] \tag{2.25}$$

where T is the temperature in Celsius. For T at $20\,°C$ we have $E = 224.923GPa$.

Theoretical lattice spacing values can easily be calculated with the equation 2.26 where PU is the atomic weight of uranium, MO is the molecular weight of oxygen, N_a the Avogadro number and TD is the UO_2 theoretical density. The calculated value, at room temperature ($20\,°C$), is 0.5469769 nm, which is in good agreement to the measured value by X-ray diffractometry of 0.54707 nm in Leyva [61].

$$a_0=\sqrt[3]{\frac{4*(PU+2MO)}{N_aTD}} \tag{2.26}$$

With all necessary data the calculated theoretical strength for UO_2 is $18.66\,GPa$ while the measured one according to Santana [62] can reach up to 40 MPa a value about 450 times lower than the theoretical one. This result is not surprising at all since the intrinsic presence of porosity and flaws in the ceramic matrix is the main reason for the strength reduction.

The influence of flaws on the theoretical mechanical strength can be explained by Griffith energy balance theory [63] in which he suggests that by the application of a stress to a ceramic body with internal flaws the reduction in the elastic strain energy and an increase of the energy necessary for creating a new crack (c) surface area will conduct to a fracture of the material. Griffith proposed his theory by observing that the theoretical strength values to fracture bulk glass was 100 times higher than the measured ones [64]. Furthermore, he also observed that the smaller the diameter of these fiber glass got the higher was the energy necessary to fracture them. His energy balance can be expressed as following [8]:

$$\frac{dW_c}{dc} = \frac{dW_s}{dc} \tag{2.27}$$

where W_c is the elastic strain energy and W_s is the energy for the creation of new surfaces. The elastic strain energy and the energy for the creation of new surfaces can be calculated by equations 2.28 and 2.29 respectively.

$$W_c = \frac{\pi c^2 \sigma^2}{E} \tag{2.28}$$

$$W_s = 4c\gamma \tag{2.29}$$

By performing the energy balance in equation 2.27 the Griffith equation is found to be

$$\sigma_G = \sqrt[2]{\frac{2E\gamma}{\pi c}} \tag{2.30}$$

2.2.8 Stress Intensity Factor

In a material containing a flaw the resistance against the fracture propagation is characterized by the stress intensity factor, K, which is the factor used to predict the theoretical stress intensity at the crack tip by the application of a load [26]. So, K depends on the geometry of the body containing the flaw, the flaw size and the applied load.

The stress intensity factor is usually associated to the existent linear independent modes of rupture (see figure 2.13):

- Mode I: opening tensile stress normal to the crack plane
- Mode II: in-plane shear stress leading to crack surface sliding over one another
- Mode III: off-plane shear stress leading to crack surface tearing apart

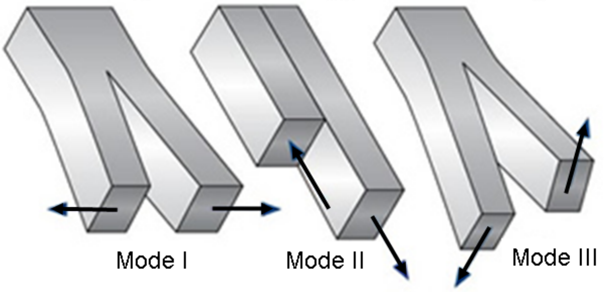

Figure 2.13: Modes of rupture.

In the engineering and scientific community the $Mode\, I$ is the most used for crack propagation in ceramics since it better represents their fracture mechanisms. It can easily be calculated by the following equation:

$$K_I = \sigma Y \sqrt{c} \tag{2.31}$$

where σ is the characteristic stress applied to the body, c is the crack length and Y is the dimensionless constant depending on the sample geometry and crack size [65].

By applying a load at the crack tip there will be a crack propagation until the critical stress is reached leading to material failure, i.e, the point where $K_I \geq K_{Ic}$. K_{Ic} is the body fracture toughness, which is a material specific characteristic independent of the sample geometry.

For the determination of K_{Ic} there are some experimental methods used in the literature [26, 66, 65] e.g. indentation techniques (Knoop, Vickers) and four point bending test. In the case of nuclear fuel ceramics, where the amount of testing material should be quite small because of the radioactive character of the samples, the most used experimental method is the indentation technique since just a small sample surface area is required for the test.

In the scientific literature for the calculation of the K_{Ic} determined by the Vickers indentation there are some relevant equations, which depend on the applied load, indent diagonal, crack length and Young's modulus to hardness ratio [67]. For nuclear ceramics Kutty [68] and Basini [69] presented the following equation, which is going to be the one used in the present work:

$$K_{Ic} = 0.016 \left(\frac{E}{H}\right)^{1/2} F \left(\frac{1}{c}\right)^{3/2} \tag{2.32}$$

where H is the Vickers hardness, E is the Young's modulus c is the crack length and d is the imprint diagonal.

Chapter 3

UO_2 Fuel Production Process

In this section some parts of the nuclear fuel fabrication process are going to be exposed and explained. Those parts, which are relevant for the work will be discussed in detail.

3.1 UO_2 Powder Industrial Scale Production Process

After mining and extraction the uranium is concentrated in form of 'yellowcake', which is a uranium concentrate obtained from leach solutions. This 'yellowcake' is converted at a conversion plant to gaseous uranium hexafluoride, which is enriched at an enrichment facility and delivered in a solid state to a reconversion plant where the uranium hexafluoride is finally converted to the uranium dioxide powder either by dry or wet route conversion processes.

From this point on the UO_2-fuel fabrication process can be presented in four production steps:

- Reconversion or Conversion Process
- Pellet Production
- Fuel Rod Assembling
- Fuel Element Assembly

In the reconversion process we have the transformation of the enriched UF_6 into the UO_2 powder. In the second step, the ceramic pellet production process, the UO_2 powder is blended, milled, compacted and finally granulated. The granulated powder is then pressed into a cylindrical body, sintered and ground for obtaining their final shape. Afterwards they are qualitatively inspected and delivered to be filled in the fuel rods, which later are assembled together into fuel assemblies.

In figure 3.1, in a simplified way, the whole fuel fabrication process is shown.

The reconversion and the pellet production steps are going to be discussed and explained in some more detail.

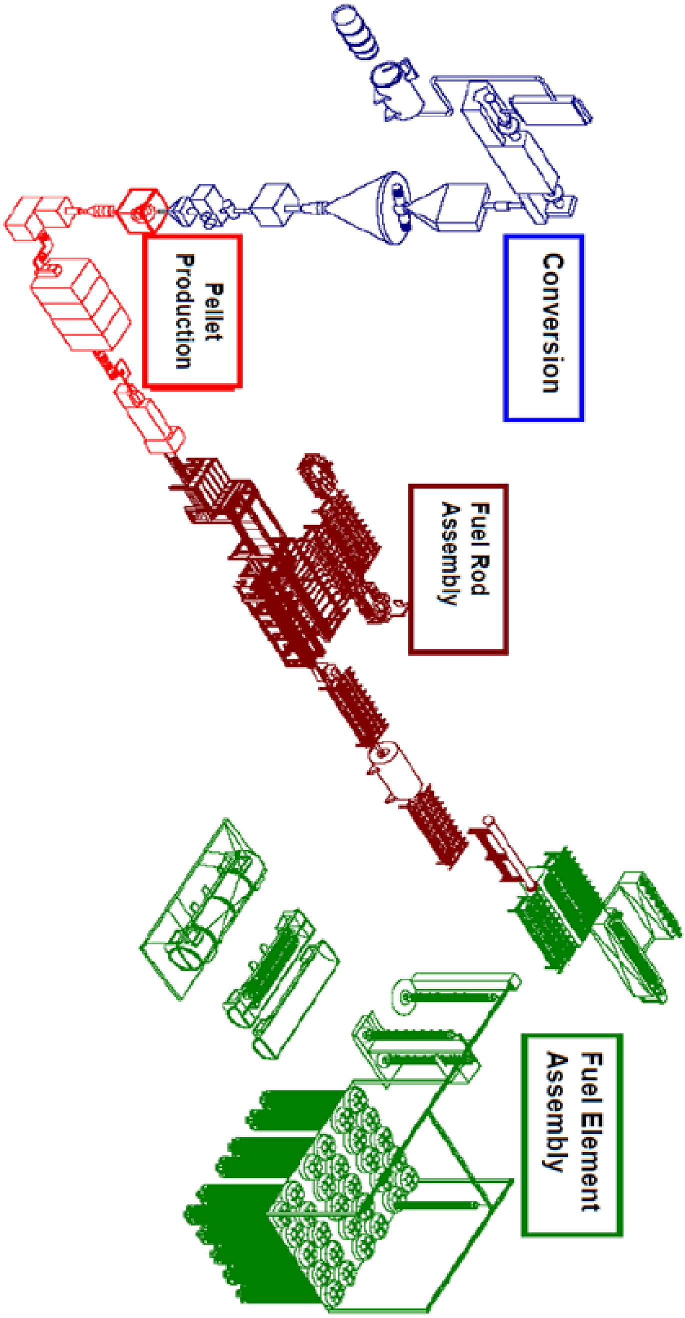

Figure 3.1: Fuel fabrication process. [Courtesy AREVA NP]

3.1.1 The Reconversion or Conversion Process

To transform the enriched uranium hexafluoride (UF_6) in the uranium dioxide (UO_2) powder different processes can be used. Basically there are two well known ways of producing the UO_2-powder – through wet conversions where there is the hydrolysis of the UF_6 by water or steam and through dry conversions where there is a reaction of the gaseous UF_6 forming an aerosol [12]. Both ways have the same process route i.e. high-temperature conversion of UF_6 to the final UO_2-powder having the desired physical and chemical properties for the fuel production.

The choice among all existent wet and dry conversion processes is not only governed by the most economic way removing of the fluorine, but it must take in account the whole process having a final product UO_2-pellets meeting all the quality requirements and performing well in a nuclear reactor during many years.

Dry and wet conversion processes are now going to be presented. Since the UO_2 powder used at the present work came from a dry conversion process this conversion process will be explained in some more details than the wet ones.

3.1.1.1 Wet Conversion Processes

The two existent wet-chemical routes, which are in commercial operation are known by the name of the intermediate uranium compounds, respectively ammonium uranyl carbonate (AUC-process) and ammonium diuranate (ADU-process).

In the AUC-process a free-flowing, granular UO_2 of uniform particle size, which does not require pre-compaction and granulation before pressing is produced. This is the main advantage of AUC-process over ADU-process.

The ADU-process involves several stages comprising, as a minimum, hydrolysis of the UF_6, reaction with nitric acid, filtration of a precipitated ADU, and furnace treatment to UO_2. In both processes the intermediate uranium compounds are separated from the liquid solution by precipitation. At the end of the conversion process, the intermediate uranium compounds are converted to the uranium dioxide powder by thermal processing.

3.1.1.2 Dry Conversion Processes

The main advantages of dry processes, when compared to the wet processes, are low losses of uranium from the process and finally almost complete elimination of radioactive gaseous and liquid effluents, which are costly to be treated [70]. However the dry conversion processes have a minor disadvantage, which is the impossibility of recycling uranium scraps [12].

Four industrial designs of dry route conversion are shown here: Conversion in the oxygen-hydrogen flame, Integrated Dry Route (IDR), Fluidized Bed Conversion and Dry Conversion (DC).

1. Conversion in the Oxygen-hydrogen Flame

This process was developed in the late 70's by the General Electric Company [71] and initially was known as "GECO". The process aims the UO_2-powder production eider directly or by first producing U_3O_8 and then by hydrogen reduction the desired UO_2 [72].

The GECO dry process can be divided in two steps: first, UF_6 reacts in a flame reactor with hydrogen-oxygen or air-hydrogen flame at a temperature of at least 750 °C or higher producing a mixture of U_3O_8, UO_2F_2 and UF_4 (see figure 3.2) [12]. The solid material separated from the gas flow is regularly blown back by a high pressure gas back flushing for collection of the particulate material in a container. Second, the collected material is reduced and defluorinated in a rotary kiln by a counter-current flow of dissociated ammonia (NH_3) and steam at temperature between 450 and 700 °C [12]. The overall process reaction equation is shown:

$$UF_6 + 3H_2 + O_2 \rightarrow UO_2 + 6HF \qquad (3.1)$$

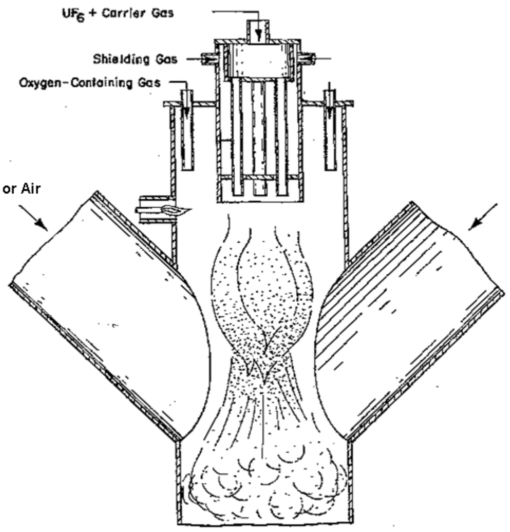

Figure 3.2: Cross section view of GECO flame reactor [9].

2. Integrated Dry Route (IDR)

The Integrated Dry Route Kiln process, which was first commercially operated in 1969 by British Nuclear Fuels Ltd (BNFL) has been adopted in France and in the USA [10]. It converts UF_6 to UO_2 in a single rotary kiln, which operates at a relatively high temperature. Solid UF_6 within a transport cylinder is vaporized by heat and metered into the kiln where it undergoes the overall reactions 3.2 to 3.4 as it passes down the kiln. The vaporized UF_6 in reaction with preheated steam will produce a solid intermediate product known as uranyl fluoride (UO_2F_2) and hydrogen fluoride (HF), which is recovered after passing through a filter. The uranyl fluoride continues passing through the rotary kiln and reacts with steam forming the uranium trioxide (UO_3), which finally is reduced with hydrogen forming the desired UO_2 powder. The kiln temperature is controlled by several zone heaters such that the temperature profiles throughout the unit can be varied according to the specification requirements between $600\,^{\circ}C$ and $800\,^{\circ}C$ [12].

$$UF_6 + 2H_2O \rightarrow UO_2F_2 + 4HF \tag{3.2}$$

$$UO_2F_2 + H_2O \rightarrow UO_3 + 2HF \tag{3.3}$$

$$UO_3 + H_2 \rightarrow UO_2 + H_2O \tag{3.4}$$

The figure 3.3 is a schematic diagram of an Integrated Dry Route kiln and shows the arrangement of both the co-current and countercurrent gas flows and the off-gas filtration system. The IDR process was developed because of its relative simplicity, low environmental impact and desirable sintering properties of the produced UO_2.

3. Fluidized Bed Conversion

This system utilizes three fluidized bed reactors in series where a consistently and high quality ceramic is produced (see figure 3.4).

The uranium hexafluoride in the first reactor is converted by reactions with steam and hydrogen to a mixture of solids like UO_2F_2, U_3O_8 and UO_2 in a work temperature varying from $475°C$ to $600°C$ [11]. The first reactor follows the following equations:

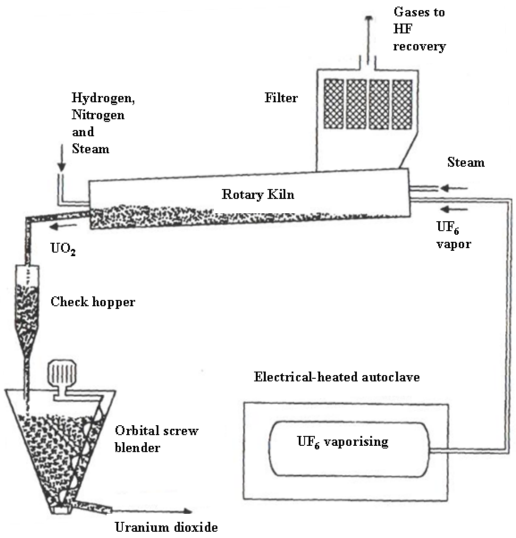

Figure 3.3: IDR process [10].

$$UF_6 + 2H_2O \rightarrow UO_2F_2 + 4HF \tag{3.5}$$

$$3UO_2F_2 + 2H_2O + H_2 \rightarrow U_3O_8 + 6HF \tag{3.6}$$

The products (UO_2F_2, U_3O_8, HF and possibly small amounts of UO_2 and UO_3) are pneumatically transferred to the second reactor in addition to steam and hydrogen being present. There the working temperature is between $575\,°C$ and $675\,°C$. The uranyl fluoride and the urania react again here in presence of additional steam and hydrogen in accordance with the following reactions:

$$3UO_2F_2 + 2H_2O + H_2 \rightarrow U_3O_8 + 6HF \tag{3.7}$$

$$U_3O_8 + 2H_2 \rightarrow 3UO_2 + 2H_2O \tag{3.8}$$

$$UO_2F_2 + H_2 \rightarrow UO_2 + 2HF \tag{3.9}$$

The final product is almost completely converted to UO_2 in the second reactor. This product consist of a fine particle UO_2 product with a residual fluorine content. In the third fluidized bed the products received from the second reactor are again under steam and hydrogen processed throughout the same equation sequence (Eq. 3.7 to 3.9) of the previous process resulting a finer UO_2 particles of high purity with a even smaller residual fluorine content of about $25\,ppm$ [12].

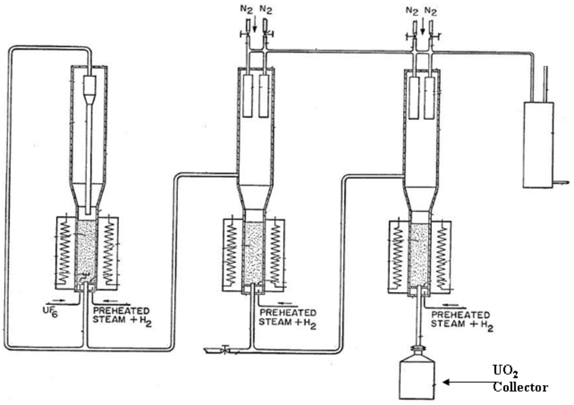

Figure 3.4: Fluidized Bed Conversion schematic [11].

4. Dry Conversion (DC) Process

The Dry Conversion (see figure 3.5) here analyzed, is a continuous process for manufacturing of UO_2 powder from UF_6. This process was developed in the late 80's in the United States by Advanced Nuclear Fuels Corporation [73]. It consists basically of the following devices:

- Autoclave for a controlled UF_6 vaporization;
- fluidized bed reactor where UF_6 is converted into UO_2;
- rotary kiln where defluorination and reduction occur;
- cooler/stabilizer for further powder oxidation and cooling. Where the powder mass and moisture is measured as well;

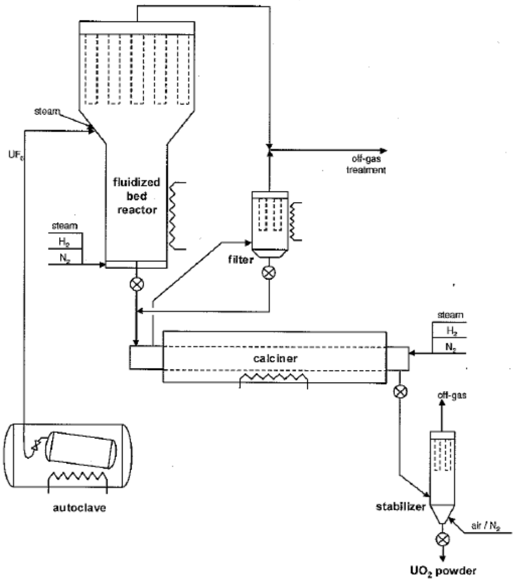

Figure 3.5: DC Process schematic [12].

- filtering and treatment of off-gases as well as recovery of the HF.

The process starts by the heating up of the solid UF_6-cylinder at an autoclave electrically heated by $\sim 90\,^{\circ}C$ proportionating a continuous extraction of gaseous UF_6, which is transported under a controlled rate to the upper part of the fluidized bed reactor. In an environment with excess of superheated steam the supplied gaseous UF_6 reacts completely according to equation 3.5 producing the solid uranyl fluoride (UO_2F_2) and the gaseous hydrogen fluoride (HF). Because of the very low powder density ($\sim 0.5{-}0.1\, g/cm^3$) part of the produced uranyl fluoride is transported along with the fluidizing gases to the metal filters overhead. These filters are regularly pressurized with a pulse of nitrogen allowing a recovery of the fluoride sediments deposited on the filters, which drop down into the fluidized bed being latter densified and agglomerated while defluorination and reduction takes place [12].

Further fluidization continues to happen at the lower part of the reactor with a mixture of preheated nitrogen-hydrogen-steam. Afterwards the powder bed is transported to the calciner where further defluorination and powder reduction takes place resulting in a nearly stoichiometric UO_2 powder [12].

In the stabilizer, the last conversion step, the powder surface is oxidized avoiding an uncontrolled oxidation during the production process [12].

3.2 Laboratory Scale Pellet Production Process

The resulting UO_2 powder used as raw material for the present work proceeded from a dry route conversion process (DC). This resulting powder will go through the laboratory scale production steps as shown in figure 3.6.

Most of the the parameters used for the pellets fabrication are within the range used by industrial fuel fabricators. This was desired since the final work can be implemented into an industrial scale production.

Most of the produced pellets have a simple cylindrical shape i.e. no specific endface design was used except for a smaller group, which was first tested before being sintered. This group of pellets had a dishing design, which does not influence much the analysis and comparisons here performed.

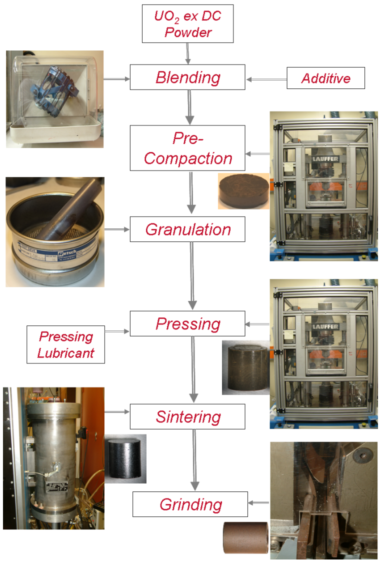

Figure 3.6: Lab scale UO_2-pellet production scheme.

In order to simplify the analysis of all pellet types produced, they are first allocated in mixing batches as can be seen in table 3.1. From these mixing batches all the UO_2 samples used in the experimental procedures are originated. Afterwards these UO_2 samples are split into three groups of different types of samples. The first group ($Gp1$) consisted of samples with different lengths and diameters without additives present (except for the pressing lubricant) in their composition. In this first group the samples were not sintered after pressing.

Brittle materials have a volume dependence to the strength. The reason for this is that the population and distribution of flaws are of a statistical nature and that the probability of

Table 3.1: Mixing Batches.

Batch	UO_2 mass [g]	Additive	Additive mass[g]	Total mass [g]
1	4037.26	-	-	4037.26
2	230.44	AZB	1.56	232.00
3	518.74	B-U_3O_8	103.85	622.59
4	197.36	Gr-U_3O_8	41.46	238.82
5	1933.22	0.3%Fibers	5.83	1891.29
6	786.18	0.2%Fibers	1.58	787.76

encountering a critical flaw is proportional to the ceramic volume if the ceramic strength is controlled by volume flaw or to surface area if the ceramic strength is controlled by surface flaws [74].

Test results of Hondros [75] show that the splitting strength increases with the diameter. However, Bazant [76] presented results from Sabnis and Mirza [77], Chen and Yuan [78], Ross, Thompson and Tadesco [79] where the splitting tensile strength results decrease with the diameter. Bazant also showed an interesting result reported by Hasegawa et al [80]. His work revealed that for small diameters the split-cylinder strength decreases as the diameter increases, but after a certain diameter is exceeded, the trend seems to reverse, i.e., the strength appears to increase, which is against the statistical theory of size effect.

So the objective of the $Gp1$ pellets group was to determine the best pellet geometry configuration by analyzing the length to diameter ratio ($L/D\,ratio$) influence to the reliability and mechanical resistance of not sintered pellets.

The second group ($Gp2$) contained pellets with different lengths, additives and sintered for different times. Finally the third group ($Gp3$) composed of samples produced according to the obtained testing results from $Gp2$. In fact the $Gp3$ samples are those having some parameters from $Gp2$ samples, which presented the best benefits to the mechanical resistance as a whole. Furthermore, pellets with another variety of green density as well as different amounts of additives were also introduced.

In chapter 5 a detailed explanation for the selection of the $Gp2$ and $Gp3$ samples as well as their test results can be found.

3.2.1 Blending

With the blending step a perfect homogenization between the UO_2 powder and the additives is desired. In an industrial scale the materials to be blended are separately added to the conical screw hopper blender and with an orbiting screw it is blended (see figure 3.7). In the laboratory the UO_2 powder and the additives were initially manually homogenized and after that mixed for approximately $20\,min$ in a small Turbula T2C tumbler (see figure 3.6)with a bin volume of approximately $1\,l$ for a perfect homogenization.

In table 3.1 the six powder batches can be found.

Figure 3.7: Conical screw hopper blender with orbital screw blender.

3.2.2 Pre-compaction

In the industry a roll compactor is used to pre-compact the powder. The powder will be pressed between two rolls, where one of them is fixed whereas the other, through a hydraulic system, will press the powder with a pre-stablished pressure. This pressure can be controlled. The rolls have axial corrugations, which give to the powder the form of small rods with density of $4.5\,g/cm^3$. The great advantage of this method is that very high pressures can be exerted continuously on moving material [12].

In the laboratory the powder was pre-compacted by another method at an uniaxial Lauffer electro-hydraulic press (see figure 3.6). The applied pressure was set between 16 and $24\,MPa$ and the resulting slug had a density of approximately $4.5\,g/cm^3$.

3.2.3 Granulation

This is the last powder preparation step in the production line. In the laboratory the compacted slugs were manually forced-sieved through a $1.18\,mm$ screen mesh (see figure 3.6) producing granules, which are going to be pressed to the final cylindrical pellet shape. With this process the flowability and the compressibility of the powder is improved.

In an industrial scale the compacted material is pressed and crushed through the sieve by a slow rotating rotor forming granules of a well-defined size, which is given by the mesh size of the sieve [12].

3.2.4 Pellet Pressing

Pressing or compacting powders is a procedure with diverse influencing factors such as powder flowability, particle size, powder density, addition of additives, pressing and powder temperature, friction among particles, plastic deformation of particles, rearrangement and densification of particles, etc. In fact, because of this wide variation possibilities a standard process, even for similar powders, can not be established since a slight change at the powder characteristics may affect the quality of the final product.

Pressing a powder bed confined in a die can not be compared to a fluid under pressure, which transmits changes in pressure at a certain point directly and uniformly throughout its mass. In the case of powders confined in a die the transmission of the applied forces decreases not uniformly through the powder bed but according to the stress pattern imposed by the die-wall restraint [81], which results in the undesired density gradients inside the green compacts affecting their future shrinkage during sintering producing asymmetrical sintered bodies.

In order to optimize the pressing process numerical modeling started to be applied by the industry. In phenomenological approaches, which are continuum mechanical modeling the powder is macroscopically considered and it is treated as a continuum medium [82]. Most of the phenomenological models such as Drucker-Prager cap model [83], Cam-Clay model [84] and the DiMaggio-Sandler model [85] were first developed for the soil mechanics and later were adapted for the specific situation of powder compaction [86]. In these models the powder is considered as a porous media and is characterized by overall powder parameters e.g. Young' s modulus, Poisson's ratio, interparticle friction and cohesion [82].

The compaction of powders could be divided in:

- die filling,
- powder pressing,
- and compact ejection.

By the first considered aspect, the filling of the die, the most important characteristic is the flowability of the powder where powder particles with a low flowability behavior resist to freely flow into the die resulting in a not steady compaction for instance during a high production rate, since the die will not be completed filled. In our specific case, with a small laboratory scale production, the flowability effect during the die filling could be neglected because the amount of powder handled is small and is constantly controlled according to its flowability characteristics.

As for the powder pressing, the rearrangement of the particles, the presence of shear and compression stresses and the friction among particles as well as among particles and die-wall and pressing punches should be considered. Actually, the powder pressing step can be said to be the most complex and important part of the whole compaction process and will be explained in the next section. Finally, we have the compact ejection, the phase where the compacted powder is pushed out by the lower punch. In the prior phase different density distribution patterns were developed in the green body and therefore it is necessary to reduce gradually the applied stress during unloading the applied pressing stresses, which developed different density distributions patterns in the green body, have to be reduced gradually in order to allow the behavior known as elastic springback effect. Moreover, if the springback effect is not controlled in those regions where the plastic dilatation occurs there can happen a localized softening and crack formation [87]. In many cases these cracks, similar to those shown in figure 3.8 from a microsection of a sintered pellet, lead to the so-called endcapping failure of the compact.

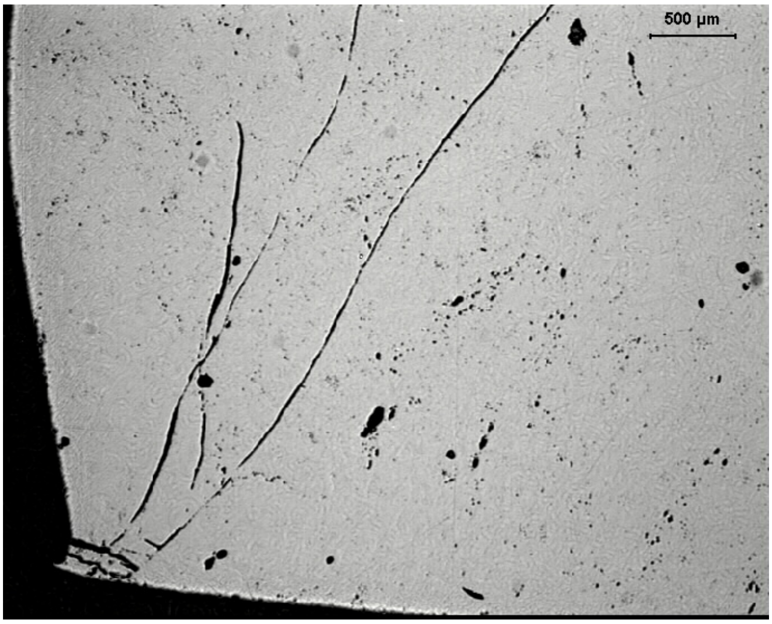

Figure 3.8: Microsection of a UO_2 pellet with green density of $6.3\,g/cm^3$ and sintered under H_2 for 3 hours. The picture shows the development of shear stress cracks at approximately 45° to the pressing direction starting at one of the end-faces of the pellet.

3.2.4.1 Powder Pressing

At the first moments of the compression process the particles are usually loose inside the die. As the relative density increases through compressive and shear stresses they are rearranged through plastic deformation sliding over each other resulting in a cold welding among them [88].

For the description of this process showing the volume reduction more than 15 equations can be compiled in the literature, which means that there is no generally acceptable equation to represent all situations [89].

The following pressing description was extracted from Thompson [14], which was based on the experiments performed by Unkel [13]. Thompson tried to express to cylindrical compacts the stress and density distribution in terms of friction and geometry namely the length to diameter ratio ($L/D\, ratio$). His approach analysis is important because the stress distribution plays an important role in the tendency of the green body to crack or end-cap during punch withdraw and ejection, while the distribution of green density strongly affects the local shrinkage during sintering.

Macleod [81] published some years before Thompson's experimental study of the density distribution in ceramic compacts using autoradiography. With his results and Thompson's mathematical development a good understanding of the pressing process can be achieved.

An important remark from Macleod's work and Thompson's model is that both were developed by using single-acting pressing. This does not invalidate the usage of their analysis in case of a double-acting pressing is applied since essentially it would just result in a reduction of the $L/D\, ratio$ in half as is shown in figure 3.9.

The stress distribution schematic adapted from Unkel's tests is shown in figure 3.10. From it Thompson deduced the following equations:

$$\sigma_z(r,z) = Br^2 e^{(4\alpha\mu/R)z} + C(1 - r^2/R^2) \tag{3.10}$$

$$\tau = \frac{\alpha\mu r^3}{R} e^{(4\alpha\mu/R)z} \tag{3.11}$$

where σ_z and τ are the axial normal and shear stresses in the powder respectively and B and C are constants. The powder to die-wall friction coefficient is represented by μ. It is is undoubtedly the most influencing factor during pressing and without it no endcapping and no density or pressure gradients would be present in the green bodies [81, 14]. It can be reduced by the directly addition of lubricants to the die-wall or by adding the lubricant to the powder. The radial-to-

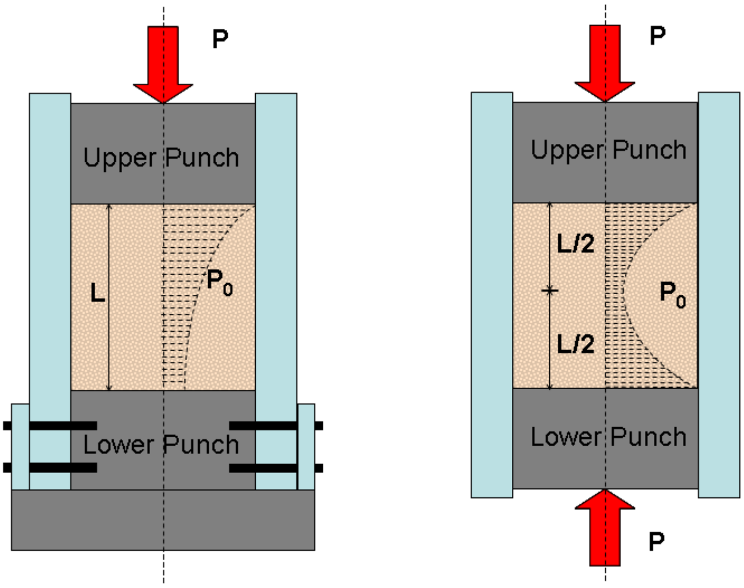

Figure 3.9: Single and double acting pressing effect on the $L/D\,ratio$.

axial compaction stress is here represented by α, which is a measure of the powder flowability. With a large α there will be an increase of the normal die-wall stress, which together with μ produces higher die-wall shear stresses finally resulting in increased endcapping stresses. One could propose that by applying lubricants there would be a reduction in μ, what is true, but however, the addition of lubricants has an adverse effect on α. So that is why a compromise between α and μ should be found. Another influencing factor on α is the shape of the particles. Flattened particles have smaller α than the spherical ones [14].

The powder/die-wall friction ratio can be calculated by the following equation:

$$\mu = \frac{D}{4L}\frac{\sigma_B}{\sigma_r}\left(\frac{\sigma_T}{\sigma_B}\right)^{\frac{z}{L}} ln\frac{\sigma_T}{\sigma_B} \tag{3.12}$$

where σ_T is the top punch stress, σ_B is the bottom punch stress and σ_r is the radial stress.

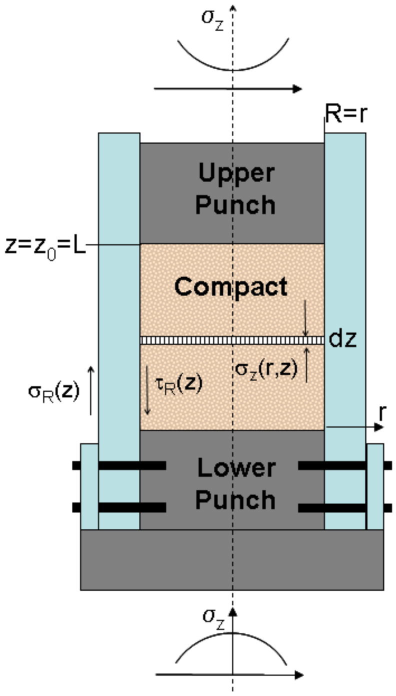

Figure 3.10: Schematic of cylindrical compaction with stress components [13, 14].

To continue with the mathematical development it is necessary to specify the two constants B and C. For this purpose two boundary conditions are employed:

1. The integrated compaction pressure at the punch face is equal to the punch force,
2. and, the density distribution in a compact is such that it has a constant mass independent to which extent it is pressed.

The first boundary condition can be written as follows:

$$F_0 = \pi R^2 P_0 = \int\limits_0^R 2\pi r \sigma_z(r, z_0) dr \tag{3.13}$$

where F_0 is the punch force, is the average compaction pressure at the punch face and z_0 is the axial position of the punch face when the powder is fully compacted, i.e. the entire compact length L. By analyzing equation 3.10 at z_0, then substituting the result into equation 3.13 and integrating will result in an equation for B in terms of C:

$$B = \frac{1}{R^2}(2P_0 - C)e^{(-4\alpha\mu/R)z_0} \tag{3.14}$$

Finally substituting equation 3.14 in equations 3.10 and 3.11 will result in:

$$\sigma_z = (2P_0 - C)\frac{r^2}{R^2}e^{(-4\alpha\mu/R)(z_0 - z)} + C(1 - r^2/R^2) \tag{3.15}$$

$$\tau = (2P_0 - C)\frac{\alpha\mu r^3}{R^3}e^{(4\alpha\mu/R)(z_0 - z)} \tag{3.16}$$

which have now just the constant C. Both equations can be written in a normalized form by substituting $z_0/R = 2L/D$, becoming equation 3.17 and finaly equation 3.18.

$$\sigma_z/P_0 = (2 - C/P_0)\frac{r^2}{R^2}e^{(-8\alpha\mu L/D)(1 - z/L)} + (C/P_0)(1 - r^2/R^2) \tag{3.17}$$

$$\tau/P_0 = (2 - C/P_0)\frac{\alpha\mu r^3}{R^3}e^{(-8\alpha\mu L/D)(1 - z/L)} \tag{3.18}$$

The mathematical development has reached for the first time a point where the $L/D\,ratio$ is explicitly mentioned. This ratio together with α and μ are the most representative factors determining the pressure and density distribution.

Before getting to the second boundary condition some comments about the compaction stress on the central axis, C, need to be given. C, is never greater than the average punch face pressure, P_0. In order for the relation C/P_0 to reach the unity, i.e. a point where all the applied stress is transmitted uniformly to the whole compact resulting in a perfect green body, the terms α, μ and L/D need to be zero. If these terms are non-zero, which is the situation at normal pressing condition, a point of equilibrium among these parameters should be established. By reduction of the C/P_0 ratio there will be an increase of the pressure gradients, which will reduce the compact uniformity and increase the probability of endcapping [14].

The second boundary condition states that the density distribution in a green body is such that its mass during pressing remains constant regardless the applied pressing stress. This condition is necessary to be fulfilled because C is a measurement of the stress distributed all over the compact. This fulfillment can be analyzed prior to the compaction by:

$$m = \pi R^2 z_i \rho_i \tag{3.19}$$

where m is the powder mass, z_i is the punch displacement and ρ_i the powder density before pressing and after the compaction is done:

$$m = \int\limits_0^R \int\limits_0^L 2\pi r \rho dr dz \tag{3.20}$$

where ρ is the green body density distribution and L is the compact length.

C can be then calculated by equation 3.21 [90].

$$C = 2P_0 \frac{\frac{P_B}{P_0} - e^{\frac{-4\alpha\mu L}{R}}}{1 - e^{\frac{-4\alpha\mu L}{R}}} \tag{3.21}$$

where P_B is the reaction of the bottom punch to the applied stress from the top punch. For a double acting press P_B and P_0 can be considered identical reducing equation 3.21 to:

$$C = 2P_0 \frac{e^{\frac{-4\alpha\mu L}{R}}}{1 - e^{\frac{-4\alpha\mu L}{R}}} \tag{3.22}$$

In figure 3.11 it can be observed the diameter variation of green and sintered pellets in some of the produced pellets for this work, showing in a practical way what was here tried to be explained with mathematical equations. In figure 3.12 it is shown the increase of the pressing load while the upper punch moves toward the powder in the die. Finally in figure 3.13 it is shown the density development while the stress is increased against the pressed powder.

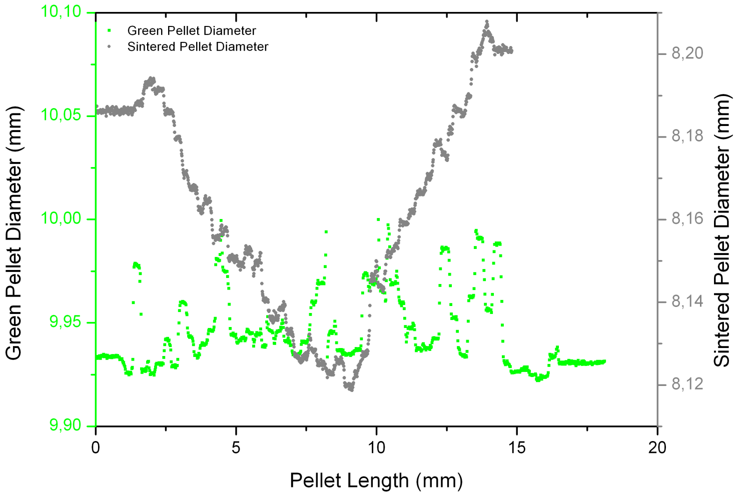

Figure 3.11: Pellet diameter variation.

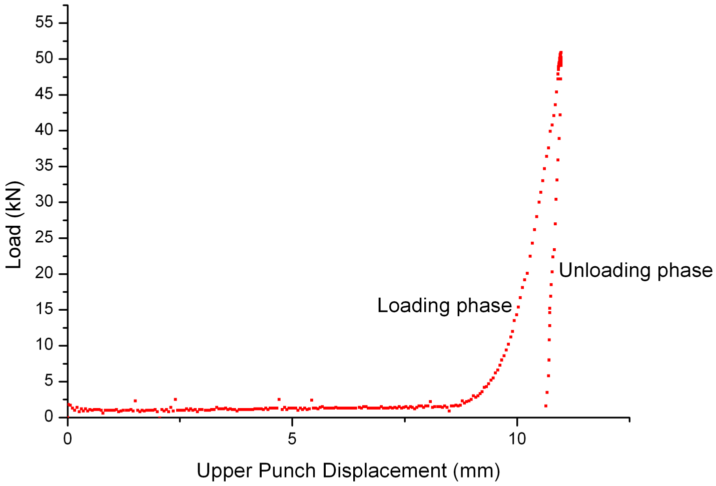

Figure 3.12: Pressing load development.

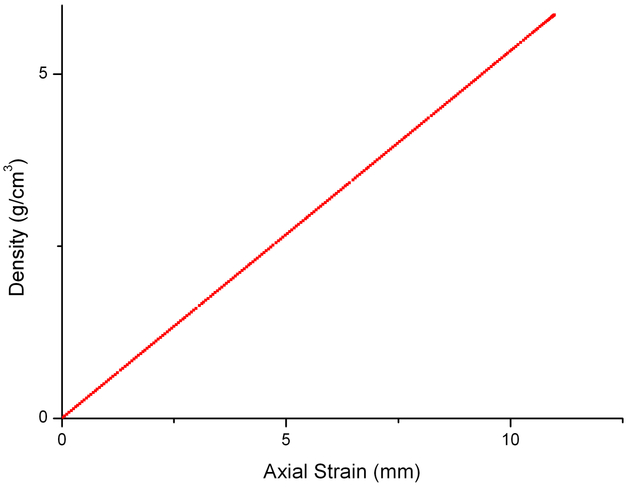

Figure 3.13: Density increase during pressing.

3.2.4.2 Green Compact Ejection

The ejection of the pressed green compact is a complex step of the pressing process. Similarly to any plastic deformation, elastic strain remains in the material until the pressure is relieved either in the powder compact itself or in form of residual radial stress while the compact is ejected from the pressing die [88]. In fact, a direct consequence of the residual radial stress, σ_{r0} that a substantial force is required to eject a powder compact from the compacting die [15].

By having a green compact with height L and a cylindrical die with diameter D_d we have a die cross-sectional area of $\pi D_d^2/4$ and a lateral area of $D_d \pi h$. With this information the ejection force can be determined as [15]:

$$F_E = \mu D d h \sigma_{r0} \tag{3.23}$$

where F_E is the bottom punch ejection force applied to the compact. The corresponding ejecting pressure can be expressed as:

$$P = \frac{F_E}{\pi D_d^2/4} = \frac{\sigma_{r0} 4 \mu h}{D_d} \tag{3.24}$$

In [15] a schematic diagram (figure 3.14) was plotted showing the ejection forces applied to a compact. The author named the peak pressure value as adhesive friction, which in certain cases may reach values above the compacting pressure, and sliding friction level where the compact slides out of the die. Excessive increase of the ejecting pressure is a possible indication cold-welding (for metallic powders) in the die, which is caused either by an overworked die or by insufficiently lubricated die, and which has a typical stick-slip behavior (creaking noise).

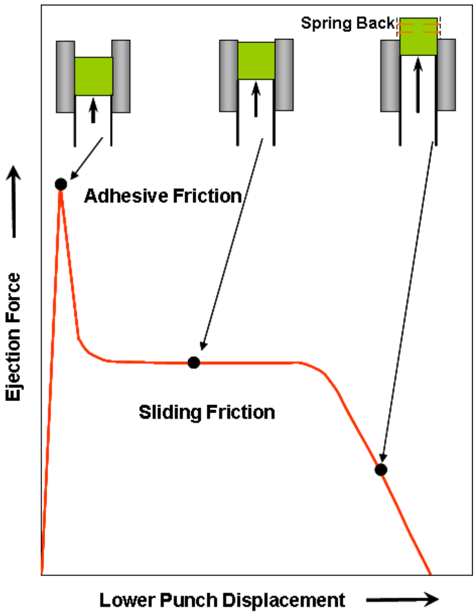

Figure 3.14: Schematic of the ejecting force as a function of the movement of the ejecting lower punch [15].

When the compact passes the upper rim of the die, its upper part expands elastically while the lower part is still under the influence of the residual radial stress. In such situation horizontal shearing stress are produced and may generate horizontal cracks in the compact [15].

According to Smith [88] the compression of brittle materials with density variations along the compact may develop shear stresses at 45° angles to the pressing direction and that secondary tensile stresses develop among planes parallel to the compression axis. Moreover, if the shear stresses are greater than the green strength of the material then shear cracks or laminate at the compact boundary may occur.

One of the reasons why cracks should be avoided during pressing is because during sintering these parts do not heal completely [88] and are left behind as can be observed in the already presented figure 3.8.

The elastic expansion of the compact after ejection, the so-called spring back effect can be determined by the following equation [15]:

$$S = \frac{100(\lambda_c - \lambda_d)}{\lambda_d} \tag{3.25}$$

where S is the spring back, λ_c is the transversal dimension of the ejected compact and λ_d is the dimension of the compact die. The spring back depends on the compacting pressure, compacting density, powder characteristics and shape and elastic properties of the die [15].

The reduction the spring back effect and cracking in compacts can be achieved by an higher lubricant content, by rounding the edges of compact exit [15] and also by the application of a small down-holding force by the upper punch.

3.2.4.3 Experimental Pressing Procedure

For a better pressing behavior i.e. a better load distribution a small amount of a solid lubricant, $0.24\,\%$ of the total mixed mass, was applied to the mixing batches. It was mixed to the UO_2 granulate at the Turbula T2C tumbler (see figure 3.6) for approximately $15\,min$ before pressing. Milled aluminum-di-stearate (ADS) was used for lubrication. The reason why the lubricant is just added after the granulation is because it does not make any sense to lubricate the interior part of the granules since the idea of its use is to reduce the friction forces between the die walls and the granules.

After granulation and lubrication the mixing batches are now ready to be dry pressed. The pressing was performed at the same Lauffer press used for the compaction. Two different green densities were selected for testing, where the lowest one being approximately $5.85\,g/cm^3$ and the highest one was about $6.22\,g/cm^3$.

The load applied for pressing the pellets with the lowest green density was between $16-26\,KN$ and between $37-60\,KN$ for the highest. The down-holding force, applied by the upper punch during pellet ejection, was set at $\sim 0.3\,KN$. For reaching these desired load values several experimental pre-runs were carried out. That's because the press adjustment varies a lot according to the type of UO_2 powder and additives combination. This forced us to make a different adjustment for every single type of pellet pressed.

Each produced green pellet was measured on its length, height and mass, which were used for geometrical density calculation. The summarized data for the different pellet types produced for the first and second testing groups, $Gp1$ and $Gp2$, can be seen in table 3.2 and 3.3. In table 3.4 can be seen the third group of pellets, $Gp3$, produced after the obtained test results from the $Gp2$.

The type identification in $Gp1$ pellets expresses their average diameter and length. So the designation $D6L9$ for example indicates that in this sample type the pellets have an average diameter of $\sim 6\,mm$ and an average length of $\sim 9\,mm$.

Pellets D and L have the same additive, AZB, in their composition. They differ from each other by the moment when the additive was added to the UO_2 powder. By pellets D the AZB was added at the blending step before the granulation, while by the pellets L it was added after the granulation step. This procedure is used by some fuel manufacturers as a safety step since it reduces even more the possibility of a spontaneous chain reaction be trigged.

Table 3.2: Gp1 Green Pellets.

Type	Samples	Mass/unit [g]	Length [mm]	Diameter [mm]	Density [g/cm^3]	ADS [g]
D6L9	31	1.57±0.05	9.181±0.334	6.092±0.004	5.88±0.06	0.13
D6L13	31	2.21±0.05	13.120±0.220	6.104±0.015	5.78±0.07	0.18
D6L18	34	3.04±0.04	18.078±0.312	6.103±0.011	5.75±0.06	0.27
D8L9	30	2.69±0.06	9.122±0.234	8.100±0.006	5.72±0.05	0.21
D8L13	30	3.93±0.05	13.166±0.193	8.107±0.009	5.78±0.06	0.31
D8L18	30	5.45±0.11	18.255±0.365	8.119±0.004	5.77±0.06	0.43
D8L9	30	4.72±0.17	9.238±0.330	106.58±0004	5.72±0.09	0.37
D8L13	30	6.83±0.14	13.278±0.278	10.667±0.003	5.76±0.02	0.54
D8L18	30	9.38±0.14	18.184±0.309	10.672±0.006	5.76±0.06	0.74

3.2.5 Sintering

After pressing, the pellets are now ready to be sintered. Sintering is a forming process explored by the humanity for thousands of years especially ceramic and also for producing metals. It consists in forming bonds among particles of a previously compacted body by the application of heat, aiming either densification or coarsening of the green sample. The first objective, the densification, relates to the reduction of the total surface free energy, which implies in pore shape

Table 3.3: Gp2 Green Pellets.

Type	Samples	Mass/unit [g]	Length [mm]	Diameter [mm]	Density [g/cm^3]	Additive	Add. [g]	ADS [g]
A	34	6.02±0.03	13.361±0.072	9.903±0.002	5.86±0.02	—	—	0.56
B	35	6.09±0.05	13.505±0.102	9.903±0.002	5.85±0.02	—	—	0.57
C	34	6.06±0.04	13.470±0.114	9.901±0.003	5.84±0.02	—	—	0.56
D	34	6.14±0.05	13.677±0.135	9.905±0.001	5.83±0.03	AZB	1.56	0.56
E	35	5.99±0.04	13.361±0.098	9.899±0.002	5.83±0.02	B-U_3O_8	39.84	0.57
F	35	6.10±0.04	13.573±0.079	9.901±0.002	5.84±0.02	Gr-U_3O_8	41.46	0.57
G	34	6.06±0.04	13.418±0.102	9.905±0.007	5.86±0.02	Kreatin (0.3wt%)	0.7	0.56
H	35	4.1±0.02	9.108±0.052	9.893±0.003	5.85±0.02	—	—	0.4
K	34	8.17±0.06	18.211±0.125	9.904±0.001	5.83±0.01	—	—	0.77
L	35	5.99±0.04	13.264±0.1	9.904±0.001	5.86±0.02	AZB	1.7	0.57
SQ-Std.	21	6.02±0.03	13.361±0.072	9.903±0.002	5.86±0.02	—	—	0.34
SQ-Keratin.	21	6.06±0.04	13.418±0.102	9.905±0.007	5.86±0.02	Kreatin (0.3wt%)	0.43	0.34

Table 3.4: Gp3 Green Pellets.

Type	Samples	Mass/unit [g]	Length [mm]	Diameter [mm]	Density [g/cm^3]	Additive	Add. [g]	ADS [g]
M	38	8.94±0.09	18.621±0.173	9.919±0.004	6.21±0.02	—	—	0.92
N	39	8.24±0.10	18.231±0.234	9.920±0.006	5.85±0.03	—	—	0.89
P	38	8.80±0.05	18.369±0.095	9.913±0.004	6.20±0.03	—	—	0.92
Q	40	8.20±0.08	18.216±0.170	9.906±0.005	5.84±0.02	Keratin (0.3 $wt\%$)	1.14	0.91
R	39	8.68±0.07	18.190±0.129	9.905±0.006	6.18±0.03	Keratin (0.2 $wt\%$)	0.79	0.95
S	40	8.75±0.08	18.285±0.168	9.903±0.004	6.22±0.02	Keratin (0.3 $wt\%$)	1.21	0.97
T	38	8.90±0.06	18.660±0.121	9.907±0.003	6.19±0.01	B-U_3O_8	64.01	0.92
U	38	8.26±0.07	18.251±0.153	9.926±0.010	5.85±0.04	Keratin (0.3 $wt\%$)	1.14	0.91
V	37	8.81±0.06	18.340±0.159	9.914±0.003	6.22±0.02	Keratin (0.2 $wt\%$)	0.79	0.95
X	38	8.80±0.09	18.380±0.187	9.914±0.005	6.20±0.03	Keratin (0.3 $wt\%$)	1.21	0.97

change, pore and sample shrinkage and grain growth. The second one, the coarsening, besides the fact of also leading to a decrease of the total surface free energy, change in porosity shape and size as well as grain increase, is also responsible for an increase of the compact strength without any net dimensional change through surface diffusion or evaporation-condensation [17]. In fact the driving force for sintering to happen is the powder compact solid-vapor surface area reduction, therefore decreasing the total surface free energy [91].

Smaller particles have a higher surface area and consequently a higher surface energy i.e. more energy per unit volume is available, which can allow a faster sintering process [17]. In addition to that it can be observed at equation 3.26, in which σ_{sp} represents the stress on a spherical particle, D_p the particle diameter and γ the surface free energy, that if D_p increases ($D_p \rightarrow \infty$) the stress tends to decrease ($\sigma_{sp} \rightarrow 0$). In other words the stress, i.e. energy, present in the curvature of the particles directs the mass flow in order to give these particles flattened surfaces after the sintering [17].

$$\sigma_{sp} = \frac{4\gamma}{D_p} \tag{3.26}$$

Some of the influencing parameters of the sintering process are listed bellow:

- the sintering temperature and its heating rate,
- the sintering dwell time,
- the sintering atmosphere,
- the particle size,
- the stoichiometry,
- the additives and,
- the compact green density.

After determining some of the powder and pressed compact characteristics, for instance powder particle size, powder density, compact green density and powder stoichiometry, the sintering parameters i.e. the sintering temperature, isothermal time and atmosphere can be established.

The sintering process is quite dependent on the temperature since at higher temperatures the rate of sintering is increased. As already said before, the smaller the particle, the greater will be the driving force of sintering - the surface free energy. By elevating the sintering temperature the rate and the magnitude of the changes occurring in the process are greatly increased. Furthermore, for sintering to happen, it is also necessary, besides the intrinsic powder surface free energy, that sufficient external energy in form of heat is present in order to enable the mass transport, i.e. the mobility of atoms in the compact. In the graph of figure 3.15 it can be seen that the higher the sintering temperature the higher will be the sintering rate showing how sensitive the sintering process is to the temperature.

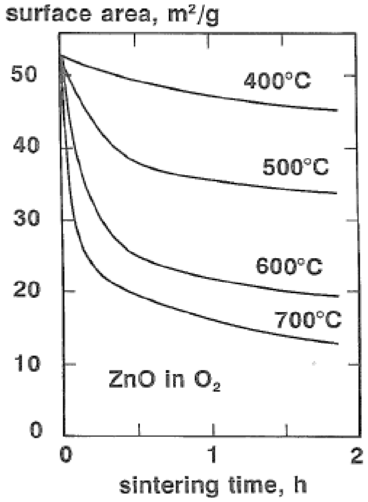

Figure 3.15: Graph from Gray [16]presented by [17] showing the specific surface area of zinc oxide versus isothermal sintering time for four temperatures. The surface area energy as well as the sintering rate are quite high at initial stages of sintering, however with extended time both of them reduce.

The sintering time is dimensioned and established for allowing the green compacts to reach the desired characteristics after sintering. Un-necessarily increased sintering time lead to higher expense in the sintering process since there will be a reduction of productivity. On the other hand a decreased sintering time may produce sintered compacts with smaller density, higher porosity, smaller grains and lower strength.

The rate of sintering decreases with increasing time [27]. In figure 3.15, besides the temperature aspect previously mentioned, it is also show that the largest change in a compact shows up at the earliest periods of sintering since by this time the surface area and consequently the surface free energy are higher allowing a faster sintering rate when compared to the later periods.

Both sintering time and temperature need to be established together for a sintering process, however a slight increase in the temperature may be much more effective in producing changes in the sintering of a compact than hours and hours of sintering.

The sintering atmosphere has also a considerable influence on the final characteristics of a sintered compact. Different composition of atmospheres are applied in order to improve the microstructure of the compacts, which directly influence on their final density, strength and plasticity.

In the case of a nuclear fuel the sintering atmosphere can be configured by the variation of the oxygen partial pressure in oxidizing, slightly reducing and reducing [92]. These atmosphere configurations can be applied to sinter e.g. green pellets produced with powder from different conversion routes (ex-AUC, ex-ADU, DC), with powders containing additives and powders containing other forms of uranium oxides (U_3O_8, U_4O_9). This will result in different as-sintered pellets characteristics, for instance the formation of a bimodal grain size distribution by a high oxygen partial pressure in the sintering oxidizing gas by ex-AUC (ammonium uranyl carbonate) powder while by ex-ADU (ammonium diuranate) and DC (dry conversion) monomodal structure is found [93].

By sintering under an oxidative atmosphere (OA), e.g. under CO_2, there is first the densification of the compact, governed by the lattice diffusion of uranium, and then at a second stage there is the reduction of the as-sintered uranium dioxide by changing the sintering atmosphere to H_2 (see figure 3.16 [93]). As for the sintering under a reducing atmosphere (RA) the pellets are always exposed to a $100\% \, H_2$ atmosphere, known as dry atmosphere, or to mixed atmospheres containing H_2 with up to $3 \, vol\%$ of H_2O or CO_2, wet atmosphere or even under H_2 containing different concentrations of N_2. Finally, the slightly RA is the one where a larger amount of H_2O or CO_2 is mixed to the H_2 [92].

The sintering process with an OA has some advantages to the one with a constant RA such as lower sintering temperatures,~ 1100 °C, which reduces the energy costs (for RA the temperature is raised to ~ 1700 °C) and consequently reduces the refractories and insulations expenses, also shorter sintering time and finally the usage of CO_2 instead of H_2, which is more expensive and dangerous, in some stages in the furnace. The great disadvantage of the OA sintering process is the complexity of the continuous sintering furnace. Especially in this case it is required that materials used inside the furnace, such as the heating element and the sintering boats, withstand the oxidative atmosphere at elevated temperatures. The construction and operation of a continuous furnace with two chambers separated by a gas lock is still not completely developed and that's why the sintering process under RA is the standard process used worldwide.

3.2.5.1 Sintering Stages

The transformations occurring during the sintering process is divided in 'stages'. A sintering stage may describe according to Coble [18] as a period of geometric change in which the pore shape change is totally defined or an interval of time during, which the pore remains constant in shape while decreasing in size.

In the scientific literature [33, 18, 94] it is quite common to find that the sintering process

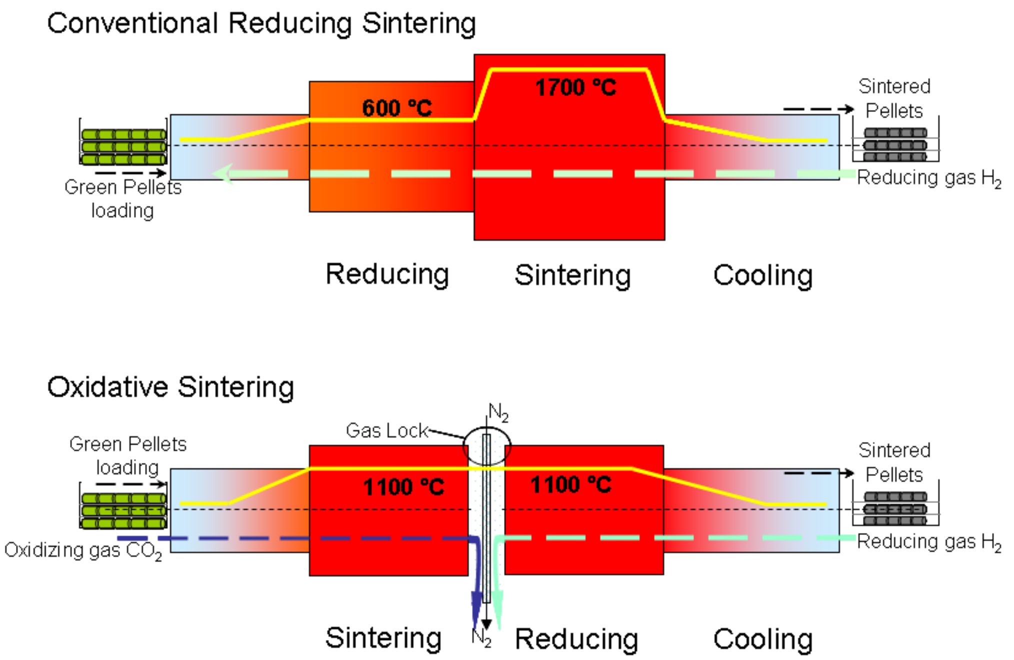

Figure 3.16: Rough schematic showing the oxidative and reducing sintering processes.

divided in three sequential stages, however a refinement introduced here by Ashby [19] includes the so-called *stage* 0, which is characterized by the instantaneous neck-formation caused by interatomic forces when powder particles are first put in contact. The other sintering stages are the *stage* 1 where there is the neck growth, the *stage* 2, the intermediate stage, characterized by porosity rounding, densification and grain growth [17], and finally the *stage* 3, the final stage, the porosity is expected to be drastically reduced.

A nice graphical representation, by Coble [18], of the sintering stages is shown in figure 3.17. There it can be seen how spheres in their initial tangential contact develop up to the final sintered tetrakaidecahedron structure.

The term 'sintering' refers to the change in pore shape, pore shrinkage and grain growth, which particles in contact undergo during heating [18]. Moreover, according to Ashby [19] this microstructure modification during sintering may involve at least 6 mechanisms (most of them are related to the diffusive transport of matter to the growing neck), as can be seen in table 3.5, all of them contributing for a final common objective of neck growth and the last three also leading to densification of the compact.

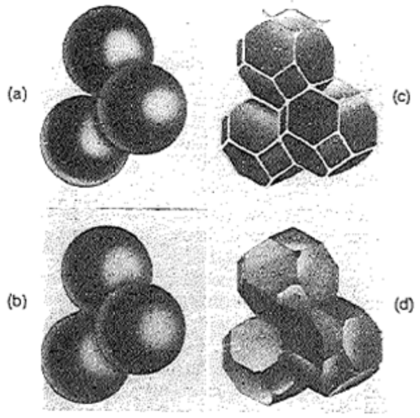

Figure 3.17: (*a*) Initial stage of sintering; model structure represented by spheres in tangential contact. (*b*) Near end of initial stage. Spheres have begun to coalesce. The neck growth illustrated is for center-center shrinkage of 4%. (*c*) Intermediate stage; dark grains have adopted shape of tetrakaidecahedron, enclosing white pore channels at grain edges. (*d*) Final stage; pores are tetrahedral inclusions at corners where four tetrakaidecahedra meet [18].

To determine which mechanism acts at a specific sintering stage and its contribution to the process is a complex matter since the presence of impurities, the presence of more than one component in sintering system, the variation of the stoichiometry, the application of pressure during sintering, etc. will certainly imply in a variation of the entire diffusion process [19].

A simpler way of analyzing the acting mechanisms during the different sintering stages was proposed by Ashby [19], the sintering diagram, where the dominant sintering mechanism and the net rate of neck-growth or densification is presented as a correlation between neck size and temperature. The diagram axes are the so-called homologous temperature, T/T_M, where T is the sintering temperature and T_M is the substance melting point (both temperature values in $^{\circ}C$), and the normalized neck radius, x/p_r, where x is the radius of the disc of contact of two particles and p_r is the particle radius. In the fields determined by the axes there is a dominant sintering mechanism contributing mostly to the neck growth. Contours of constant sintering time show the neck size after a specific time. The unshaded fields describe the mechanisms, which lead to densification, so for a higher density the sintering should be performed in an unshaded field.

In figure 3.18 is presented an Ashby sintering diagram for the stoichiometric UO_2 [19] in which the particles in $stage\,0$ form necks caused by interatomic forces. In $stage\,1$ the dominant sintering transport mechanism is the surface diffusion. In order to simplify the analysis $stages\,2\,and\,3$ are in the diagram presented together. Nevertheless, such approximation bring some course imprecision to the diagram it is still valid and adequate for our study.

Table 3.5: Sintering transport mechanisms [19].

Mechanisms	Transport path	Source of matter	Sink of matter
1	Surface diffusion	Surface	Neck
2	Lattice diffusion	Surface	Neck
3	Vapor transport	Surface	Neck
4	Boundary diffusion	Grain boundary	Neck
5	Lattice diffusion	Grain boundary	Neck
6	Lattice diffusion	Dislocations	Neck

The sintering stages are now going to be presented containing a description of the process indicating the contribution of each involved transport mechanisms.

1. Adhesion-Stage 0

At this stage the powder particles, which were brought together by pressing, adhere to each other by interatomic forces (see figure 3.17(a)). The also described as the adhesion stage occurs spontaneously with the formation of a starting sinter bond [17]. In case of crystalline solid the grain boundary energy depends on the crystal orientation across a grain boundary, so, if possible, the particles will rotate and repack to obtain a higher packing density and lower energy grain boundary structure [17].

In order to obtain the rate-equation for this stage Ashby [19] assumed that when particles are put in contact, interatomic forces draw them together at approximately the sound velocity, v, until equilibrium is achieved at the neck size, leading to:

$$(\dot{x})_0 = \frac{cp_r^2}{x} \quad for \quad x < \left(\frac{\gamma p_r^2}{10s}\right)^{1/3} \tag{3.27}$$

$$(\dot{x})_0 = 0 \quad for \quad x \geq \left(\frac{\gamma p_r^2}{10s}\right)^{1/3} \tag{3.28}$$

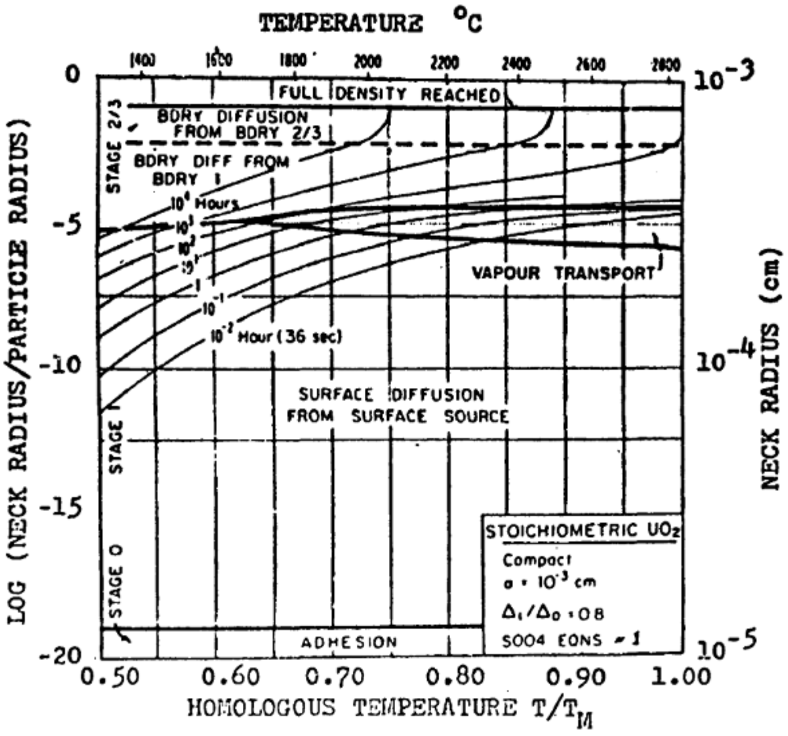

Figure 3.18: Sintering diagram for an aggregate of UO_2 particles of radius $10\,\mu m$. Vapor transport appears here as the dominant transport mechanism [19].

2. Neck Growth-Stage 1

The principal characteristic of this stage (transition between (*a*) and (*b*) in figure 3.17 and also in figure 3.19), which starts happening at approximately $0.25\,T_M$, is the interparticle neck growth [19]. The chemical potential of atoms at the neck where two particles meet is determined by the principal curvatures there. This potential determines the matter flux towards this particular region, coming from all other parts of the system where with a higher potential [19]. The neck growth-rate is then determined by the total of matter reaching the neck, which in other words means the contribution to the process from all transport path mechanism.

In Rahaman [33] it is stated that this interparticle contact will produce a neck size of $0.4-0.5$ of the particle radius (p_r), whereas the compact density would increase from $0.5-0.6$ of the theoretical density (TD) to 0.65 of TD.

During this first stage of sintering no grain growth takes place since the solid-vapor surfaces diverge at an acute angle from the particle-particle contact area. Any grain boundary movement away from the minimum area position would require it to increase significantly in area and energy, so that is why the boundary is initially confined to the neck area [18]. After the equilibrium condition between solid-vapor surface and particle-particle contact area has reached by neck growth, the inhibition to boundary motion decreases allowing the grain growth to happen [18], which is also the point that determines the end of the first sintering stage.

All transport mechanisms are involved in this stage and according to figure 3.18 the surface diffusion gives the biggest contribution.

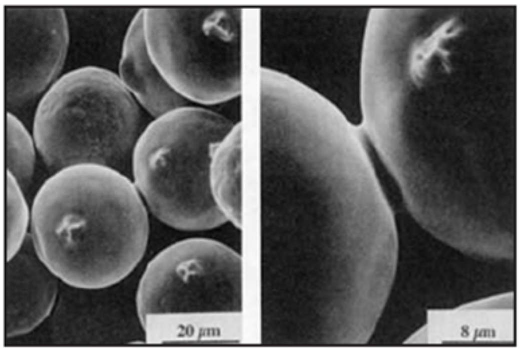

Figure 3.19: Scanning electron micrographs of the neck formation during sintering. The spheres (33 μm diameter) were sintered at 1030°C for 30 minutes in a vacuum [20].

3. Intermediate Stage-Stage 2

The end of the previous stage is the starting point of this one, i.e. where a recently reached equilibrium condition between the solid-vapor surface (pore) at the locus of intersections with the solid-solid surfaces (grain boundary) with independently curved surfaces between intersections propitiates the grain growth [18].

In the intermediate stage a representative characteristic is the still continuous porosity phase and that the pores are all intersected by grain boundaries [18, 33] as can be seen in figure 3.20. Pores may become unstable and pinch off, leaving behind isolated pores indicating that this stage is finishing. Furthermore, densification is assumed to happen by simply porosity shrinkage, which reduce their cross-section [33].

The second stage covers the major part of the sintering process taking the compact to reach a TD of up to $\sim$ 92%. The most important transport mechanisms present at this stage are the boundary diffusion and the lattice diffusion both having the same source of matter, the grain boundary [19].

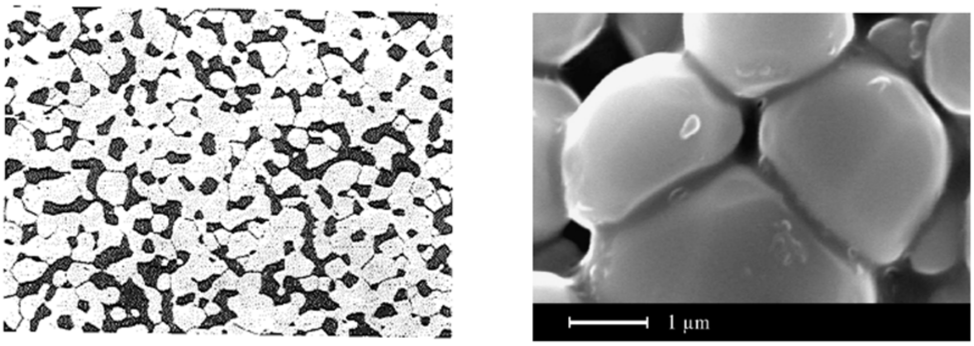

(a) (b)

Figure 3.20: Intermediate stages of sintering. In (a) typical intermediate structure for alumina gel sintered for $12\,h$ by $1750\,°C$ [18]. (b) SEM investigation of $Nd:YAG$ doped with $0.3\,wt\%$ SiO_2, sintered under vacuum at $1800\,K$ for 15 minutes [21].

4. Final Stage-Stage 3

The so-called final stage of sintering will start with a TD of $\sim 92\,\%$ and an eventually pinched off porosity. The pores now located at four-grain corners or inside the grains (see figure 3.17 and 3.21) are now closed and may continuously shrink and disappear indicating the completion of the sintering process [18].

Grain growth is also taking place at this stage as well as densification, which may reach up to the TD. At the end of the process there should be a uniform grain size distribution. Another possible end to the stage 3 happens when discontinuous or exaggerated grain growth occurs before all the porosity is removed [18].

Similarly to the second stage of sintering, the most important transport mechanisms are again the boundary diffusion and the lattice diffusion both having the same source of matter, the grain boundary [19].

3.2.5.2 Experimental Sintering Process

During the pre-test phase several experiments were conducted in order to find the optimum sintering set up. This point was investigated for three different sintering dwell times of 3.9 and 27 hours at the isothermal level by $1770\,°C$ and for the same sintering atmosphere of 100% dry H_2. The temperature was raised up at a rate of $5\,°C/min$ until it reaches $1000\,°C$ hold at this temperature for 30 minutes in order to assure a complete elimination of all additives before starting the second stage of sintering. The temperature continues rising now at a rate of

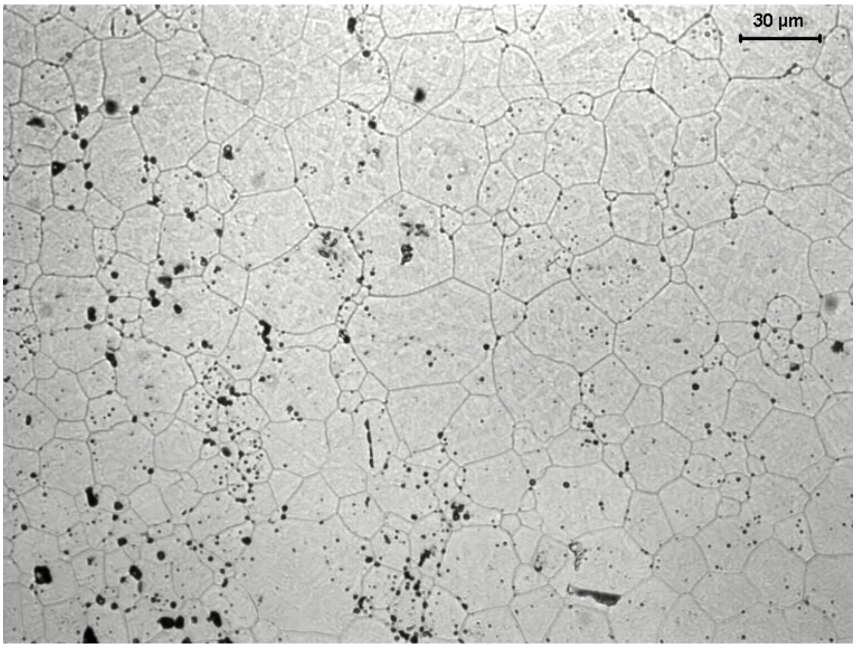

Figure 3.21: Micrograph of UO_2 at $200\,X$ sintered for $3\,h$ by $1770\,°C$ having a final density of more than 98% TD.

$10\,°C/min$ until the desired sintering temperature of $1770\,°C$ is achieved. After dwell on $1770\,°C$, the isothermal, for either 3.9 or 27 hours the samples were controlled cooled down to $20\,°C$ at a rate of $5.8\,°C/min$. This sintering process can be seen in a simplified way at the scheme of figure 3.22.

The sintering furnace, from company FCT, consists of a water cooled cylinder made of steel (see figure 3.23) and the working temperature can reach up to $1800\,°C$. The inside atmosphere is evacuated (max. $1x10^{-1}mbar$) and can be used with reducing gas mixtures or with inert gas (Argon) and also with oxidizing atmospheres. There are two pistons, made of aluminum-oxide (Al_2O_3) where the lower one is hydraulic controlled and can be moved from the bottom of the oven till the top making possible the positioning of the green pellets on it and the superior one, which is used to close the oven. These pistons are made of Al_2O_3 in order to give a better thermal isolation at the heating zone. At the middle part of the oven, in a pressurized chamber and separated from the sintering testing chamber we have the heating-element made of molybdenum (Mo). This heating-element is surrounded by Al_2O_3 wool for reducing heat loss and concentrating most of the heat to the samples. The heating zone is separated from the sample area since it needs to be constantly under a reducing atmosphere while in the sample area different types of atmosphere can be used. For regulating the furnace's the temperature is measured at two different points, at the pellets position and at heating-element chamber. The thermocouple used here is made of tungsten-rhenium ($W - 3\,\%\,Re/W - 25\,\%\,Re$). After the samples are placed in the furnace and the superior piston is positioned, the furnace is evacuated, and the process parameters such as gas mixture and sintering temperature and time are adjusted the experiment can finally start.

In figure 3.24 it can be seen how the green pellets are positioned in the sintering furnace as well as the sintered pellets. Differently from the sintering furnace in the industry (see figure 3.16), where the pellets lie one upon the other, the pellets stand upright each other being each layer separated by tungsten plates.

The sintered samples characteristics e.g. length, diameter and density were measured and also can be seen in table 3.6 and 3.7. The density can be directly measured according to the Archimedes' Principle also called immersion method [95], which is more precise, or indirectly measured by determination of the porosity content at fuel microsections. For the second porosity determination method the model developed by Saltykov [96] was used. The accuracy of this method depends a lot on the quality of the electronic microscope used as well as on the camera for shooting the microsection pictures. Also the experience of the microscope operator contributes to the uncertainty of this model. That is why the determination of the porosity volume at this work was done according the Archimedes' Principle. The Saltykov's model was just used for the depiction of the porosity distribution in the pellet, which is presented in the subsection 5.1 in chapter 5.

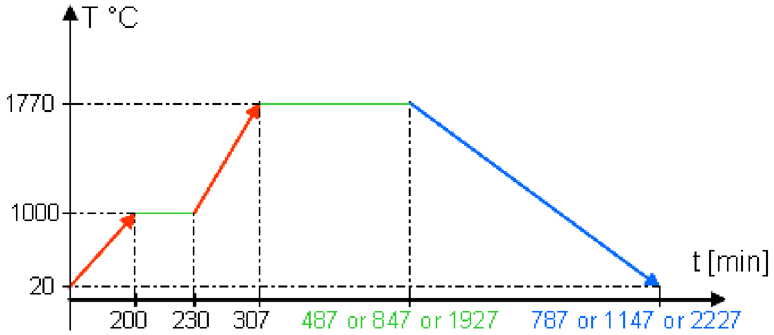

Figure 3.22: Sintering process.

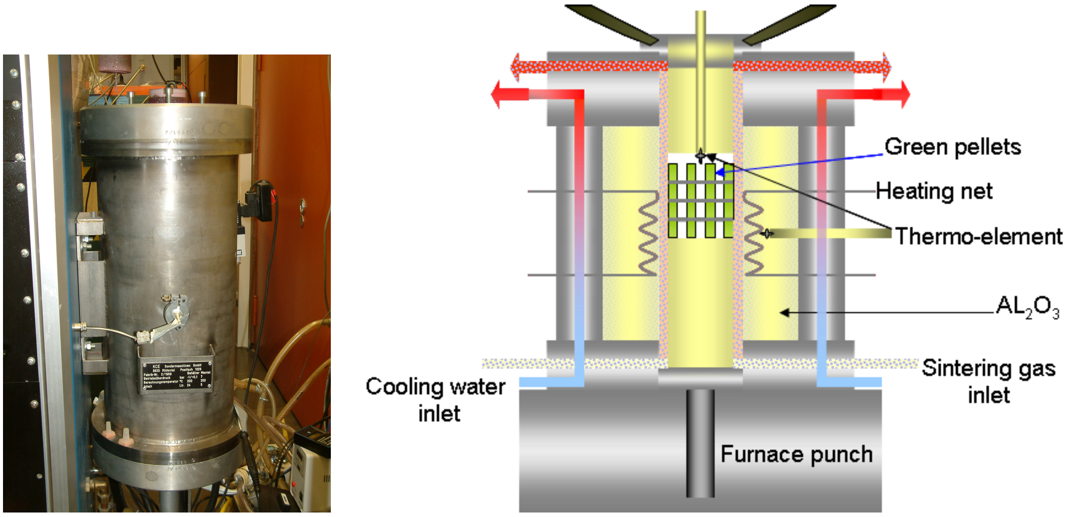

(a) (b)

Figure 3.23: FCT sintering furnace (*a*) and a schematic design showing its internal arrangements (*b*).

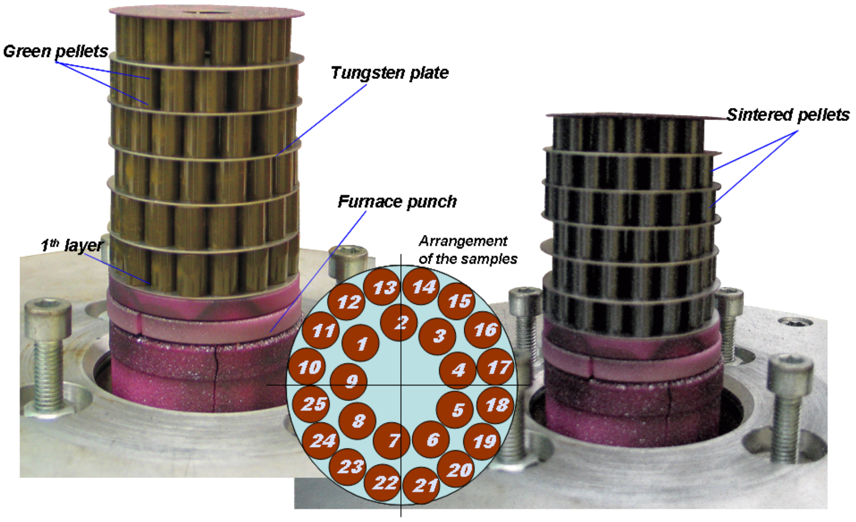

Figure 3.24: Green and sintered pellets arrangement in the sintering furnace.

3.2.6 Grinding

In section 3.1 it was explained that because of the green pellet density variation the resulting sintered pellet will present a deformation from its original cylindrical shape to an hourglass-like shape having a thinner diameter at its center portion along the axial direction [97]. For this reason the common process used to remove material from the pellets to achieve the required cylindrical geometry and diameter tolerances is the grinding process, especially the centerless grinding process.

The laboratory scale dry centerless grinder consists of a machine with an grinding wheel, which rubs against the ceramic pellet removing tiny pieces of material and a regulating wheel for pushing the pellet against the grinding wheel at a certain angle.

Except for the $Gp1$ pellets, which were not sintered, all produced pellets were ground. They were ground to maximal $0.1\,mm$ in diameter per pass for avoiding excessive stresses to the sample, which could lead to the development of flaws or even the collapse and failure of the sample.

3.3 UO_2 powder Characterization

For a reliable, cost effective, and defect free UO_2 fuel pellet a good quality UO_2 powder should be used as raw material for the pelletizing. Therefore, the powder characteristics are determined right after the reconversion from UF_6 to UO_2 powder. A high presence of fluorine originated from a not complete conversion can lead to undesirable effects during sintering when UO_2 fuel is reduced by hydrogen. A fluorine content inferior to $100\,ppm$ is desired and any other impurities should not exceed the level of several ppm, especially for those elements having a high neutron absorption cross-section [12].

Some other relevant characteristics are determined such as:

- Particle size distribution
- Particle morphology on the structure
- Particle strength
- Crystallite size
- Stoichiometry

- Density (bulk and tap densities)
- Specific surface area
- Sinterability
- Flowability

3.3.1 Particle size distribution

Because of its great influence on the macrostructure the microstructure of the powder was analyzed. Furthermore, it was already published elsewhere by Djuric [98] and Ranogajec [99] that powder particle size greatly influence the sintering and pressing process. Djuric [98] as well as Ranogajec [99] demonstrated that by pressing small particles they would behave more plastically and the bigger ones would act more in a brittle way. In fact, an increase in the particle's dimension would result in a decrease of the stress for the brittle fracture, which is directly linked to the green density. So, according to Djuric [98] and Ranogajec [99], larger particles implies in higher green densities, lower porosity and higher compressive strengths. Ranogajec [99] also reported that depending on the particle size the densification rate could be increased or decreased.

Among the several method used in the literature for measuring the particle size distribution [100, 101, 102, 103, 104, 22] the laser diffractometry analysis has become a frequent choice, mostly because of its quick, easier and accurate results. The method can be implemented in a wet or dry dispersion medium. The wet dispersion is a quite successful method, but for materials that are manufactured or used as dry powders it is often necessary to carry out particle size analysis using the dry dispersion method [22].

The first commercial laser diffractometers were developed by CILAS in France, using a liquid dispersant, Malvern Instruments in United Kingdom and Leeds and Northrup (Microtrac) in the USA [100].

For the measurements a dry dispersion equipment *Mastersize 2000* with the Scirocco sample dispersion unit from Malvern Instruments was used. The sample size was of approximately $1.5\,g$. The median diameter (see figure 3.25a), D_{50}, which is the value of the particle size that divides the population into two equal halves is usually the value adopted for comparison analysis. In our case its value of $120\,\mu m$ indicates that the particle are larger than those at sieved and milled state for UO_2 $58\,\mu m$ and $1\,\mu m$ respectively. Figure 3.25b also presents a SEM picture of the used UO_2 powder.

Table 3.6: Gp2 Sintered samples.

Type	Samples	Sint. Isotherm. [min]	Mass/unit [g]	Density [g/cm^3]	TD[1] [%]	Length [mm]	Diameter [mm]
A	33	180	5.95±0.02	10.64±0.02	97.04±0.19	10.81±0.06	8.08±0.01
B	34	540	6.00±0.05	10.68±0.01	97.44±0.10	10.97±0.11	8.03±0.01
C	33	1620	5.97±0.04	10.74±0.01	97.97±0.05	10.94±0.11	8.02±0.01
D	33	180	6.02±0.04	10.45±0.01	95.31±0.09	11.09±0.09	8.13±0.01
E	33	180	5.94±0.03	10.46±0.01	95.45±0.06	10.78±0.10	8.14±0.01
F	33	180	6.02±0.03	10.51±0.01	95.85±0.07	10.93±0.08	8.14±0.01
G	33	180	5.95±0.04	10.46±0.01	95.44±0.12	10.94±0.12	8.11±0.01
H	33	180	4.04±0.02	10.70±0.01	97.66±0.06	7.26±0.05	8.08±0.01
K	32	180	8.05±0.05	10.70±0.01	97.65±0.06	14.48±0.11	8.09±0.01
L	33	180	5.87±0.04	10.43±0.01	95.12±0.09	10.84±0.09	8.11±0.01
SQ-Std.	14	180	5.74±0.16	10.64±0.01	97.04±0.09	10.72±0.10	8.10±0.01
SQ-Keratin.	14	180	5.82±0.04	10.50±0.01	95.78±0.12	10.94±0.08	8.09±0.01

[1] Theoretical density to UO_2(10.96 g/cm^3)

Table 3.7: Gp3 Sintered samples.

Type	Samples	Sint. Isotherm. [min]	Mass/unit [g]	Density [g/cm^3]	TD[1] [%]	Length [mm]	Diameter [mm]
M	36	180	8.86±0.08	10.78±0.01	98.32±0.03	15.47±0.19	8.10±0.01
N	37	540	8.19±0.09	10.72±0.02	97.78±0.19	14.74±0.23	8.08±0.01
P	37	540	8.73±0.05	10.80±0.01	98.55±0.04	15.26±0.06	8.13±0.01
Q	39	180	8.08±0.08	10.47±0.04	95.55±0.41	14.86±0.12	8.09±0.01
R	38	180	8.54±0.06	10.54±0.01	96.21±0.11	15.12±0.12	8.17±0.01
S	39	180	8.63±0.08	10.54±0.03	96.14±0.31	15.25±0.15	8.18±0.01
T	36	180	8.68±0.03	10.57±0.01	96.40±0.12	15.54±0.09	8.16±0.01
U	36	180	8.18±0.05	10.55±0.01	96.29±0.12	14.82±0.16	8.11±0.01
V	36	180	8.72±0.06	10.63±0.01	96.97±0.10	15.28±0.16	8.17±0.01
X	36	180	8.70±0.07	10.59±0.01	96.60±0.09	15.33±0.15	8.18±0.01

[1] Theoretical density to UO_2(10.96 g/cm^3)

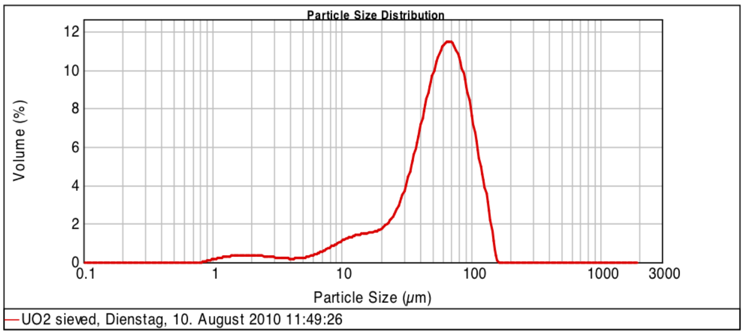

(a) Particle size distribution graphic.

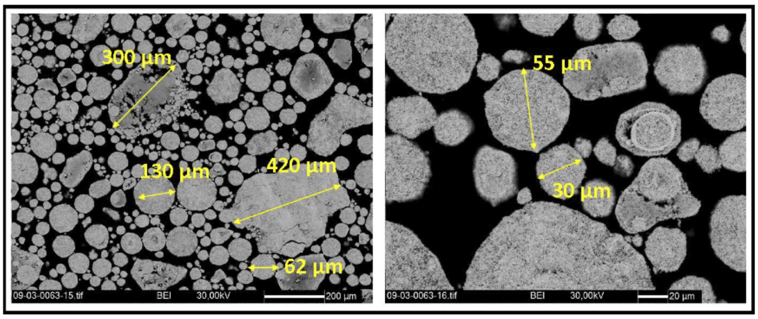

(b) SEM microsection the particle size population.

Figure 3.25: UO_2 particle size distribution [22].

3.3.2 Stoichiometry

3.3.2.1 Fluorite Crystal Structure

The fluorite, CaF_2, also called fluorspar is a mineral composed of calcium fluoride. The crystallographical description of the fluorite is the space group $Fm\bar{3}m$ where F is the fluorite cubic lattice and the numbers describe the symmetric operations.

Some applicability possibilities of this oxide structure are in the chemical industry in form of fluoride for the production of hydrofluoric acid used as source of fluorine-containing fine chemicals [105] and in the optical field for the semiconductor lithography using deep-UV lasers based on fluoride and also for the production of especial glasses.

UO_2 has a face-centered cubic crystal structure commonly classified to the fluorite structure.

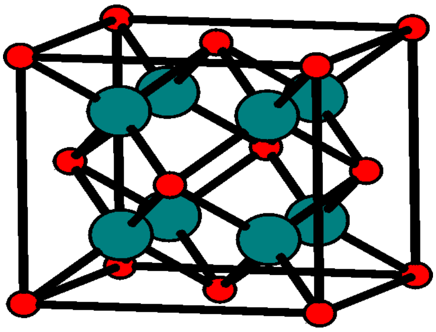

Figure 3.26: Fluorite crystal structure. Fluoride anions (green) and calcium cations (red) [23].

For this reason is the fluorite structure here mentioned since the uranium dioxide molecules have their same atomic arrangement. Thus, in the fluorite the calcium atoms occupy the eight tetrahedral sites and their face centers while the fluorine atoms place themselves inside forming the face-centered cubic packing structure (see figure 3.26) providing plenty unoccupied positions in the cubic fluorine array in the middle of the cell. In a similar way the uranium atoms are positioned at the tetrahedral sites and their face centers and the oxygen atoms form a cubic array in the middle of the cell allowing the existence of interstitial spaces, which are of great importance in the case of the UO_2 molecule since in this free space fission products can be accommodated without causing any staining on the lattice positions [31].

3.3.2.2 O/U Ratio

The chemical composition of UO_2 pellets influences its neutron absorption cross-section, which is an important nuclear parameter in sustaining the nuclear chain reaction in the reactor core. Thus, the oxygen chemical potential has a dependency on the fuel composition and changes with temperature and irradiation [12].

It is desired that the DC powder before sintering has a slightly higher than 2.00 O/U ratio since in this configuration the powder is more stable on air avoiding an uncontrolled oxidation.

The stoichiometric characteristics of UO_2 sintered pellets are established in the sintering furnace where the temperature, the isothermal dwell and the atmosphere in the furnace determine the O/U ratio. The sintering atmosphere is a volume diffusion controlled process. At any atmosphere configuration it is a strongly reducing environment allowing that the sintered fuel have a very high degree of stoichiometry. The hyper-stoichiometry of the fuel itself is a positive characteristic since it increases the cladding inner oxidation, but, on the other hand this “extra” oxide layer becomes a thermal barrier, which together with the intrinsic low thermal conductivity of UO_2 act in a negative way in the reactor core elevating the fuel’s central temperature, which finally leads to a higher release of highly corrosive gaseous fission products [106]. A hyper-stoichiometric fuel also reduces the availability of cesium, which is a natural iodine catcher elevating the probability of stress corrosion cracking (SCC) and consequently also the predisposition for pellet cladding interaction (PCI) failures [12]. In the case of a hypo-stoichiometry UO_2 fuel we also have a tendency to increase the SCC weakness since it decreases the cladding inner protecting film and the fuel plasticity [12]. For this reason the O/U-ratio is of a great importance in the fuel production process.

In table 3.8 can be seen the stoichiometry value for the UO_2 powder as well as for the sintered pellets.

3.3.3 Density

A simple definition for density is that it represents how cohere the atoms of a substance are. Theoretically speaking it can easily be calculated by dividing the mass of a material by the volume occupied by it, mass per unit volume. Two of the most used direct methods are the determination by geometrical means by dividing the mass of an object by its calculated volume, and for a more precise measurement the buoyancy principle from Archimedes can be applied. Moreover, the density can also be indirectly determined for example by measuring the amount of porosity present in a microsection sample analyzed under the microscope. In this case the total porosity measured represents the amount, which reduces the theoretical density, in other words, having a sample for instance with a total porosity of 2 % means that the sample density is 98 % from the theoretical one. Both direct and indirect methods here described were used in the present work.

Commercial light water reactors (LWR) fuel density varies from 94 to 97 $\%TD$. Furthermore, the final sinter-density of the ceramic nuclear fuel is influenced by e.g. powder characteristics, pellet green density, sintering regime and also by the introduction of additives to the virgin UO_2. In fact, a compromise between what is the best technical fuel configuration and what is economically viable must be found. This because fuel pellets with a higher density can imply in a more compact core, an increase in the thermal conductivity of the pellet and also an extension of the time between refueling, enabling a higher fuel burnup. On the other hand in fuels with densities above 97 $\%TD$ it can be expected that during the reactor operation an earlier and

Table 3.8: O/U ratio.

Sample type	Uranium (U)	Oxygen (O)
UO_2 powder	1	2.09
UO_2 pellet	1	2.00

stronger fuel swelling interacts with the cladding thanks to the radial temperature gradient, which in this kind of fuel prompts higher internal stresses since the pellet centre tends to expand more than the periphery and also more than then the zircaloy cladding because of their different thermal expansion coefficients [2]. In addition to that the porosity also acts retaining the corrosive fission gases and doing so delays its attack to the zircaloy cladding. Finally, it can be stated that the main contribution of the fine porosity is a controlled thermal re-sintering so the density increases during the first and second reactor operation cycle, which is a counter measure for the matrix swelling at the beginning of the cycle.

As already said the final fuel pellet density depends on many factors e.g. additives and their quantities added to the virgin UO_2 powder, green density and the sintering process. However, the most important influencing factor is the initial characteristic of the powder [17, 12]. In can be seen in table 3.11 that each additive type has its intrinsic density. Uranium dioxide has a density of $10.96\,g/cm^3$ [107], which by mixing it with additives with a lower density will undoubtedly reduce the final density of the nuclear fuel what at certain limits is a desired effect (see section 3.4 to find the density of the additives mixed to the UO_2 powder).

3.3.4 Specific surface area

During the sintering process there is a natural loss of the initial powder surface area because of the compact shrinkage and the growth of the interparticle bonds [17].

The specific surface area measurement is used to determine the cohesive forces among the particles in a green pellet influencing also the sintering rate and mechanism. Zemek [12] states that a high specific surface area produces green bodies with higher green strength, nevertheless this fact depends on the powder morphology and it is quite complicated to generalize and to state a requirement threshold value.

For its determination the BET method developed by S. Brunauer, P.H. Emmett and E. Teller [108] in 1938 was used. The theory relies on physical absorption of gas molecules onto the solid surface analyzed. Then the mass of the absorbed gas is measured as a function of the pressure at a fixed temperature (usually liquid nitrogen) [8]. In other words the BET method measures the amount of gas needed to saturate the measured powder surface [17].

Before the determination of the surface area the powder density was determined at a pycnometer, and the obtained result of $10.9477 \pm 0.0817\,g/cm^3$ can be considered in agreement to the literature [107].

The ISO 9277:1995 [109] standard was used as reference to the measurement carried out at NOVA 2000e analysis equipment (see table 3.9). The powder sample was dried prior the measurement for approximately 2 hours at about $60\,^{\circ}C$ in nitrogen.

Table 3.9: UO_2 powder and granulate specific surface area and density.

Type	Pour Density [g/cm^3]	Tap Density [g/cm^3]	Spec. Surface Area [m^2/g]
UO_2 Powder	1.65	1.81	2.18
UO_2 Granulate	2.66	2.99	-

Table 3.10: Sinterability samples.

Type	Gr. Density [g/cm^3]	Sint. Isotherm. [min]	Sint. Density [g/cm^3]	TD [%]
A	5.86	487	10.66	97.23
B	5.85	847	10.72	97.83
C	5.84	1927	10.73	97.93
M	6.21	487	10.72	97.75
P	6.20	847	10.75	98.10

3.3.5 Sinterability

The change in density of the sintered body as a function of the green compact density represents the sinterability of a powder [110]. Hence, the powder's sinterability can be influenced by many variables from the production process e.g. green density, powder particle size characteristics, crystal structure, presence of additives, sintering procedures, etc.

The importance of the sinterability relies on the necessity of the fuel fabricators to have an idea of the highest sinter-density achievable by a specific powder type at certain production conditions. With this information the necessary adjustments of the process for achieving the desired client's sinter-pellet density, which can vary from 94 % to 97 %, can be done by the addition of additives.

In the laboratory powder's sinterability determination was carried out in a dilatometer (see section 3.3.5.1). Five samples representing the different green densities and sintering time used were prepared following the same production process described in section 3.2 and the results can be seen in table 3.10. The sintering temperature of $1760\,°C$ was the same for all samples.

Ideally these green pellets should had been prepared without the addition of any additive but because the high friction forces present during the pellet pressing the addition of a powder lubricant is necessary. For this reason $0.24\,wt\,\%$ of ADS was added to the granulate leading to a significantly reduction of the friction forces. Furthermore, this amount of lubricant reduces the sinter-density in about 0.7 % resulting in a lower sinter-density than the expected value. But since all the pellets are going to have the same amount of lubricant it won't influence the future comparisons.

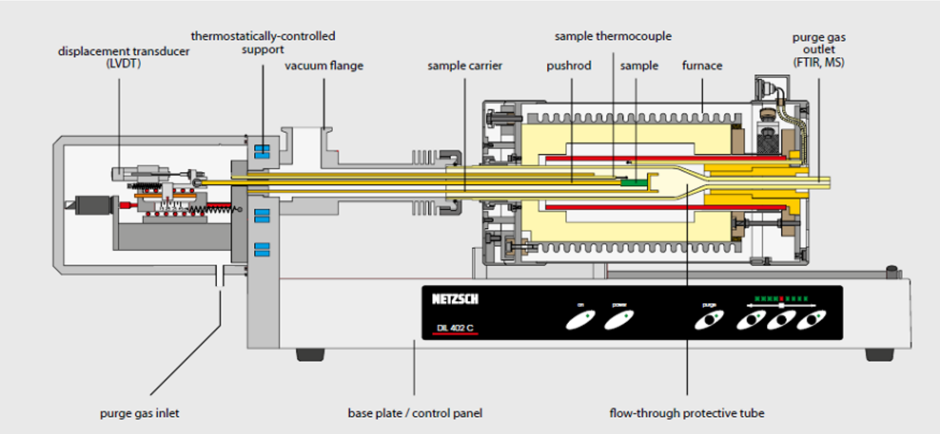

Figure 3.27: Schematic of Netzsch 402C appliance.

3.3.5.1 Dilatometry

In a dilatometry experiment a dilatometer measures the expansion or shrinkage of a material while it is heated or cooled. Thus, by its use, the shrinkage rate sintering mechanisms and activation energy can be determined.

The dilatometry analysis using a horizontal pushrod dilatometer consists of placing a sample, in our case, a cylindrical pellet in a Al_2O_3 tube inside a moveable furnace. The furnace temperature is controlled by a W/Re thermocouple located next to the sample. The pushrod placed in contact with the sample transmits length variation while the sample is subject to a change in temperature to a linear variable displacement transducer ($LVDT$), which produces an output signal proportional to the displacement [111].

For the experiment a horizontal pushrod dilatometer model Netzsch 402C was used and a similar model can be seen in figure 3.27. The principle consist in measuring the shrinkage or expansion of material while it is subjected to temperature variation over the time. The linear thermal expansion or shrinkage,$\Delta l/l_0$, can be determined by the following equation 3.29:

$$\Delta l/l_0 = \frac{1}{l_0}\left(\frac{l_1 - l_0}{T_1 - T_0}\right) \tag{3.29}$$

where l_0 and l_1 are the lengths of the samples at the temperatures T_0 and T_1 respectively.

The objective for using the dilatometer before producing all the testing samples is here justified because of the magnitude of the work would require a great amount of resources, basically UO_2 powder. So, in order to reduce the bulk of powder needed for the pre-tests and the initial necessity of following closely the pellets' sintering behavior a small number of pellets having different lengths and containing the different types of additives were produced and sintered. Hence, it was desired for the work that a varied shape and size of pores and grains, different pores and grains distribution, different pellet lengths as well as distinct final densities were present in the analyzed pellets.

The resulting curve for the sintering process obtained from the dilatometer experiment is known as the master sintering curve (MSC), see figure 3.28, which was first proposed by Su and Johnson [112]. They proposed that the geometric parameters related to sintering are often functions only of density for a given powder and green-body process, provided that one diffusion mechanism dominates in the sintering process [113]. This curves have since then been used to characterize the sintering behavior of powders and green-bodies regardless the heating profiles. With the MSC it is possible to estimate the densification behavior of a specific sample reducing the number of practical process set up experiments. Finally, the MSC is a characteristic measure of the sinterability of a compact over a wide density range.

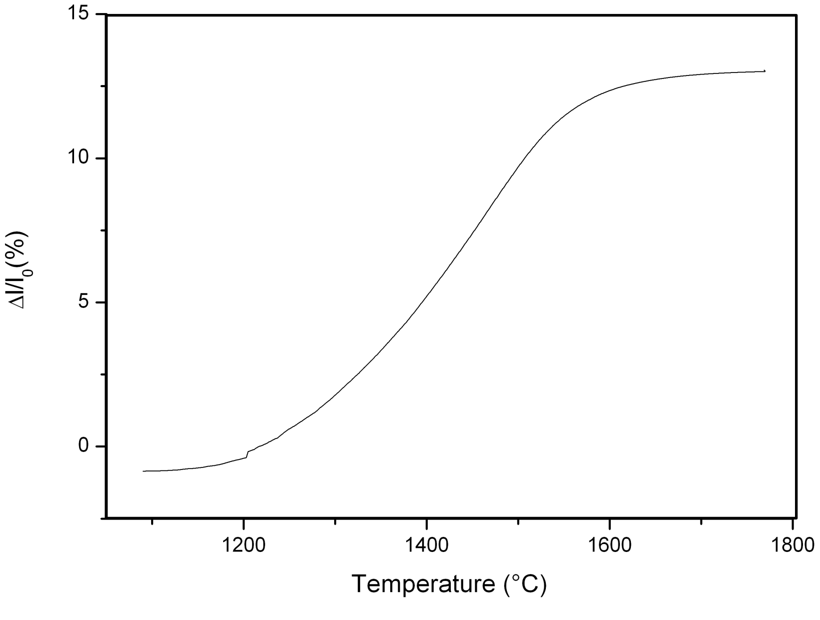

Figure 3.28: Master sintering curve for UO_2 pellet sintered under H_2 by 1770 °C.

In order to determine the curve two parameters should be taken into consideration, first $\phi_{(\rho)}$, which is term dependent on the sample density,ρ, evolution and the second one is $\Theta(t, T(t))$, which is a function of the time, t, and of the temperature, T. The relationship between $\phi_{(\rho)}$ and $\Theta(t, T(t))$ is then defined as the MSC (see equation 3.30), where Q is the activation energy and $\bar{R}$ is the gas constant.

$$\phi_{(\rho)} = \Theta(t, T(t)) \equiv \int_0^t \frac{1}{T} exp\left(-\frac{Q}{\bar{R}T}\right) dT \qquad (3.30)$$

The time dependent relative density, presented in figure 3.29, can be analyzed in terms of the linear shrinkage of a sample in the next equation 3.31 [114]:

$$\rho_r = \frac{\rho_g}{\left(1 - \frac{\Delta l}{l_0}\right)^3} \frac{1}{\rho_0} \qquad (3.31)$$

where ρ_g is the green density of the sample and ρ_0 is the theoretical density of the sintered sample.

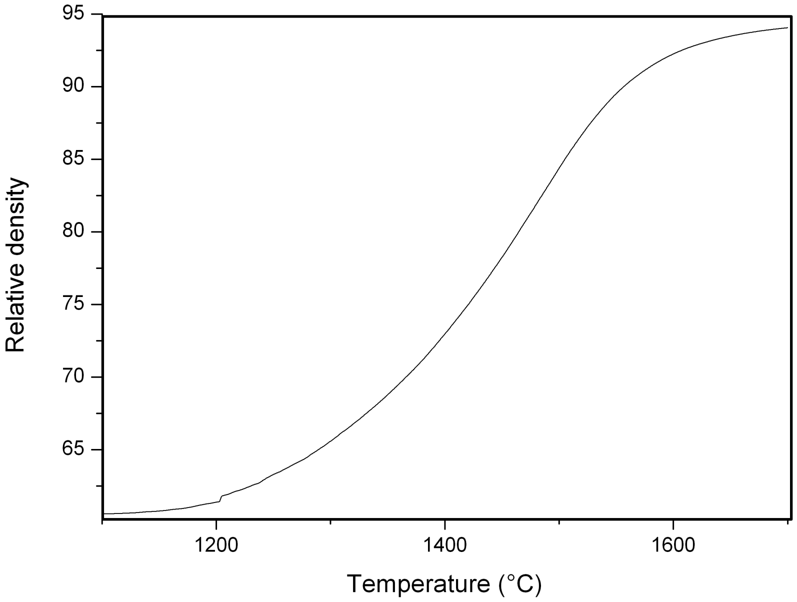

Figure 3.29: UO_2 relative density development by sintering process under H_2 by 1770 $°C$.

The sintering processes optimized in the dilatometer were reproduced for the tested pellets and are described in section 3.2.5.

3.4 Additive Characterization

The necessary porosity for the ceramic fuels is controlled by the usage of additives. These can be characterized in three groups: oxidized urania (U_3O_8), pore-formers and lubricants, which is not used as pore-former for the fuel but rather for reducing the friction stresses during the pressing of the green pellets. So besides the addition of the “real” pore-formers it must be also included in the calculations the small amount of lubricant applied to the granulate.

3.4.1 Oxidized Urania

For the comparison analysis two types of oxidized urania were used, the oxidized UO_2 powder (OP) produced by the oxidation of the DC UO_2 powder in air at about $500\,°C$ in a small oven and the oxidized sintered UO_2 pellet scrap (OS) prepared in the same way as the OP.

In the industry the usage of the OS is justified because the scrap, intrinsic to the production process, can be reintroduced to the process reducing the scrap inventory. As for the OP it is used for improving the quality of the green pellets providing higher interparticle forces [12].

3.4.2 Azodicarbonamid

The organic pore-former agent AZB (azodicarbonamid - $NH_2 - CO - N = N - CO - NH_2$) can be added to the UO_2 powder either at the beginning of the powder preparation process during the powder blending or in a more conservative way after the granulation. The more conservative way is applied for some fuel fabricators because the pore-former is an organic material and so it can act as neutron moderator, which from the criticality safety side need to be considered. For this reason both possibilities were analyzed.

AZB has a melting point of $225\,°C$. During the sintering process it is gasified and contained in pores, which reaches an equilibrium state between the pressure of the gas inside the pores and the surface tension forces trying to eliminate all the porosity.

3.4.3 Aluminum Distearate

The organic agent ADS (aluminum distearate - $C_{36}H_{71}AlO_5$) is an aluminum salt of stearic acid, which is used as a solid lubricant added to the granulate prior to the pelletizing reducing the friction forces among the granulate, the die and the pressing punches. Its melting point is $175\,°C$

decomposing during sintering in a similar way as the AZB. Moreover, the residual Al_2O_3 speed up the grain growth rate, at heigh temperatures, during the sintering [12].

3.4.4 Keratin

The usage of ceramics containing fibers in their composition for improving their mechanical properties is quite new when compared to other structural materials such as steels, aluminum, titanium alloys or even monolithic ceramics [54]. The high strength fibers used for this purpose must withstand the high temperature sintering process so they can be used in innumerous technical fields for instance by the aerospace or automobile industry. SiC-based fiber family and alumina and alumina-based fibers are the most used types of fibers used. Both SiC-based and alumina-based fibers present excellent oxidation resistance, good mechanical behavior at room temperatures. However the later type have a poor creep behavior even at moderate temperatures. For this reason the SiC-based fibers are the most commonly used reinforcements in ceramic matrix composites especially at high temperatures.

Some drawbacks of the SiC-based fibers are: the fact that they are fragile needing to be embedded in a refractory ceramic matrix and the elevated prices. There are also the SiC nanofibers, which are not extensively used in ceramic composites much because its handling difficulty, health considerations and cost [54].

Keratin, the last additive type here described, is not a conventional or commercial material added to the nuclear fuel. It was introduced to the UO_2 powder for basically two objectives, first to be used as a reinforcement fiber to the green pellet matrix enabling a possible improvement in its mechanical resistance during handling and second to be used as an organic, easy obtainable and environmentally friendly pore-former producing typical linear pores.

Differently from the SiC-based fibers the keratin fibers do not withstand to high temperatures and so are eliminated during the green pellet sintering process.

The main component of the hair fiber is keratin, a fibrous protein formed from long chains of amino acids such as cysteine, serine, glycine, proline, etc. In fact in hair fiber protein comprises up to 95 % of the hair fiber weight.

In order to determine the organic origin of the used fibers (see figure 3.30)spectrometry analyses were carried out in the laboratories of the UPV. The analysis consisted in comparing the characteristic spectrum of our fiber with standards of polyurethane, a synthetic fiber, silk and fresh human hair fiber, both organic materials. In figure 3.31 it can be seen the comparison between polyurethane and our fiber, showing clearly that both spectra do not coincide. When our fiber spectrum is then compared to the silk one it can be observed, in figure 3.32, some coincidence in both of them. Finally, when compared to the human hair fiber spectrum in figure 3.33 it can be concluded that fibers used in our experiments are really of organic origin.

Table 3.11: Additives characteristics

Additive	wt.%/Sample	Chemical Composition	Decomposition [°C]	Density [g/cm^3]
AZB	0.67	$C_2H_4N_4O_2$	225	1.681
ADS	0.24	$C_{36}H_{71}AlO_5$	230-500	1.033
OS	16.68	U_3O_8	-	8.529
OP	17.36	U_3O_8	-	8.616
Keratin	0.2 or 0.3	$(N-C-H-O-S)^1$	200-1500	1.272

$^1N(\sim 17\%) - C(\sim 50\%) - H(6\%) - O(\sim 21\%) - S(5\%)$

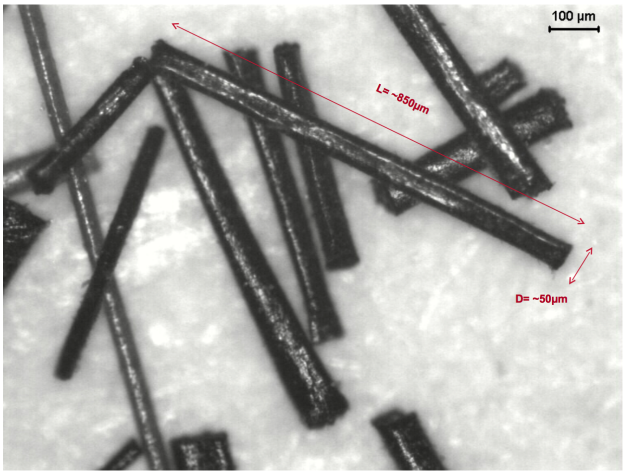

Figure 3.30: Used keratin fiber.

Thermogravimetric analysis, presented in figure 3.34, showed that more than 60 % of the keratin fibers had already disintegrated by 500 °C under H_2. By the end of the analysis at 1500 °C there was still 10 % of ash residual material, which did not evaporated indicating that this material most likely remain in the fuel when the sintering itself starts. The ash is most probably formed by carbon, hydrocarbons and by inorganic compounds present in the fibers. This behavior is somehow similar to what happen with ADS in the nuclear fuel. In figure 3.35 the thermogravimetric analysis of ADS is presented showing the existence of also 10 % of residual ash containing Al_2O_3.

The additives amount ($wt\%$) as well as their physical properties are detailed in table 3.11.

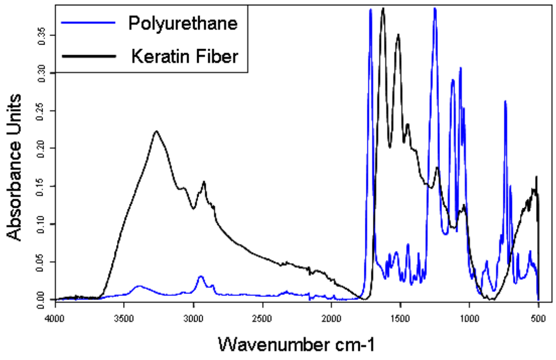

Figure 3.31: Spectrometry analysis between polyurethane and keratin fiber.

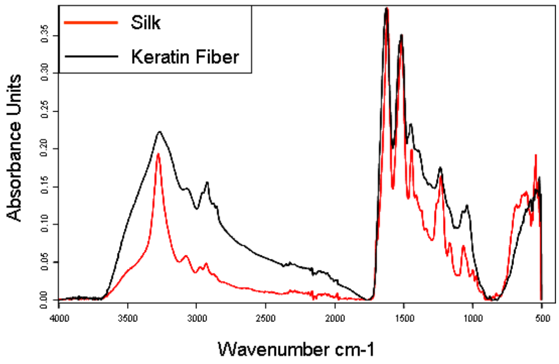

Figure 3.32: Spectrometry analysis between silk and keratin fiber.

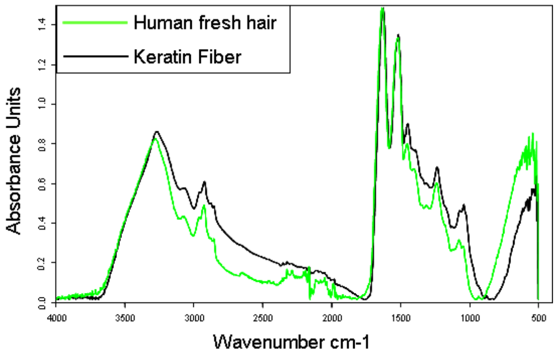

Figure 3.33: Spectrometry analysis between human fresh hair and keratin fiber.

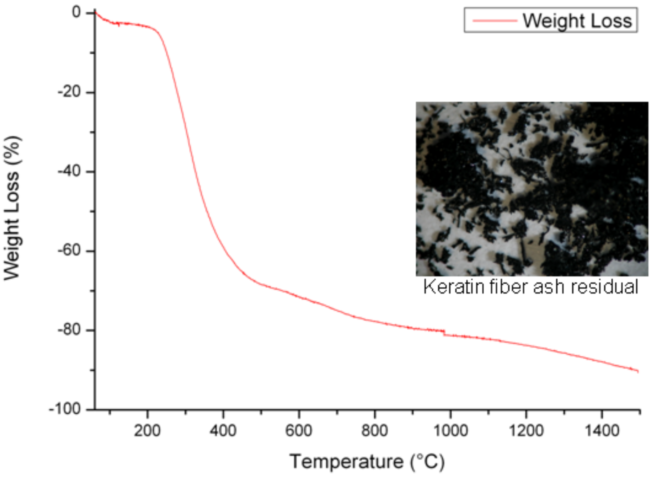

Figure 3.34: Keratin fibers thermogravimetric analysis.

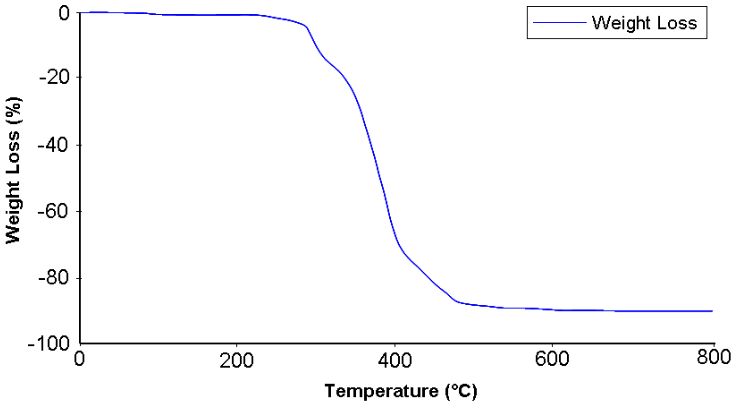

Figure 3.35: ADS thermogravimetric analysis.

Chapter 4

Experimental Procedures

In ceramics internal and superficial flaws and dislocations play a very important role on their mechanical strength. These defects are introduced during the production process and are intrinsic to any ceramic. In this concern it can be said that no ceramic material is free of defects.

Mechanical testing is necessary for understanding the material behavior under an applied stress. In other words, these experiments can show how reliable a certain ceramic type is when a defined load is applied to it. In fact it is desirable that before using a ceramic, for instance, in a load-bearing situation it should be extensively tested for the obtention of some characteristics:

- Weibull fracture strength
- Weibull modulus
- Stress rupture data
- Hardness
- Fracture toughness

Since a slight change in the microstructure leads to the variation of these parameters, they need to be acquired for each type of ceramic which was produced. In our case by changing the additive type, the sintering time or the pellet geometry we could see how expressively the mechanical strength and the reliability is influenced.

Unlike metals, which have comparable tensile and compressive strengths ceramics are much stronger in compression situations than in tension mainly because of its brittleness and low strain [8]. In tensile tests flaws are possibly introduced to the tested sample microstructure leading to an “early” failure. For this reason, unless extremely necessary, compression testing procedures are much more widely used for developing fragile materials.

The ceramic tensile strength is highly influenced by the applied loading rate to the tested sample. Tensile strength results, from a quasi-static loading rate, can not be compared to results coming from tests where a high loading rate regime is applied to the samples. While quasi-static testing procedures are well established and normalized e.g. ASTM C 773-88 (2006) [115], ASTM C 496-71 (1996) [116], where the first one determines the compressive strength of fired ceramics and the second one determines the tensile strength for cylindrical concrete specimens, the dynamic fracture theory is still not well understood. Even though several techniques and testing procedures for the determination of dynamic stresses have been proposed over the past decades by Shukla 2006 [117], Jiang and Vecchio 2009 [118] and most recently by Santana 2010 [119] we do not have any widely simple and reliable procedure, or even standard for its determination [120].

With nuclear ceramic fuel the situation is not much different from other ceramic types. Both dynamic and quasi-static stresses are present and influence on fuel integrity and for this reason both should be studied, but since the focus of our study is on developing the mechanical strength and the reliability of nuclear ceramic fuel and not on the developing of a specific type of testing the quasi-static testing procedure was the one chosen. We are not here trying to neglect the existence of dynamic stresses because it is well known from every fuel fabricator that unfortunately these stresses are constantly there at many processing steps before sintering e.g. filling the bowl feeder or after sintering such as emptying of the sintering boats, vibration at the bowl feeder and charging of the fuel rods, but stating that by the development of the mechanical strength by a quasi-static mean may also improve the resistance to a dynamic impact.

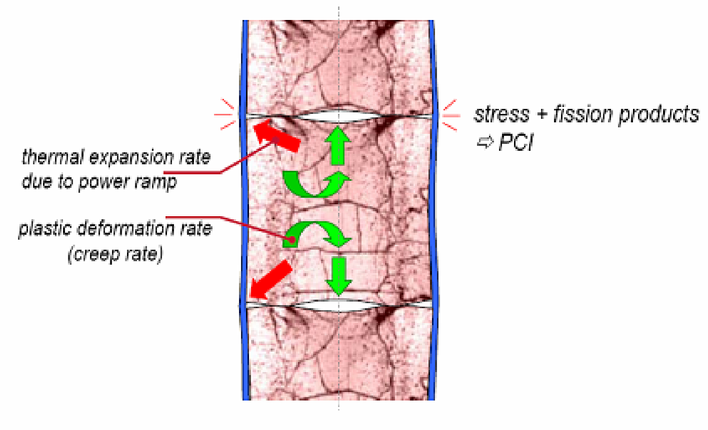

Figure 4.1: Pellet Clad Interaction (PCI).

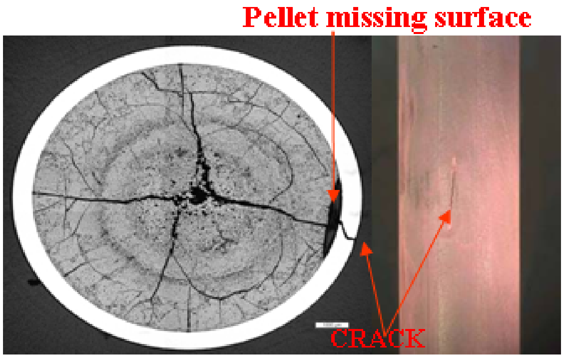

Figure 4.2: Pellet missing surface and resulting crack.

In a fission reactor these "defect" pellets can contribute to a mechanical failure of the zircalloy rods containing them. This missing "chip" may be responsible for increasing the *PCI* (Pellet Clad Interaction) failure risk. The *PCI* failure (see figure 4.1) can occur e.g. during the power ramp-up, where some of the fuel elements operating, before, in a lower power production are brought to a power increase causing thermal dilatation of the pellet. The action mechanism of *PCI* failure is the formation of stress corrosion cracking (*SCC*) by a combination of the aggressive fission products formed and the cladding stress from pellet expansion [30]. According to Billaux [30], careful analysis of fuel rods showed that where the edge of the pellet had been chipped is just in front of the crack in the cladding (see figure 4.2). The conjunction of a "pellet missing surface" with a cladding crack has also been observed a number of times in commercial reactors. The pellet missing surface behavior breaks the symmetry of the pellet-cladding mechanical system resulting in a stress concentration at the cladding inner surface [30].

The quasi-static tests chosen are the following:

- Diametral compression test
- Biaxial flexure strength of thin ceramic discs
- Micro-hardness test

4.1 Diametral Compression Test

Flexural tests are the most usually used for the determination of mechanical properties in fragile materials due to its simple execution. These tests however are only in relevance to determine the density of the existing defects on the traction surface [121]. Being so, it can not be used to study the properties of materials, which work under internal maximum tensions.

The “diametral compression” or “Brazilian” test is of fundamental importance in diverse engineering fields. Its use has been justified in terms of uniformity of (theoretical) stress distribution, avoidance of problems with collinearity of machine and specimen axes, and lower coefficient of variation [122]. It was first developed and used by Carneiro [123] a brazilian engineer who was trying to analyze the tensile strength of the cylindrical concrete rolls, which would be used for the transportation of a baroque church. Carneiro observed that concrete fracture developed almost strictly in a vertical plane connecting the line of contact between the cylindrical specimen and the compression plates concluding that the maximum tensile stresses grow perpendicularly to the loading direction and are proportional to the applied load. With this observation he proposed the theory of the testing method, which is not only used to test concrete cylinders but also rocks [124], coal [125], polymers [126], cement carbides [127], and finally ceramics [24, 128].

The most important fact to be noticed about the Brazilian Test is that fracture should be initiated by tensile stresses otherwise the results could not be considered useful. Because failure happens along the diametral plane of the applied load, it is commonly assumed that the nominal tensile stress causes the sample to fail [24].

Carneiro used for his stresses calculations the theoretical basis for the stress analysis of a disc subjected to two concentrated diametral forces published by Timoshenko [129] and also by Frocht [130]. Fahad [24] detailed in his work that Frocht illustrated the stresses state at any point within, and on, the disc by using three general equations:

$$\sigma_x = \frac{2F}{\pi D t} - \frac{2F}{\pi t}\left\{ \frac{x^2\,(R-y)}{\left[x^2+(R-y)^2\right]^2} + \frac{x^2\,(R+y)}{\left[x+(R+y)^2\right]^2} \right\} \tag{4.1}$$

$$\sigma_y = -\frac{2F}{\pi D t} - \frac{2F}{\pi t}\left\{ \frac{(R-y)^3}{\left[x^2+(R-y)^2\right]^2} + \frac{x^2\,(R+y)^3}{\left[x^2+(R+y)^2\right]^2} \right\} \tag{4.2}$$

$$\tau_{xy} = \frac{2F}{\pi t}\left\{ \frac{x\,(R-y)^2}{\left[x^2+(R-y)^2\right]^2} + \frac{x\,(R+y)^2}{\left[x^2+(R+y)^2\right]^2} \right\} \tag{4.3}$$

where F is the applied load, t is thickness of the disc, D the diameter, R the radius of the disc, σ_x and σ_y are normal stresses in the directions perpendicular and parallel, respectively, to the loaded diameter, and τ_{xy} is the shear stress (see figure 4.3a).

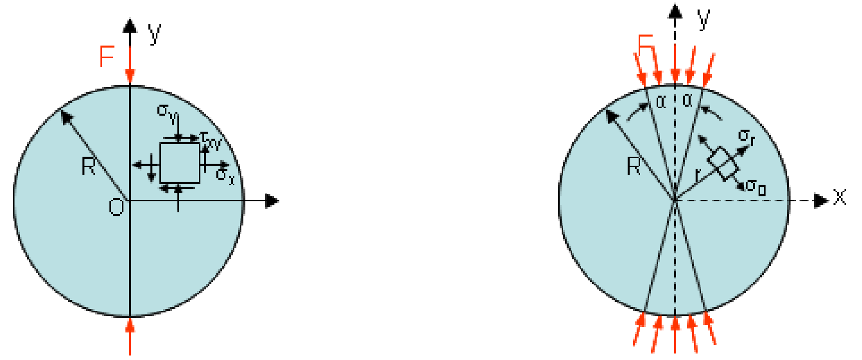

(a) Diametral disc under point load.

(b) Diametral disc under distributed load.

Figure 4.3: Diametral disc test representations.[24]

The normal stress, σ_x, along the load diameter ($x = 0$) is tensile and constant with magnitude equal to eq. 4.4.

$$\sigma_x = \frac{2F}{\pi D t} \tag{4.4}$$

Parallel to the load diameter is the compressive stress σ_y. The shear stress, τ_{xy} is zero along the diameter plane letting just σ_x and σ_y as the principal stresses on the plane.

Hondros [75] confirmed Frocht's [130] work even by proposing a more realistic approach to the problem. Frocht' s [130] analysis was developed assuming a point load on a thin disc however, in a real situation the load is applied to a finite area (see figure 4.3b). With this approach Hondros modified Frocht's equations above to reflect a finite load distribution but at the end the same tensile stress, σ_x, equation was obtained.

4.1.1 Test Procedure

The Brazilian test was performed on the sintered pellets from $Gp1$, $Gp2$ and $Gp3$. Except for the $Gp1$ pellets, which were tested as pressed, the fired pellets were ground after sintering since during this production step they do not shrinkage uniformly because of the green density variation becoming an irregular cylinder showing for instance the hourglass-like shape, which is characterized by a thinner diameter at the pellet central portion along the axial direction (see figure 4.4).

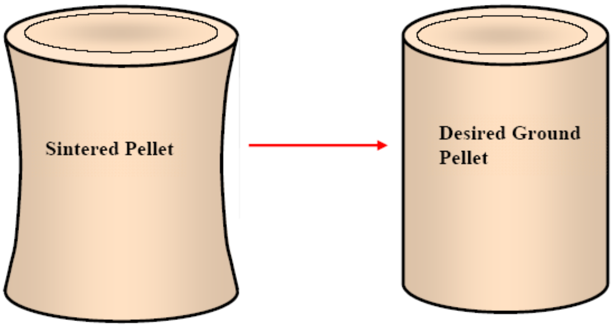

Figure 4.4: Hourglass effect (exaggerated).

The testing machine used for the experiments was an Erichsenpress equipment (see figure 4.5), a screw driven machine. The press can apply a maximum load of 20 kN. The load was increased with a rate of 0.2 mm/min and the maximum value for each tested sample was saved.

The usage of pad materials is justified by Darvell [122] for reducing the friction present between specimen and loading platen, which leads to stresses perpendicular to the end faces. Moreover, this thin pad of suitable material will provide a better distribution of the load all over the contact line between punchers and sample preventing failure due to stress concentration at a single point. If the specimen and the punchers contact during the test (determined by visual inspection of the pad after testing), the test result is invalid [131].

The padding material used for the experiments were copper foils with thickness of 0.10 mm.

4.1.2 Weibull Statistics

Because of its probabilistic nature fracture in brittle materials needs a statistical treatment. Furthermore, by measuring the strength of a series of similar ceramic samples a reasonable scatter in the results is normally found. This is due to the flaw size and distribution, which are responsible for failure, all over the ceramic matrix. For designing ceramic components a probabilistic approach is used in which the scatter is represented in a quantitative way so that these materials can be safely used [132].

The Weibull statistics is named after the swedish professor E. H. W. Weibull (1887-1979). Professor Weibull's theory became widely known and used since he published in 1951 the paper *A Statistical Distribution Function of Wide Applicability* [133]. At this work he presented seven case studies using the Weibull distribution. His theory is based on the weakest link concept, which states that the entire body will fail when the stress at any defect is enough for unstable crack propagation and consequently failure.

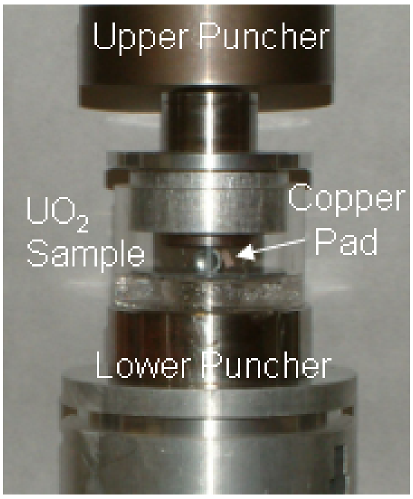

Figure 4.5: Erichsenpress.

The Weibull distribution function can be presented as:

$$P_S = 1 - P = exp\left[-\int_V \left(\frac{\sigma - \sigma_t}{\sigma_0}\right)^{m_w} dV\right] \tag{4.5}$$

where P_S is the probability of survival or, alternatively, the probability of failure [8] P of a stressed volume V. m_w is the dimensionless Weibull modulus, which describes the narrowness of the distribution or in other words it indicates how rapidly the strength falls as we approach σ_0. The characteristic strength σ_0 is a normalizing parameter often selected as a characteristic stress at which the probability of failure is 63.2 %. σ_t is the fracture stress and it is the threshold stress below, which the probability of failure is zero. It is usually set to zero since there is always a possibility, even for the best ceramic, that the material have a very large crack leading to a failure. With $\sigma_t = 0$ the distribution is reduced to a two-parameter equation (eq. 4.6).

$$P = 1 - exp\left[-\int_V \left(\frac{\sigma}{\sigma_0}\right)^{m_w} dV\right] \tag{4.6}$$

Now, if the full volume is under uniform stress the equation 4.6 can be written as equation 4.7.

$$P = 1 - exp\left[-\left(\frac{\sigma}{\sigma_0}\right)^{m_w}\right] \tag{4.7}$$

Weibull statistical analysis was carried out on each set of strength data using equation 4.7 and for the determination of m_w, which is the slope of the Weibull probability curve the next steps were followed:

1. Calculate the samples' strength
2. Rank these values in order of increasing strength
3. Determine P for the n^{th} sample by eq. 4.8:
4. Plot now the graphic P versus $ln\sigma$

$$P = ln\left(ln\frac{1}{(1-P_n)}\right) \tag{4.8}$$

where $P_n = (n-0.5)/N$ and N is the total number of measurements.

With Weibull modulus between 1 and 10 we have low-stable ceramics and with m between 10 and 30, stable ceramics

Consequently, in general, the smaller the Weibull modulus, the closer the fracture probability to the unit showing that the material is susceptible to failures in a wide band of strength. In the case of elevated values of this parameter, the failure probability tends to the unit just in a narrow interval around σ_0. So, a high Weibull modulus indicates a good quality of a ceramic, because the dispersion of the measured rupture tensions is smaller [31].

4.2 Squirrel Cage Experiment

The squirrel cage experiment was here introduced for simulating how superficial damages on green pellets would influence on the mechanical resistance of sintered pellets and also for analyzing the green pellet resistance against abrasion. In this later case the pellets were not sintered afterwards. Ideally the green pellets should have no damages but in reality chip loss is present after pressing the green pellets and during their transportation to the sintering furnace in every fuel fabrication plant. Improving the mechanical strength of the green pellets can be responsible for reducing the scrap inventory (see figure 4.6).

The test consists in damaging the green pellets (not fired) in a two-cylinder rotation machine as can be seen in figure 4.7. The cylinder walls are made of steel screen with a mesh of 1.5 cm allowing the produced ships from the damaged pellets to be collected on a plate. During the rotation of the cages the chocks among the pellets and also between the pellets and the metal screen produced chip losses, which simulate what happens by the fuel fabricators in their production processes. Depending on the size and position of the chip the pellet can be rejected and scrapped as can be

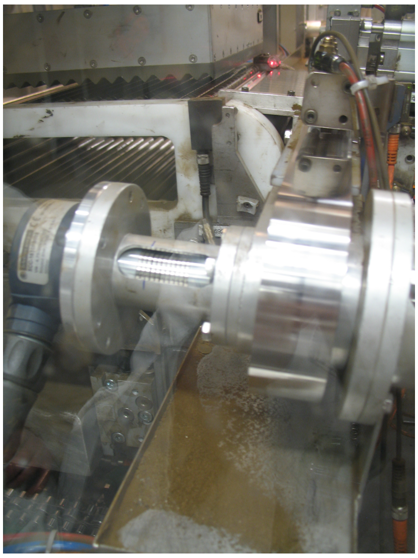

Figure 4.6: Picture showing green pellets chips produced during pressing.

seen in figure 4.8. The picture presents a pellet drawing with the maximal allowed dimensions for circumferential ships and two damaged pellets one with a chip on its circumference and another one with chips on the dishing. If a chip exceeds these limits on the pellet will be scrapped since at this specific position the pellet will be in contact to the cladding transmitting the heat generated by atomic fission. Moreover a critical chip on the circumferential area will reduce the heat conduction occasioning a 'cold area' on the cladding, which is surrounded by 'hot areas' that swell when heated. The not swelling from the 'cold area' will produce a concentration of stresses on it resulting in a crack at the cladding directly in front of the missing chip position (see figure 4.1 and 4.2).

Two types of analysis were performed. In the first one it was desired to compare how the mechanical resistance of pre-damaged pellets without additives, SQ-Std., and pellets with 0.3 % of keratin, SQ-Keratin., (both types having the same green density as can be seen in table 4.1) would be affected. In each of the two cylinders 7 green pellets were carefully placed and damaged for 20 rotations (80 seconds) with a rotation speed of $15\,rot/min$. The mass was measured before and after the experiment for each pellet group. Afterwards these pellets were sintered for 3 hours and ground for meeting the dimensions specifications and finally tested at the 'Brazilian' test.

Figure 4.7: Squirrel cage machine.

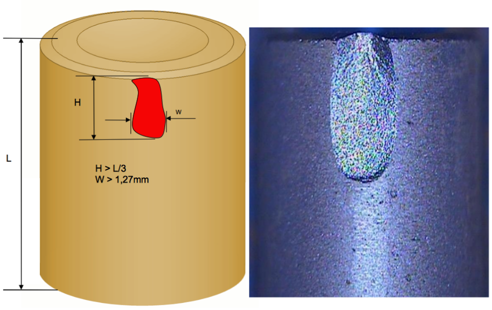

Figure 4.8: Drawing showing the allowed dimensions for chips and a damaged pellet.

Table 4.1: Squirrel cage samples.

Type	Gr. Density [g/cm^3]	Total Mass of 7 Pellets [g]
SQ-Std. Br-Test 01	6.02±0.03	67.31
SQ-Std. Br-Test 02		69.43
SQ-Keratin Br-Test 01	6.06±0.04	67.60
SQ-Keratin Br-Test 02		70.04
SQ-Std.	6.02±0.03	67.54
SQ-Keratin	6.06±0.04	67.96

The second analysis performed intended to investigate the chipping strength / abrasion hardness of green pellets SQ-Std. and SQ-Keratin. by increasing the number of turns causing an increase in the weight loss. Higher damage strength is an indicative of a better resistance to impacts during the production process.

Similarly to the first analysis 7 green pellets were carefully positioned in the cylinder and turned up to 600 rotations. At 20-50-100-200 and 600 turns the average weight loss of the 7 green pellets was measured.

The experiment was performed at room temperature ($20\,^{\circ}C$).

4.3 Indentation Test

With the indentation or microhardness test two material characteristics can be obtained, the hardness and the fracture toughness. For this end many testing techniques were developed over the years [8] but basically two of them are used for ceramics the Knoop [134] and the Vickers [134, 135]. About 60 % of worldwide community published ceramic hardness values, which were obtained with Vickers method whereas the Knoop method represents just 35 % [136].

The great advantage for the microhardness test is probably because its simplicity and the small amount of samples required for the determination materials properties. Nevertheless, for measuring the precise crack length and determining the type of cracks formed are the greatest problems for determining a reliable and comparable fracture toughness. Moreover, for means of internal comparison no restrictions are imposed but in case of comparison with external sources a especial care should be taken in consideration [65].

4.3.1 Hardness

Hardness is one of the most important ceramics parameters. It can be defined as the material resistance to overcome a permanent shape change when a force is applied by a sharp indenter or object. In addition to that, Wachtman et al [5] states that hardness, erosion, and grinding, are comparable parameters since all of them happen by a local deformation of the ceramic surface usually over a region on the order of micrometers in width and depth. Under the action of a sharp indenter the developed stress are enough to cause local plastic deformations from dislocations, twinning and grain boundary shear.

The hardness of a material sample is usually measured by indentation techniques like the Vickers method, which consists in pressing into a sample a sharp diamond square based pyramidal indenter with an angle of 136° between opposite faces with a given load, F, for a typical dwell-time of 10 seconds (see figure 4.9). The minimum distance between indentations was observed according to $ASTM1327$ [135].

For the determination of the hardness besides the applied load the arithmetic mean length of the two diagonals formed is calculated. The characteristic hardness can be then calculated by using two formulas

$$H = \frac{1.8544F_i}{(d)^2} \tag{4.9}$$

$$H = \frac{2.000F_i}{(d)^2} \tag{4.10}$$

where F is the indentation load and d is the average imprint diagonal value. In eq. 4.9 the constant number is calculated using the contact area of the four faces of the indenter, whereas in eq. 4.10 the constant is calculated using the projected area of the indenter. Many in the ceramic community use the projected area but on the other hand the contact area definition is also widely accepted definition. Both definitions differ by 7.9 % [137].

For the present work the Vickers method was used and the hardness was calculated with eq. 4.9.

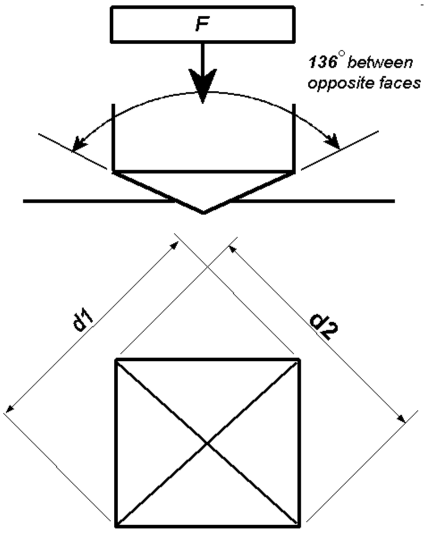

Figure 4.9: Vickers indentation [25].

4.3.2 Toughness

It was already mentioned in section (2.2) that the fracture toughness can also be calculated from an indentation test. In this same chapter it was defined that K_I, the stress intensity factor normal to the crack plane, at the tip of a single crack increases along with the increasing load until an unstable or critical crack propagation occurs K_{Ic} [26]. Hence, the fracture toughness is a specific material property independent on its dimensions, which describes the material's resistance against crack propagation.

For the determination of K_{Ic} equation from chapter 2.2.8($K_{Ic} = 0.016\,(E/H)^{1/2}\,F\,(1/c)^{3/2}$) was used. The hardness as well as the average crack length accounted from the imprint centre and the indentation half-diagonal length were measured as shown in figure 4.10.

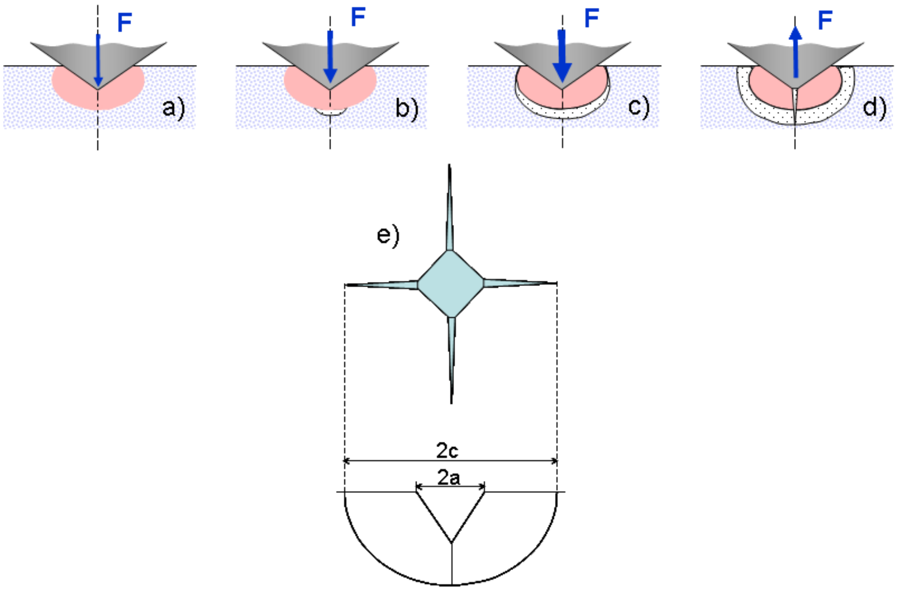

Figure 4.10: Hardness and fracture toughness determination [26]. In *a*, *b* and *c* it is shown the crack evolution by increase of the indentation load and in *d* the indenter is removed letting behind the diamond imprint. In *e* an indentation top view as well a cross section view with crack dimensions are shown.

4.4 Creep Behavior

Differently from the other experimental procedures, which were performed at room temperature, the creep behavior experiment was done at elevated temperature allowing us to have a more complete overview of the ceramic fuel behavior under a "cold" and under a "hot" condition.

The compression creep tests were performed using a creep furnace (see figure 4.11) from the company FCT. The thermocouple used here is made of tungsten-rhenium ($W - 3\,\%\,Re/W - 25\,\%\,Re$) and the pressing punches are made of tungsten. After the sample is placed in the furnace and the upper punch is positioned applying a minimal load to the sample the furnace is evacuated and the process parameters such as gas mixture, temperature, time and load are adjusted the experiment can be start. The creep atmosphere, dry Ar/H_2 ($5\,\%\,H_2$), was the same for every sample tested and the temperature, raised at a rate of $50\,°C/min$, for all tested loads was set at $1500\,°C$. The cooling down was also performed at a rate of $50\,°C/min$.

After the test completion the length, diameter and density of the sample was again measured. The sample was then metallographic analyzed to measure the after-test grain size and porosity.

From the deformation curves, above the initial elastic extension stage and the primary creep stage, the creep rate was determined at the steady creep stage after a sample deformation of $\sim 3\,\%$. Nevertheless, at tests with very low creep rates a smaller deformation values of about 0.5 or $1\,\%$ was considered.

The creep rate could be calculated by equation 4.11 where $\dot{\varepsilon}$ is the creep rate in $mm/mm/h$ (often expressed in $\%/h$), L is the initial sample length in mm, ΔL is the change in sample length after time t in hours.

$$\dot{\varepsilon} = \frac{\Delta L/t}{L} \tag{4.11}$$

The tested samples are presented in table 4.2 and in table 4.3. The samples produced for our work are those containing, before sintering, $0.3\,wt\%$ of keratin fibers. The other samples used for the comparison were obtained from other experiments in the ceramic laboratory of AREVA NP GmbH in Erlangen, Germany and from Vidal [138].

For the creep tests all samples containing dishing are ground in order to be perpendicular to the compression axis. This preparation procedure was not performed to the samples with keratin fibers because the pellets were already pressed without dishing. Force transmission to the testing pellet is then performed by two tungsten punches. The pellet and the punches are not in direct contact. Between them are positioned aluminum oxide disks responsible for avoiding the melting together of the punches and the pellet.

The calculated creep rates of this work represent a mean estimation on a given deformation area, as a function of the applied stress, i.e.:

- $\sigma < 30MPa: \ 1 < \dot{\epsilon} < 3\%$

- $30 < \sigma < 90MPa: \ 1 < \dot{\epsilon} < 6\%$

Table 4.2: As-sintered creep experiment pellets tested at 1500 °C.

Characteristics	Tested creep samples by 1500°C		
	Std. UO_2*	$UO_2 + Cr_2O_3$*	$UO_2 + U_3O_8$**
TD[1] [%]	96.52	97.15	95.68
Grain size [μm]	12	38	2
Mass [g]	7.16	7.25	3.04
Length [mm]	12.86	12.77	8.22
Diameter [mm]	8.21	8.25	6.76
Creep load [MPa]	15/45/60/75/90	15/45/60/75/90	15/45/60/75/90

*Courtesy AREVA NP GmbH
**Vidal [138]

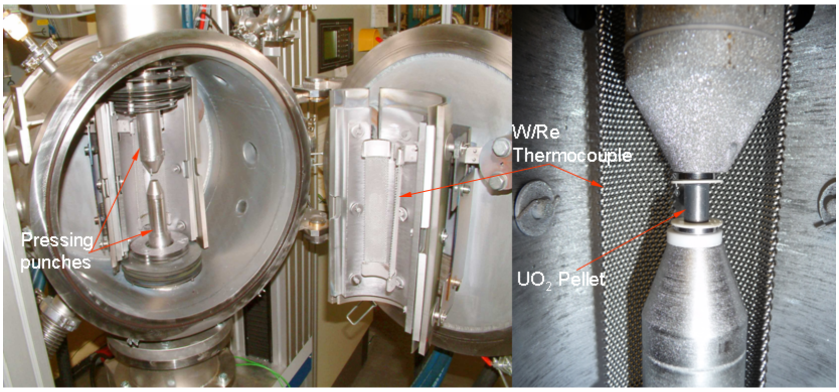

Figure 4.11: FCT creep furnace where between the two tungsten punches a testing pellet can be seen.

Table 4.3: UO_2-keratin fiber creep samples before test at $1500\,°C$.

Characteristics	Tested UO_2-keratin fiber creep samples by $1500°C$			
	Sample 1	Sample 2	Sample 3	Sample 4
Creep load [MPa]	15	30	60	90
TD[1] [%]	96.39	96.32	96.44	96.24
Grain size [μm]	Bi-modal 6 - 16			
Mass [g]	8.27	8.43	8.40	8.45
Length [mm]	15.07	15.23	15.25	15.29
Diameter [mm]	8.15	8.19	8.17	8.18

[*] Courtesy AREVA NP GmbH

[**] Vidal [138]

Chapter 5

Analysis of the Results

This chapter presents the microstructure analysis of the tested samples discussing their characteristic advantages and disadvantages as well as the influence of the specific microstructure on the mechanical resistance and reliability of each type of produced pellet lot.

Afterwards, the analysis concentrates on the obtained results of the different testing procedures being each procedure examined and discussed in a separated sub-chapter and when pertinent comparisons between the testing procedures were made.

5.1 Microstructure Analysis

The final pellet microstructure is defined by a series of influencing factors such as the presence of additives in the powder mixture, the pressing green density and also by the sintering temperature, sintering time and sintering atmosphere.

The result analysis and the discussion at this section were split in the coming subsections. In the first one the influence of the different additives to the pellet microstructure was taken in account. In the second one the contribution of the green compact density was considered. And finally at the last one, the sintering dwell time as well as the first two influencing factors were brought together for characterization of the fuel microsection.

Microsection pictures will be displayed as they are mentioned in the text. Unfortunately it will not be possible to attach all microsection pictures taken. Per pellet type it will be displayed the two most relevant grain size distribution and the two most relevant pore size distribution.

5.1.1 Additives

In the subsection 3.4 it was presented the additives used for the fuel produced in this work. Some characteristics such as the additive density, their temperature of decomposition, their chemical composition and the amount added to the fuel were already mentioned.

The measured average additive particle size as well as the particle size for the used UO_2 are shown in table 5.1.

Table 5.1: Average additive and UO_2 particle size.

Additive	Average particle size (d(0.5)) [μm]
ADS	3.774
AZB	6.012
OS	8.833
UO_2	57.761
OP	79.388

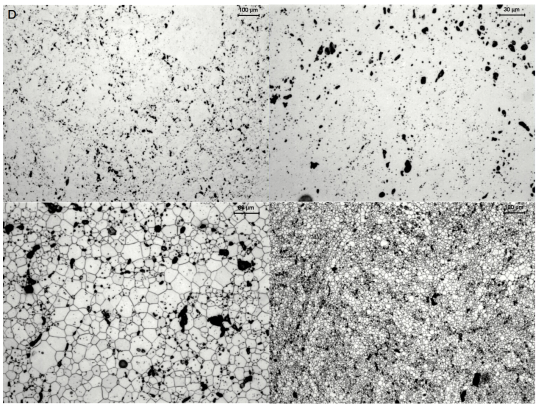

Figure 5.1: Pellets type D microsections. For these pellets an earlier addition of AZB produced a more homogeneous porosity distribution.

The keratin fiber was not included in the table 5.1 because it was not analyzed with the *Mastersize 2000*, but with a light microscope. From this analysis it was obtained that the fiber length range (L in μm) was $80 \leq L \leq 2000$, whereas the fiber diameter range (D in μm) was $35 \leq D \leq 110$.

Particle size distribution for the different additives as well as for the UO_2 powder used are presented in appendix A. The biggest particles were for the oxidized powder, also known as green U_3O_8, and for the UO_2 powder. These two powders present such “large” particles because they quite easily agglomerate forming bigger particles. In order to reduce their size a sieving or milling process can be used. Milled UO_2 powder can have its particles reduced to $\sim 1\,\mu m$. The other additive types have quite fine particles.

Microsections of pellet types D, E, F and L are now presented. Pellets D and L have in their composition the same additive, AZB. It was added to pellets D at the blending step while in the case of pellets L it was added after the granulation step. The additon of AZB at different moments of the fuel fabrication process produced pellets with different microstructure. Because of a later addition of the AZB to the UO_2 powder, the additive particles stay around the granulated UO_2 particles. When the additive is added to the UO_2 powder before the mixture is more homogeneous.

Pellets D microsections show that the earlier addition of the AZB produced a more homogeneous microstructure with the porosity spread all over the pellet matrix (see figure 5.1). In addition to that it can be observed that the grains closer to porosity cluster were smaller than the others. By pellets L the addition of the AZB to the granulated UO_2 powder produced big areas of grains surrounded by pore clusters (see figure 5.2). The grains inside these areas are almost free of pores. Similarly to pellets D the grains closer to the pore clusters are smaller than the most distant ones.

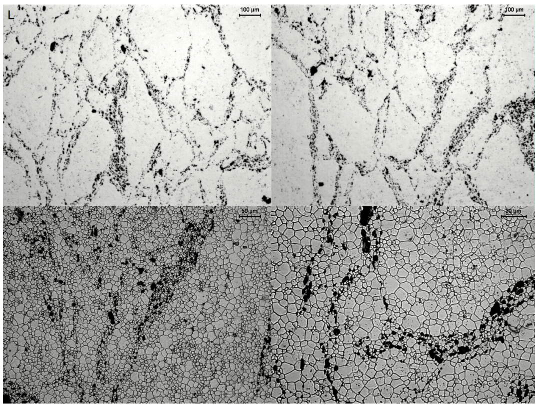

Figure 5.2: Pellets type L microsections. The granulate structure produced big areas of grins surrounded by pore clusters.

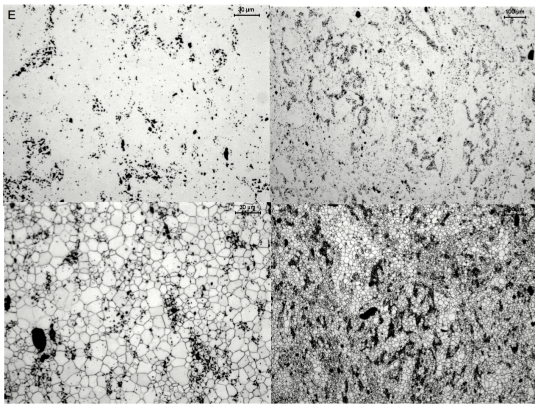

Figure 5.3: The OS added to pellets type E produced a structure with fine pores homogeneously distributed with some porosity clusters.

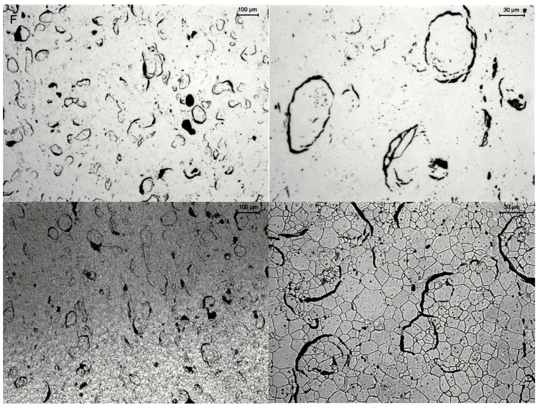

Figure 5.4: Pellets type F prepared with OP produced porosity in form of hooks.

Pellets E and F were respectively prepared with oxidized pellet scrap (OS) and oxidized powder (OP) added to the UO_2 powder. It was shown above that the OP particles easily agglomerate producing quite bigger particles than the OS ones. This is the main aspect determining the porosity distribution in pellets with these two types of additives. Pellets with OS (see figure 5.3) present fine porosity (see table 5.2) distributed all over the pellet matrix with some porosity clusters whereas pellets containing OP show in its matrix porosity in form of hooks as can be seen in figure 5.4. More uniform grain size distribution can be observed in pellets E than in F. In pellets F microsections it can be observed that the grains closer to the porosity clusters are smaller than the farther ones. Nevertheless, the measured general grain size is similar in both

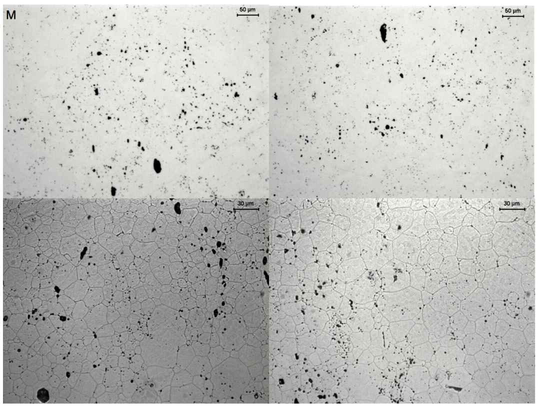

Figure 5.5: Microsections of standard pellets type M.

cases since they had the same green density and were sintered for the same sintering dwell time of 3 hours.

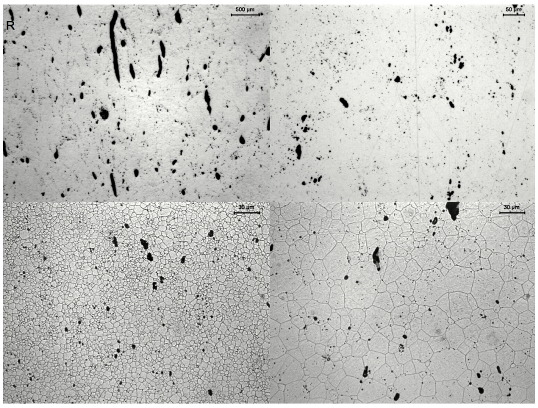

Figure 5.6: Pellets type R prepared with keratin fibers. Elongated pores and bi-modal structure are their main characteristics.

Pellets M, R and T have the same green density, $6.2\,g/cm^3$, and the same sintering dwell time, 3 hours, but have different additives. Pellets M are standard, no additive in their composition. Pellets R have $0.2\,wt\%$ of keratin fibers while pellets T have in their composition $16.68\,wt\%$ of OS. In their microsections in figures 5.5, 5.6 and 5.7 as well as in table 5.3 it can be observed that by the standard pellets M and the OS ones the amount of large pores is much less than in the case of the pellets R with keratin fibers. Similar grain sizes are seen by pellets M and

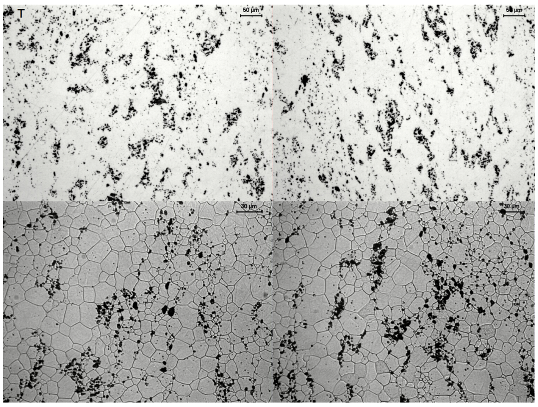

Figure 5.7: Pellets type T microsections showing the fine porosity as well as the some pore clusters.

T. However, the grain size distribution by pellets R present many of the larger grains positioned at pellet border while the smaller ones were concentrated more in the central part of the pellet. This phenomenon is discussed in the coming 5.1.3 subsection.

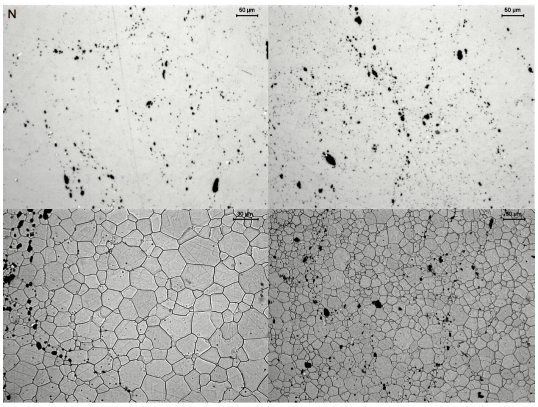

Figure 5.8: Standard pellets type N microsections showing porosity free grains.

Pellets N are standard and pellets U have $0.3\,wt\%$ of keratin fibers in their composition. Both types have the same green density, $6.2\,g/cm^3$, and were sintered for 9 hours. The resulting microstructure can be seen in figures 5.8 and 5.9. Pellets N present quite fine porosity. Furthermore, it can be observed several grains without any porosity a clear sign that the achieved theoretical density is quite high. Pellets U have a much higher amount of larger pores and have

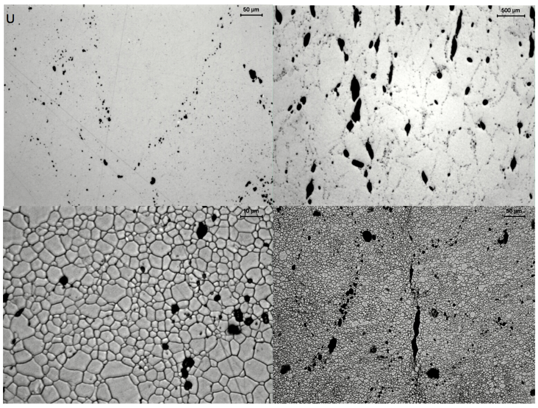

Figure 5.9: Microsections of the keratin fiber pellets type U, which were sintered for 9 hours. Grains closer to the pores are smaller than the more distant ones.

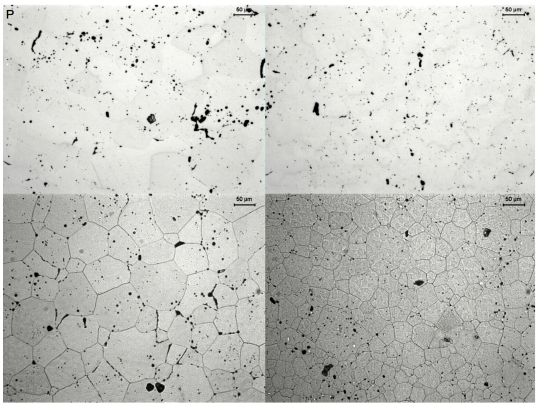

Figure 5.10: Standard pellets type P microsections. These pellets were sintered for 9 hours presenting a quite high theoretical density.

also the presence of clusters. Pellets N have a uniform grain size distribution whereas pellets U has the bi-modal structure. In both types the amount of larger grains is similar.

Pellets P, V and X are now analyzed (see figures 5.10, 5.11 and 5.12). Their common characteristics are the same green density and the same sintering dwell time of 9 hours. Pellets P are standard while pellets V and X have respectively in their composition $0.2\,wt\%$ and $0.3\,wt\%$ of keratin fibers. Similarly to the other standard pellets here analyzed, pellets P also have a very fine porosity distribution and present some grains without any porosity since their final theoretical density (TD) is above $98\,\%$. In the case of pellets V the porosity amount was slightly

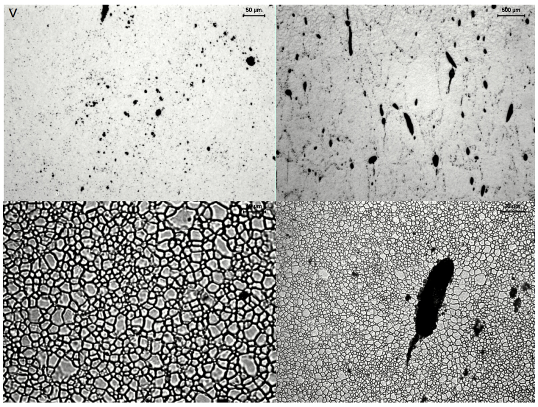

Figure 5.11: Pellets type V have $0.2\,wt\%$ of keratin fibers in their composition. The presented microsections show the grain size distribution in two magnifications. Larger grains were found more at pellet borders while the smaller ones were located at their central part.

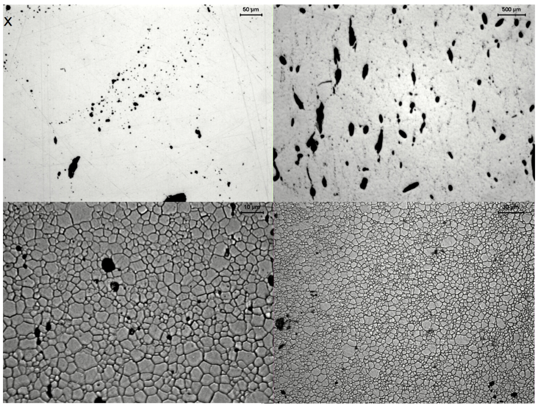

Figure 5.12: Keratin fibers pellets type X microsections show many porosity free grains. The bi-modal structure is also present.

lower as in pellets X because of the also smaller amount of additive added. The presence of larger pores is also lower than in X and in both cases there is the presence of porosity cluster. Pellets V presented in general a higher amount of larger grains than pellets X. In both types there are areas where no porosity is found inside the grains.

Table 5.2: *Gp*2 sintered pellets porosity characteristics. The table show the general porosity volume, the porosity volume in three pore size range and the mean pore size at two magnifications.

Type	General porosity volume [%]	Porosity volume [%] in the pore size range:			Mean pore size at 100x [μm]	Mean pore size at 500x [μm]
		$< 10\mu m$	$10 - 20\mu m$	$> 20\mu m$		
A	2.96	1.51	0.46	0.99	16.65	2.51
B	2.56	2.23	0.23	0.11	5.47	1.98
C	2.03	1.71	0.21	0.10	5.62	2.66
D	4.69	3.17	1.22	0.30	7.79	5.38
E	4.55	3.76	0.67	0.12	6.01	3.19
F	4.15	1.51	0.74	1.90	1.63	4.95
G	4.56	1.64	0.18	2.74	7.43	2.67
H	2.34	1.68	0.35	0.31	8.77	2.33
K	2.35	1.79	0.29	0.27	10.12	1.96
L	4.88	2.88	1.55	0.45	8.41	1.37

5.1.2 Green Density

The pellet green density is a very relevant production characteristic, which directly influence the sintered pellet microstructure. A higher green density leads to a higher final sintering density, since the higher compaction achieved enables a faster densification during sintering. In fact, even

Table 5.3: *Gp*3 sintered pellets porosity characteristics. The table show the general porosity volume, the porosity volume in three pore size range and the mean pore size at two magnifications.

Type	General porosity volume [%]	Porosity volume [%] in the pore size range:			Mean pore size at 12,5x [μm]	Mean pore size at 200x [μm]
		$< 10\mu m$	$10 - 20\mu m$	$> 20\mu m$		
M	1.68	1.16	0.42	0.10	—	5.87
N	2.22	1.45	0.63	0.14	—	6.49
P	1.45	1.05	0.36	0.04	—	5.88
Q	4.45	0.97	0.45	3.03	117.49	6.62
R	3.79	0.76	0.47	2.56	121.74	7.00
S	3.86	0.70	0.27	2.89	125.31	7.63
T	3.60	2.67	0.77	0.16	—	5.75
U	3.71	0.74	0.27	2.70	150.4	8.68
V	3.03	0.83	0.41	1.80	101.87	7
X	3.40	0.57	0.24	2.58	130.91	9.1

a small variation in the green density will certainly result in elevation or reduction of the after sintering density.

The pellet pressing strength was adjusted according to the final pellet length and also according to the additive mixture to the UO_2 powder. At figure 5.13 a graph showing the necessary applied load to different pellet types is presented. As one can see the desired green density an adjustment at the pressing load was necessary, since each type of additive reduces or increase the friction between powder bed and die walls. Furthermore, a longer pellet will require a higher pressing load than a shorter one as can be seen at the pressing load of pellets A and K. Both of these types are standard pellets, however pellets K are $18\,mm$ long while pellets A are just $13\,mm$ long, which implies that pellets K needed some more strength in order to have the same green density of pellets A.

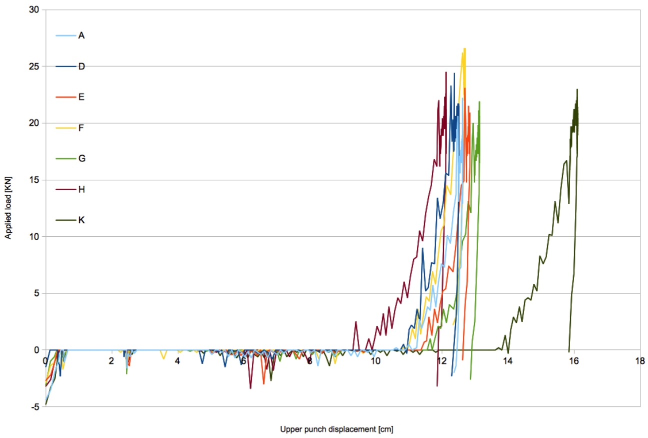

Figure 5.13: Pressing load development of different pellet types.

This subsection presents comparison of pellet types with different green densities, however with the same sintering dwell time.

The standard pellet types A and M were sintered for 3 hours. Pellets A had a green density of $5.86\,g/cm^3$ while pellets M had $6.21\,g/cm^3$. The final density of pellets M reached 98.36 % of the UO_2 theoretical density while pellets A density was 97.17 % of TD. The grain size distribution of pellets M presented in average larger grains than pellets A. A higher amount of larger pores were observed in pellets A than in pellets M.

Pellets Q, and S were prepared with the same amount of keratin fibers however were pressed with different green densities. Pellets Q had a green density of $5.84\,g/cm^3$ while pellets S had a green density of $6.22\,g/cm^3$. This variation in compaction resulted in a higher sintering density and consequently a lower general volume porosity for pellets S than in pellets Q. Also resulted in larger grains at the pellets S matrix.

Pellets U and X were also prepared with the same amount of keratin fibers but were pressed with different green densities and sintered during 9 hours. Pellets U and X had a green density of $5.85\,g/cm^3$ and $6.20\,g/cm^3$ respectively. The higher sintering dwell time resulted in similar observations as for the last comparison, i.e, higher theoretical density for pellets X, lower general porosity volume and larger grain size for pellets X.

5.1.3 Sintering dwell time

In the sintering process there are three major influencing factors the temperature, the atmosphere and the dwell time at the isothermal. Here, the influence of the first two factors was not investigated.

As already mentioned in subsection 3.2.5 the continuously increasing of the sintering time at the isothermal will lead to a reduction of the sintering rate due to the progressive reduction of the porosity, i.e., the theoretical density of the material is about to be reached. Furthermore, a progressive reduction in the number of pores leads also to a reduction of the rate of sintering with time [91].

The sintering kinetics was studied at three different dwell times 3, 9 and 27 hours at the isothermal level by $1770°C$. The 3 hours dwell produced pellets with theoretical densities between 95 % and 98 % (see tables 5.4 and 5.5). This great variation derives from the different additives in the pellet composition. Pellet types with additives in their composition sintered to a maximal density of 96.44 % whereas those without additives reached until 98.36 %, which is a quite high sintering value. The other two dwell periods produced pellets with densities above 97 % for those without additives and maximal 97 % for the ones with additives.

Increasing the sintering dwell period by the isothermal will not always mean that the final density will be the highest. By comparing the three standard pellet types, A, B, C, which had the same starting point, i.e, the same green density and production process, but different dwell times of 3, 9 and 27 hours respectively, it can be observed that the density increase was not proportional to the increase in the dwell time. This behavior happens because the compaction physical limits were reached. In other words, once the capacity of the sintering process to eliminate the porosity is about to be reached increasing the dwell time will bring almost no effect to the final density of the fuel pellet. Tables 5.2 and 5.3 shows the measured porosity by the Saltykov model [96], the volume of porosity in three pore size ranges and also the mean pore size at two different magnifications. Different magnifications were used because of the existence of very fine and large pores. The highest magnification was used for the analysis of the fine porosity while the lowest one was used for the larger pores.

Among these three pellet types, pellets type C are those with the smallest general porosity volume, a expected value since they had the highest dwell time. So since the dwell time of the pellets type B was higher than the dwell time of pellets type A it would be expected that the type B pellets had had a smaller general porosity volume than pellets type A, which does not happen. This was because of the uncertainty of the determination method. As already mentioned in the subsection 3.2.5 the Saltykov model can be influenced by the quality of the microscope, quality of the camera and also by the operator experience. For this reason the determination of the general porosity volume the Archimedes' Principle was the one chosen. The Saltykov model gives us a good idea of the porosity distribution, however it is more prone to present greater inaccuracy at the determination of a sample density.

The porosity distribution in three size ranges previously presented in tables 5.2 and 5.3 gives us a better picture to what the pellet microstructure looks like. Pellets type B and C had much less larger pores than pellets type A, which also presented the smallest amount of fine porosity as can be seen in figures 5.14, 5.15 and 5.16. In addition to that, the porosity measurement with two different magnification, presented in these tables, also points out that a higher amount of larger pores are present in pellets type A.

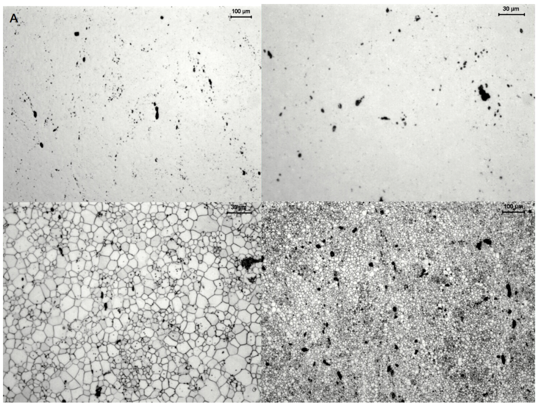

Figure 5.14: Standard pellets type A microsections. Above pore size distribution in two magnifications and below two grain size microsections showing the grain size distribution.

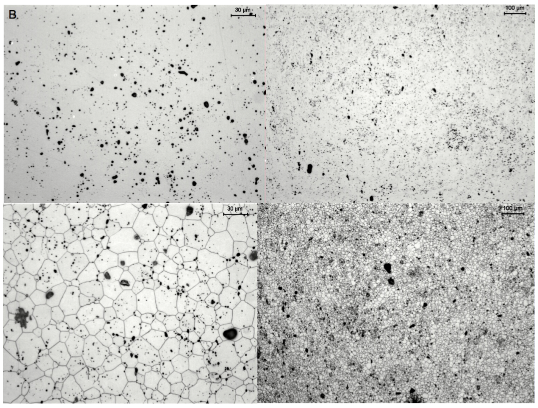

Figure 5.15: Microsections of the standard pellets B, which were sintered for 9 hours. Above the pore size distribution in two magnifications and below the grain size distribution.

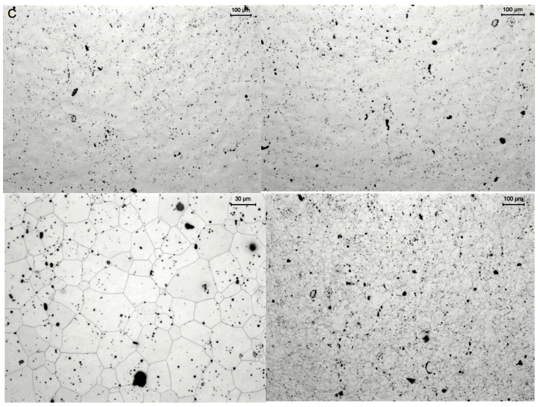

Figure 5.16: Standard pellets type C microsections. These pellets were sintered for 27 hours. Above are presented their pore size distribution in two magnifications and below their grain size distribution.

The fine porosity existent in pellets is quite difficult to be eliminated. If the external and internal forces acting on the pore walls reach a point of equilibrium the fine porosity will not disappear. Applying more energy to the system will bring almost no effect to the increase of the density.

Table 5.4: *Gp*2 sintered pellets grain size characteristics at two magnifications 500x (larger grains) and 1000x (smaller grains) as well as the pellet TD.

Type	Grain size distribution at different magnifications [μm]:		TD[1] [%]
	$500x$	$1000x$	
A	10.87	—	97.04±0.19
B	17.97	—	97.44±0.10
C	24.65	—	97.97±0.05
D	11.58	—	95.31±0.09
E	13.70	—	95.45±0.06
F	13.57	—	95.85±0.07
G	11.74	2.9	95.44±0.12
H	13.31	—	97.66±0.06
K	14.49	—	97.65±0.06
L	14.40	—	95.12±0.09

[1] Theoretical density to UO_2(10.96 g/cm^3)

The grain size distribution was determined using the linear intercept method. By this method lines are traced through the grain structures captured by the light microscope. The total length of the traced lines is divided by the total number of grains intercepted by them. At least 150 grains have been measured per microsection.

The grain size distribution of pellet types *A*, *B*, *C* presented a clear tendency of grain size increase (see table 5.4) with the sintering time, a fairly consistent result.

Table 5.5: *Gp*3 sintered pellet grain size characteristics at two magnifications 500x (larger grains) and 1000x (smaller grains) as well as the pellets TD.

Type	Grain size distribution at different magnifications [μm]:		TD[1] [%]
	$500x$	$1000x$	
M	13.00	—	98.32±0.03
N	15.00	—	97.78±0.19
P	22.92	—	98.55±0.04
Q	14.60	3.00	95.55±0.41
R	18.65	4.98	96.21±0.11
S	16.00	6.10	96.14±0.31
T	12.46	—	96.40±0.12
U	15.94	4.68	96.29±0.12
V	18.42	4.20	96.97±0.10
X	16.60	4.08	96.60±0.09

[1] Theoretical density to UO_2(10.96 g/cm^3)

So, by the presented facts and arguments, it is clear that the increase of the sintering dwell time will not consequently bring an increase of density. Nevertheless it is true that by increasing the dwell time the grain size will increase.

For achieving, in a more effective way, higher density values other factors must be considered such as the sintering temperature or the green compact density. Even though the degree of sintering increases with increasing time, the effect is small in comparison to the temperature dependence. The rate of sintering decreases with increasing time [27]. As can be seen in figure 5.17, the largest change shows up at the earliest periods. Thousands of hours are normally required in order to produce changes in sintering that could be brought about by an increase in sintering temperature of perhaps 40 °C. The loss of driving force with increasing time at any temperature is one of the reasons why it is so difficult to remove all porosity by sintering [27].

As for the pellets with additives, more specifically those containing keratin fibers, two comparisons were made, one with pellet types Q and U and the second one with pellet types S and X. In the first analysis the pellets had the same amount of additive (0.3 %) at their composition, were pressed with the same green density (~ 5.8) but were sintered by 3 and 9 hours (dwell time) respectively. In the second group the pellets also had the same amount of additive (0.3 %), the same green density (~ 6.2) and different sintering dwell times of 3 and 9 hours.

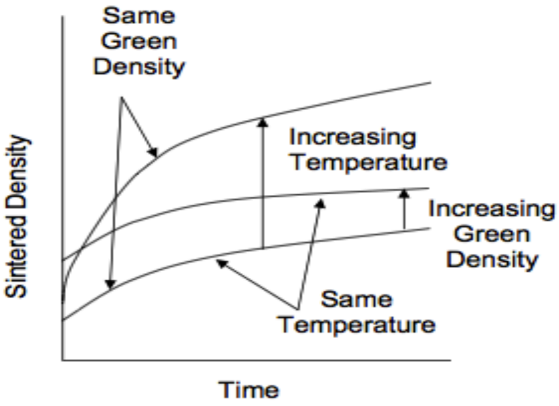

Figure 5.17: Sintering density vs. sintering time curves illustrating effects of increasing green density and sintering temperature on the densification process [27].

The characteristic pore shape for these pellets differs quite a lot from the more spherical shape found in the standard pellets (A, B, C). In figure 5.9 it can be seen that elongated pores are spread all over the pellet matrix. Spherical pores are also present, however their influence in the pellet mechanical strength is reduced when such elongated pores are observed.

The theoretical sintering density of pellets U (96.26 %) was a bit higher than for pellets Q (95.53 %) since their sintering dwell time was 6 hours longer. Their pore size distribution can be seen in table 5.3 and shows, for both pellet types, that large elongated pellets have a great influence on the general pellet porosity volume. The grain size distribution shows that larger grains are present by pellets U. That's because of their longer sintering dwell time.

In the second comparison group results are similar to those in the previous group, i.e., the theoretical sintering density of pellets X (96.62 %) was higher than for pellets S (96.17 %) also because of the longer dwell time by pellets X. The remark at this comparison group here comes to the fact that pellets X presented larger pores at $1000\,x$ magnification as well as at the combination of both magnifications. For this kind of result two conclusions can be presented, first there was an error during the measurement, or second the further grain growth in pellets X would need more energy to continue growing.

Another interesting characteristic observed at all pellets with keratin fibers is that most of the larger grains were positioned at the borders of the pellet while the smaller grains were at the central part. This phenomenon was called bi-modal structure.

A possible explanation to this phenomenon is that the presence of the keratin fibers acted in a certain way to delay the grain growth. The grain growth takes place mainly at the final stage of sintering. By this stage the pores should present a spherical shape and should also be closed allowing a further growth of grains. In the case of pellets with keratin fibers, the pores still have a cylindrical shape by the end of the final stage of sintering, which implies in a discontinuous or exaggerated grain growth at the points with less pores. Coble [18] explained that if the grain growth started before all big pores were eliminated such abnormal, however interesting, behavior would happen.

5.2 Diametral Compression Test

With the diametral compression test the mechanical strength of the green or sintered UO_2 pellets was analyzed. The strength influencing factors detailed in chapter 2 as well as the microstructure characteristics will determine the pellet mechanical behavior during the experiment.

In subsection 3.2.5 it was presented the different pellet groups that would be tested by the diametral compression test. However, differently from the $GP2$ and $GP3$ pellet groups, which were sintered in a dry H_2 atmosphere by $1770\,^{\circ}C$ the $GP1$ green pellets were not sintered being tested as they were compacted. The objective of testing $GP1$ green pellets was to determine the best length to diameter relation. Results in table 5.6 show that the combination of the longest pellets ($L = 18\,mm$) and those having 8 mm in diameter presented the best Weibull modulus and Weibull strength values.

If the diameter is fixed and the length is increased it is clearly seen that the Weibull modulus tends also to increase, i.e. if the $L/D\,ratio$ is increased the reliability of the green pellets will be

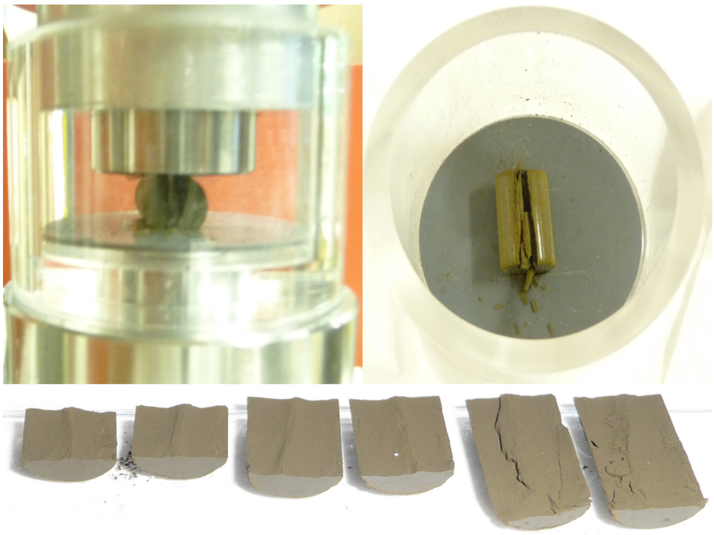

Figure 5.18: GP1 diametral compression test samples.

higher. This reliability increasing tendency is also observed if the length value is fixed and the diameter is raised, although the $L/D\,ratio$ is decreasing.

Another interesting observation is that the maximal Weibull modulus is reached for the largest volume of each reference diameter. Hence, the obtained values for $D10L13$ and $D10L18$ are very expressive if it is considered that ceramics with a Weibull modulus between 10 and 20 are considered ceramics of good quality. It is evident that the green pellets are not the final sintered product but if the quality achievement here observed could be transferred to the sintered pellets the production costs could be reduced.

Figure 5.19 shows that there is a correlation between the pellet volume and the Weibull modulus. By increasing the pellet volume there was an increase of the pellet reliability with an exponential correlation index of 0.75. It can be seen in figure 5.20 that an even better exponential correlation index is obtained when, for instance, just the pellets with diameter of $8\,mm$ were selected.

The variation of flaw density distribution could be an explanation for higher Weibull modulus for those samples with the highest volume. By having a larger sample volume both the volume and surface flaws are not as concentrated as in a sample having a smaller volume. This point of concentration can be the starting point of failure. Furthermore, the failure mode can be considered as a quasi-ductile.

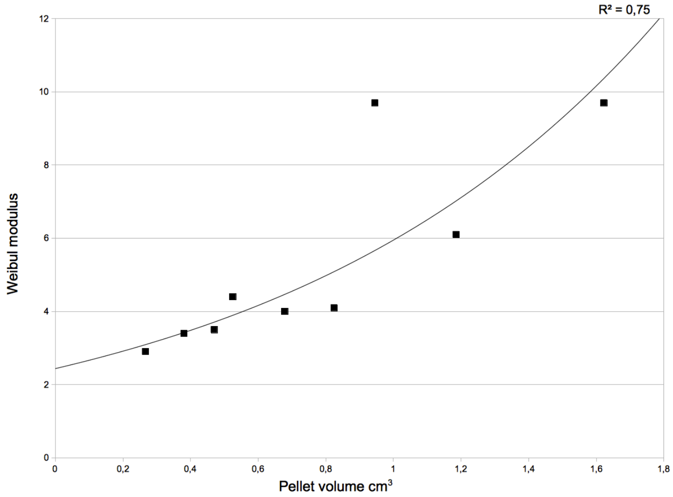

Figure 5.19: Graph showing the exponential correlation between the pellet volume and the Weibull modulus.

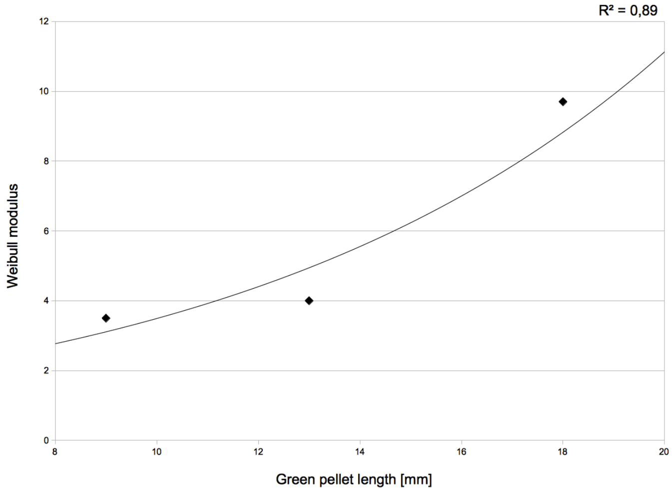

Figure 5.20: Graph showing the exponential correlation between the pellet length and the Weibull modulus by $GP1$ pellets $D8L9$, $D8L13$, $D8L18$.

As for the Weibull strength no representative observation for all green pellet groups could be done. By keeping the height fixed and increasing the diameter, $L/D\,ratio$ decreases, the groups with height 6 and 18 mm increased the Weibull strength obeying the Weibull statistics theory. Having the height fixed at 9 mm and increasing the diameter presented a reversal result from the Weibull theory.

In the $GP2$ group of pellets some comparison analysis can be done. The powder for the standard pellets A, B and C were similarly prepared. However, the pressed pellets were sintered for 3, 9 and 27 hours respectively. All the three pellet types had a quite low porosity volume having a higher amount of pores smaller than 10 μm (see table 5.2). Pellets A presented the highest amount of pores larger than 20 μm, which may be the reason for having the lowest Weibull modulus among the three pellet types. The Brazilian test results of these pellet types presented in table 5.7 show that by increasing the TD there will be also an increase of the reliability (higher Weibull modulus). The Weibull strength was slightly higher for pellets B sintered for 9 hours, while the value for pellets A and C were the same.

Pellet types D and L contain AZB as additive. Pellets D had this additive added before the pre-compaction, which allowed the porosity to be uniformly distributed all over the pellet matrix. In pellets L it was added afterwards producing pore clusters. The grains inside these pore clusters were quasi porosity free. In both pellet types the grains close to the pores were smaller than the more distant ones. The production process did not influence much on the TD as well as on the porosity distribution. Pellet L grains are slightly larger than pellets D. Their Brazilian test results clearly show that the homogeneous (pellets D) structure and the granulate (pellets L) structure behave in a similar way as can be seen in tables 5.7 and 5.8.

Pellets E had OS as additive, pellets F were prepared with OP as additive and pellets G had the 0.3 % keratin fibers added. Looking at their porosity characteristics in table 5.2 it can be seen that pellets E present the highest volume of pores smaller than 10 μm while pellets F and G present the highest volume of pores larger than 20 μm. It seems that this relevant characteristic favored the highest Weibull strength value for pellets E, 35 MPa.

Both pellets E and F have similar grain sizes (14 μm). However because of their porosity characteristics pellets E present a more uniform grain size distribution than pellets F. Pellet F microsections show that closer to the pore clusters the grains are smaller than the farther ones, which is an effect also observed in pellets E but in a smaller proportion. Pellets G presented the previously mentioned bi-modal structure having smaller grains in the pellet central part (3 μm) and larger grains at the pellet borders (12 μm).

Pellets F and G presented quite similar values for Weibull strength respectively 25 MPa and 27 MPa. Pellets E presented the lowest value for the Weibull modulus, 4.1, whereas pellets F and G presented the highest values 5.0 and 4.9 respectively.

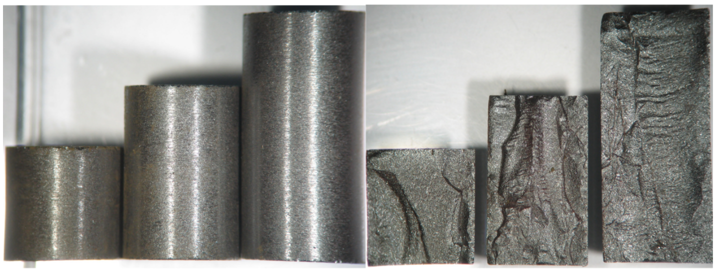

Figure 5.21: $GP2$ sintered pellets H, A and K before and after the brazilian test (left to right).

In $GP2$ pellet types with different lengths and with the same diameter were also produced so it could be observed whether the obtained results with the green pellets ($GP1$) could be transferred to the sintered pellets. Pellets H, A and K are respectively $7.26\,mm$, $10.81\,mm$ and $14.48\,mm$ long (see figure 5.21). Similarly to $GP1$ pellets their initial lengths were $9\,mm$, $13\,mm$, and $18\,mm$ respectively. They had the same green density and were sintered for the same sintering dwell time of 3 hours. The absence of additives produced quite high TD as well as a higher amount of fine porosity in all three pellet types and it also could be observed the absence of porosity in many grains. The amount of larger pores in pellets A is two times higher than in pellets H and K. Pellets H and K have similar grain size, $13.31\,\mu m$ and $14.48\,\mu m$ respectively, while pellets A grain size is smaller $10.81\,\mu m$.

The Weibull modulus increased with the length, i.e., for the longest pellets, K, it was the highest and for the smallest pellets, H, it was the smallest. On the other hand the Weibull strength for pellets K was the smallest, $26\,MPa$, and for pellets A and H it was the same, $32\,MPa$.

The graph in figure 5.22 shows the exponential correlation index between the length of pellets A, H and K and the Weibull modulus. The obtained index means that the Weibull modulus increases with the pellet length.

Finally we come to the pellets $SQ - Std$ and $SQ - Ker$, which were damaged in the squirrel cage and afterwards sintered for 3 hours. These pellets have the same microstructure as the

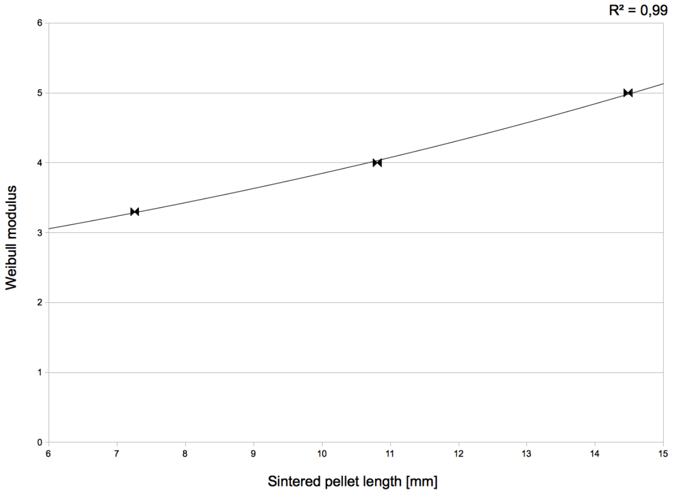

Figure 5.22: Graph showing the exponential correlation between the pellet and the Weibull modulus in sintered pellets.

pellets A and G respectively, i.e., pellets A have a fine porosity with a grain size of $10.81\,\mu m$ and pellets G have a bi-modal grain size distribution and porosity clusters.

Brazilian test results show that the $SQ - Ker$ pellets with their bi-modal structure have a much more expressive Weibull modulus than the standard $SQ - Std$ pellets. This means that the pellets with fibers have a lower scatter in their failure mode, which allows a control of the production process as a whole. On the other hand the Weibull strength for the $SQ - Std$ pellets presented a better result than for the $SQ - Ker$ pellets. The higher value of the Weibull strength for the $SQ - Std$ pellets maybe because of the smaller presence of larger pores than in pellets $SQ - Ker$.

The last group to be analyzed is the $GP3$. The pellets in this group have some of $GP1$ and $GP2$ characteristics such as longer green pellets and the keratin fibers as additive, which were characteristics that presented improvement in the mechanical resistance as a whole. Beyond that, pellets with higher green density and different amounts of keratin fibers were introduced to this group of pellets.

In the first analysis we have pellets B from $GP2$ and pellets N from $GP3$. These two pellet types had the same powder preparation and the same sintering process. Also, small and intermediate pore volumes are similar as well as the TD. The great difference between them is the fact that pellets B are shorter than pellets N.

In the analysis of $GP1$ group we have seen that longer green pellets presented a much higher Weibull modulus, i.e., higher reliability than the shorter ones. The $GP1$ results showed a Weibull modulus at least 30 % higher for pellets with length of $18\,mm$. By comparing pellets B and N it can be seen that the tendency presented by the green pellets can also be observed by the sintered ones. It was for sure not expected that this great improvement presented by the green pellets would be directly transferred to the sintered pellets since it is well known that the sintering process itself could introduce imperfections and flaws to the ceramic pellet microstructure as well as the grinding process after sintering could produce cracks to the pellet surface. The reliability improvement achieved by the sintered pellets was about 10 %. A similar tendency is also observed by comparing pellets G, $10.94\,mm$ in length, and pellets Q, $14.86\,mm$ in length, both with keratin fibers as additive. The longer pellets Q presented a slightly higher Weibull modulus and Weibull strength than pellets G.

For the second analysis we took pellets R and S. Both pellet types had the same green density, $\sim 6.2\,g/cc$, the same green pellet length, $\sim 18\,mm$, and were sintered for the same sintering dwell time 3 hours. However, they differ in the amount of keratin fibers added to the powder mixture. Pellets R had $0.2\,wt\%$ of keratin fibers and pellets S had $0.3\,wt\%$.

The lower amount of additive in pellets R produced pellets with a higher TD, also a greater amount of larger grains and a lower quantity of smaller grains than in pellets S. The smaller grains in the bi-modal structure is a direct consequence of the keratin fiber, which delayed the grain growth. It seems that the smaller grains conferred some stability to the group of pellets allowing them to have a more similar fracture mechanism, which can be seen by their Weibull modulus. Pellets S presented a higher value than pellets R most likely because they presented a higher amount of smaller grains.

The porosity analysis of pellets R and S show that because of the higher volume of additive, pellets S have a larger amount of pores greater than $20\,\mu m$, which most likely negatively influenced on the Weibull strength. Pellets R have a Weibull strength of $34\,MPa$ and pellets S of $31\,MPa$.

The third analysis involves pellets V and X. These pellets have the same green density, $\sim 6.2\,g/cc$, the same green pellet length, $\sim 18\,mm$, and were sintered for the same sintering dwell time 9 hours. Their basic difference is that pellets V have $0.2\,wt\%$ of keratin fibers and pellets X had $0.3\,wt\%$, which produced higher density for pellets V. The influence of the slightly higher porosity volume, because of the higher amount of keratin fibers added, of pellets X can be seen in their lower Weibull strength.

Pellets V presented a greater amount of larger grains than pellets X. The amount of smaller grains is practically the same for both pellet types, which could explain the similar Weibull modulus values obtained, 5.6 for pellets V and 5.5 for pellets X.

In the fourth analysis we take again a pellet type from $GP2$, pellets E, and compare to pellets T. Both of these pellet types have as additive the OS and were sintered for 3 hours. They differ in their green length, pellets E are $\sim 13\,mm$ long and pellets T are $\sim 18\,mm$ long, and in their green density, pellets $E \sim 5.8\,g/cc$ and pellets $T \sim 6.2\,g/cm^3$. The lower green density of pellets E produced pellets with lower TD and consequently higher porosity volume.

The lower porosity volume of pellets T resulted in a higher Weibull strength than pellets E.

The Weibull modulus was more influenced by both pellet length and grain size. The of pellets T being longer and having smaller grains favored their higher reliability.

The fifth analysis is between pellets U and X. These pellet types had the same amount of keratin fibers in their composition, $0.3\,wt\%$, were sintered for the same sintering dwell time, 9 hours, had the same pellet green length but had different green densities, pellets U had $\sim 5.8\,g/cm^3$ and pellets X had $\sim 6.2\,g/cm^3$.

The lower green density of pellets U produced a higher porosity volume than for pellets X. This characteristic determined the higher Weibull strength value for pellets X. On the other hand, the greater amount of smaller grains presented by pellets U conferred a higher reliability to them than for pellets X. Pellets U obtained a Weibull modulus of 6.9 and pellets X a value of 5.5.

The last analysis is between pellets Q and S. Both pellet types had $0.3\,wt\%$ of keratin fibers added to their powder mixtures. They were also sintered for the same sintering time, 3 hours, and had the same pellet green length, $\sim 18\,mm$. However, they differ in their green density, having pellets Q $5.8\,g/cm^3$ and pellets $S \sim 6.2\,g/cm^3$.

The higher density of pellets S produced pellets with a lower porosity volume, which seems to be the determining factor for the better performance of this pellet type when compared to pellets Q. Pellets S had a Weibull strength of $31\,MPa$ and pellets Q had a value of $29\,MPa$.

The Weibull modulus results were influenced by the grain size. Pellets S presented a greater amount of smaller grains than pellets Q, which conferred to pellets S a reliability value of 6.9 and of 5.0 for pellets Q.

In addition to these 3 pellet groups four more groups of pellets, slightly damaged at the squirrel cage, were also sintered and tested. The idea here was to analyze how these pre-damaged pellets would mechanically behave during the test. Some pictures of these pellets can be seen in the section 5.3.

Table 5.6: $Gp1$green pellets results by brazilian test.

Type	Density [g/cm^3]	Mass/unit [g]	Length [mm]	Diameter [mm]	Pellet geometric volume [cm^3]	Weibull Modulus	Weibull Strength [MPa]
D6L9	5.88±0.06	1.57±0.05	9.181±0.334	6.092±0.004	0.27	2.9	1.2
D6L13	5.78±0.07	2.21±0.05	13.120±0.220	6.104±0.015	0.38	3.4	1.1
D6L18	5.75±0.06	3.04±0.04	18.078±0.312	6.103±0.011	0.52	4.4	1.2
D8L9	5.72±0.05	2.69±0.06	9.122±0.234	8.100±0.006	0.47	3.5	1.1
D8L13	5.78±0.06	3.93±0.05	13.166±0.193	8.107±0.009	0.68	4.0	1.3
D8L18	5.77±0.06	5.45±0.11	18.255±0.365	8.119±0.004	0.95	9.7	1.2
D10L9	5.72±0.09	4.72±0.17	9.238±0.330	10.658±0.004	0.82	4.1	1.2
D10L13	5.76±0.02	6.83±0.14	13.278±0.278	10.667±0.003	1.19	6.1	1.2
D8L18	5.76±0.06	9.38±0.14	18.184±0.309	10.672±0.006	1.62	9.7	1.3

[1] Theoretical density to UO_2(10.96 g/cm^3)

Table 5.7: $Gp2$ pellets results by brazilian test.

Type	Additive	Length [mm]	Sint. Isotherm. [min]	TD[1] [%]	Porosity [%]	Weibull Modulus	Weibull Strength [MPa]
A	—	10.81±0.06	180	97.04±0.19	2.96	4.0	32
B	—	10.97±0.11	540	97.44±0.10	2.56	4.5	35
C	—	10.94±0.11	1620	97.97±0.05	2.03	4.9	32
D	AZB	11.09±0.09	180	95.31±0.09	4.69	4.1	32
E	B-U_3O_8	10.78±0.10	180	95.45±0.06	4.55	4.1	35
F	Gr-U_3O_8	10.93±0.08	180	95.85±0.07	4.15	5.0	25

[1] Theoretical density to UO_2(10.96 g/cm^3)

Table 5.8: Continuation of *Gp*2 pellets results by brazilian test.

Type	Additive	Length [mm]	Sint. Isotherm. [min]	TD[1] [%]	Porosity [%]	Weibull Modulus	Weibull Strength [MPa]
G	Keratin ($0.3\,wt\%$)	10.94±0.12	180	95.44±0.12	4.56	4.9	27
H	—	7.26±0.05	180	97.66±0.06	2.34	3.3	32
K	—	14.48±0.11	180	97.65±0.06	2.35	5.0	26
L	AZB	10.84±0.09	180	95.12±0.09	4.88	4.2	31
SQ-Std	—	10.72±0.10	180	97.04±0.09	2.96	4.5	31
SQ-Keratin	Keratin ($0.3\,wt\%$)	10.94±0.08	180	95.78±0.12	4.22	7.5	27

[1] Theoretical density to UO_2(10.96 g/cm^3)

Table 5.9: *Gp*3 pellets results by brazilian test.

Type	Additive	Length [mm]	Sint. Isotherm. [min]	TD[1] [%]	Porosity [%]	Weibull Modulus	Weibull Strength [MPa]
M	—	15.47±0.19	180	98.32±0.03	1.68	4.8	40
N	—	14.74±0.23	540	97.78±0.19	2.22	4.8	35
P	—	15.26±0.06	540	98.55±0.04	1.45	4.8	33
Q	Keratin ($0.3\,wt\%$)	14.86±0.12	180	95.55±0.41	4.45	5.0	29
R	Keratin ($0.2\,wt\%$)	15.12±0.12	180	96.21±0.11	3.79	5.1	34
S	Keratin ($0.3\,wt\%$)	15.25±0.15	180	96.14±0.31	3.86	6.9	31
T	B-U_3O_8	15.54±0.09	180	96.40±0.12	3.60	5.1	39
U	Keratin ($0.3\,wt\%$)	14.82±0.16	540	96.29±0.12	3.71	6.9	24
V	Keratin($0.2\,wt\%$)	15.28±0.16	540	96.97±0.10	3.03	5.6	33
X	Keratin ($0.3\,wt\%$)	15.33±0.15	540	96.60±0.09	3.40	5.5	31

[1] Theoretical density to UO_2(10.96 g/cm^3)

5.3 Squirrel Cage Experiment

The squirrel cage experiment was here introduced for simulating how superficial damages on green pellets would influence on the mechanical resistance of sintered pellets (first analysis) and also for analyzing the green pellet resistance against abrasion (second analysis).

In the first analysis pellets without additives, SQ-Std, and pellets with 0.3% of keratin, SQ-Keratin, were used (see table 4.1). As already shown in section 4.2 the testing machine consist of two cylinders where 7 green pellets were carefully placed and damaged for 20 rotations (80 seconds) with a rotation speed of $15\,rot/min$. The mass was measured before and after the experiment for each pellet group. Afterwards these pellets were sintered for 3 hours and ground for reaching dimension specifications and finally tested at the 'Brazilian' test.

The second one, called durability analysis, the pellets were not sintered afterwards. It intended to investigate the chipping strength / abrasion hardness of green pellets SQ-Std and SQ-Keratin by increasing the number of turns resulting in higher weight loss. A higher strength against damage is an indicative of a better resistance to impacts during the production process.

The experiments were performed at room temperature ($20\,°C$). Similarly to the first analysis 7 green pellets were carefully positioned in the cylinder and turned up to 600 rotations. At 20-50-100-200 and 600 turns the average weight loss of the 7 green pellets was measured.

Table 5.10 presents results from the first analysis, while table 5.11 presents the results from the second analysis.

Table 5.10: Standard and Keratin samples from the first analysis.

Type	SQ-Std. Br-Test 01	SQ-Std. Br-Test 02	SQ-Keratin Br-Test 01	SQ-Keratin Br-Test 02
Initial total mass of 7 pellets [g]	67.31	69.43	67.60	70.04
Pellets Total mass after 20 turns at 15 rpm [g]	66.23	69.15	67.37	69.74
Mass loss in [%]	1.6	0.4	0.3	0.4

From results of the first analysis it can be observed that the developed structure with keratin fibers lost in general less material than the standard ones. The basic reason for this feature can be observed in figure 5.23. It can be seen that the keratin fibers 'stick' together to the powder particles increasing the resistance of the pellet against the abrasion reducing the probability of chips. Figure 5.24 show the two pellet groups before and after the 20 turns. The endface of the standard pellets look much more damaged than pellets with keratin fibers. In figure 5.25 it can

Table 5.11: Standard and Keratin samples from the durability analysis.

Type	SQ-Std durability	SQ-Std Mass loss in [%]	SQ-Keratin durability	SQ-Keratin Mass loss in [%]
Initial total mass of 7 pellets [g]	67,.54	—	67.96	—
Pellets Total mass after 20 turns at 15 rpm [g]	67.03	0.8	67.68	0.4
Pellets Total mass after 50 turns at 15 rpm [g]	65.47	2.3	67.03	1.0
Pellets Total mass after 100 turns at 15 rpm [g]	62.57	4.4	65.03	3.0
Pellets Total mass after 200 turns at 15 rpm [g]	59.7	4.6	62.94	3.2
Pellets Total mass after 600 turns at 15 rpm [g]	56.32	5.7	59.91	4.8

be observed in more detail a circumferential section and an endface of pellets from both groups after the test reveling that the loss of chips or mass by the pellets with the keratin fiber is lower than from those without them.

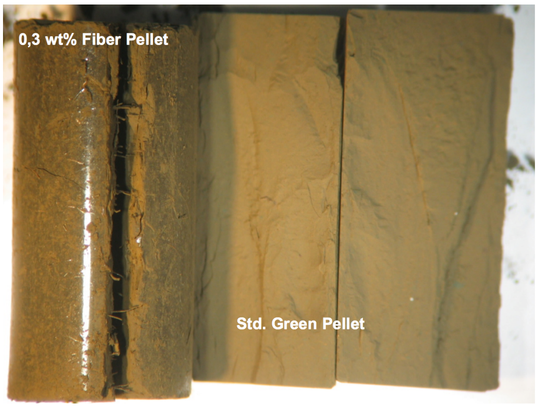

Figure 5.23: On the left a pellet prepared with keratin fibers and on the right side a standard pellet without keratin.

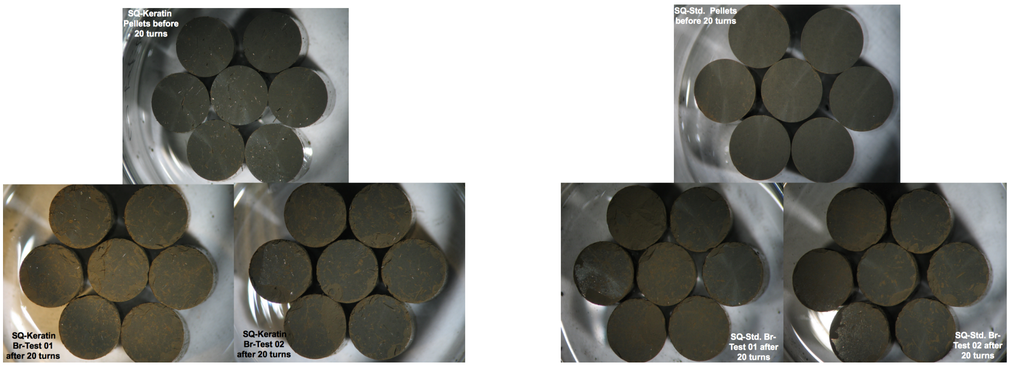

Figure 5.24: Pellets groups before and after the first analysis.

The pellets of the first analysis were sintered after the squirrel cage test. In figure 5.26 it can be seen how some of these pellets look like right after sintering. Every fuel fabricator have their technical standards for determining the allowed chips on the circumference of the pellets. This selection process is either done manually or automatically. In both cases the damages to the endface are much more difficult to be detected as those on the circumference of the pellet. It is true that the chips on the circumference are more critical than the ones on the inside the endface.

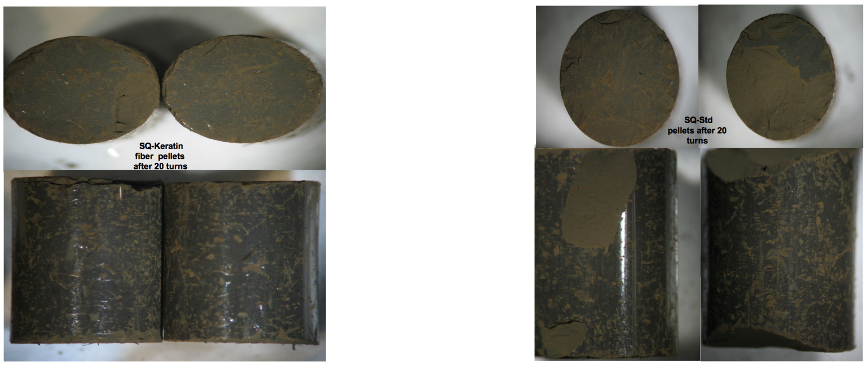

Figure 5.25: Keratin fiber and standard pellets in detail.

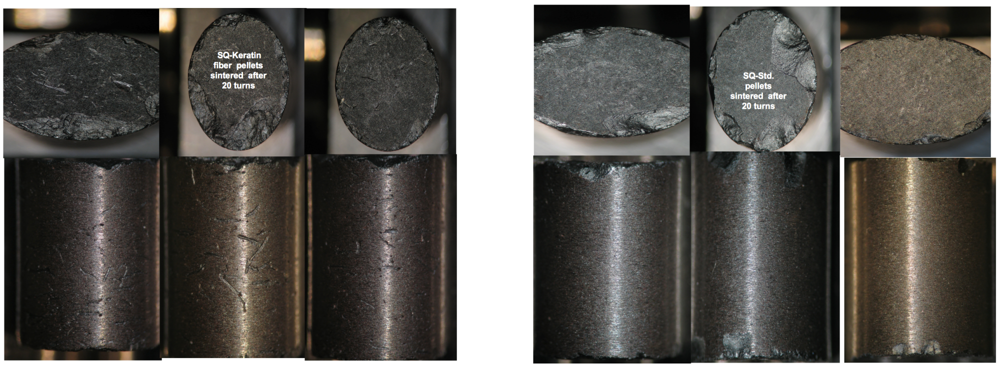

Figure 5.26: Keratin fiber and standard pellets sintered after testing.

Nevertheless any improvement on the production process will ensure a better final quality of the fuel pellets as a whole.

A quite tight standard, used at the present work, from a fuel fabricator states that the chip should be no longer than one third of the pellet length ($L/3$) and have a maximal width of $1.27\,mm$. The quality control is done prior to the fuel rod fulling. However, in this work, the analysis was done in a green pellet of each group having the biggest chips (see figure 5.27) and after sintering them. The chips for the standard pellets are quite bigger in comparison to those in the keratin fiber pellet. Figure 5.28 it is seen that sintered pellets even after their natural volume reduction during sintering still clearly have chips exceeding the standards limits being the chips from the standard pellets much larger than the one from the keratin fiber pellet.

By the second analysis, the durability tests, it can be observed that samples containing the keratin fibers are much more resistant than the standard ones. The percentile weight loss, which

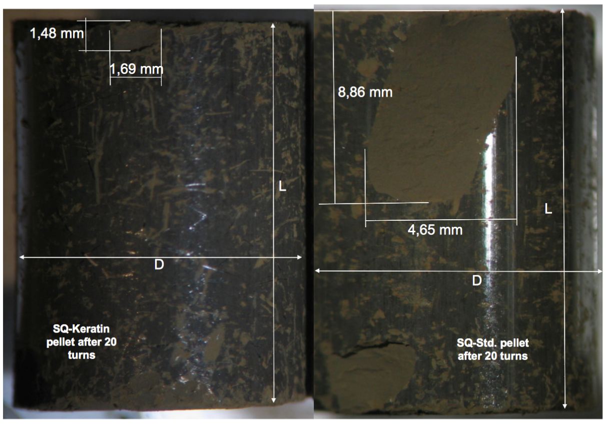

Figure 5.27: Green pellets after 20 turns showing chips dimensions.

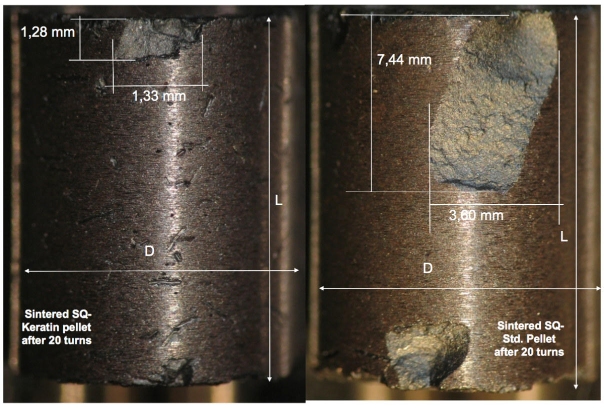

Figure 5.28: Green pellets after 20 turns showing chips dimensions.

is the proportional mass lost after each test step, was calculated after each testing step showing progressively development of the weight loss by the pellets.

In the first test step the pellets, similarly to the procedure in the first analysis, were damaged for 20 turns. The chips produced at this step are usually larger than in the other steps because the pellets still have sharp corners. Similarly to what was happened in the first analysis higher mass loss as well as larger chips were observed by the standard pellets as can be seen in figure 5.29.

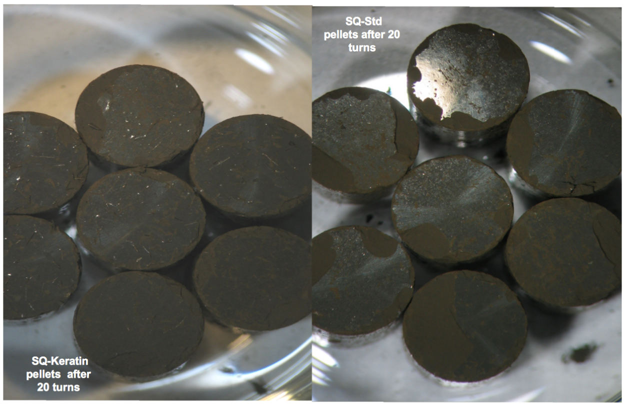

Figure 5.29: Both group of pellets after 20 turns.

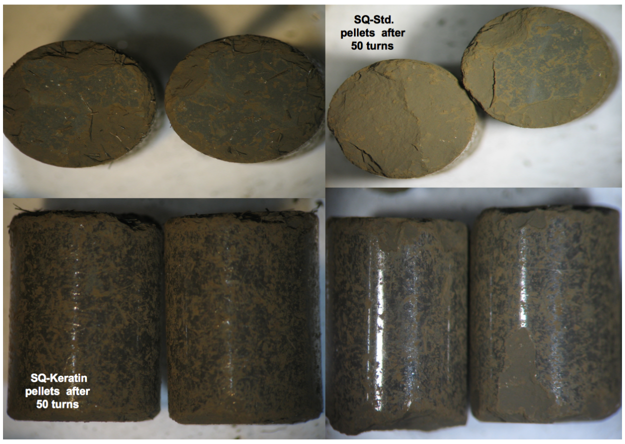

Figure 5.30: Keratin fiber and standard pellets after 50 turns.

At the second testing level the pellets were damaged for 50 turns. Some of the resulting pellets are shown in figure 5.30. Large chips are still found at this level even though they have reduced a bit in size but increased in the total volume. For this reason weight loss more than doubled in comparison to the first level. Here also the pellets containing keratin fibers have lost less mass and presented smaller chips than the standard ones.

The third testing level damaged the pellets for 100 turns. For this testing level no larger chips

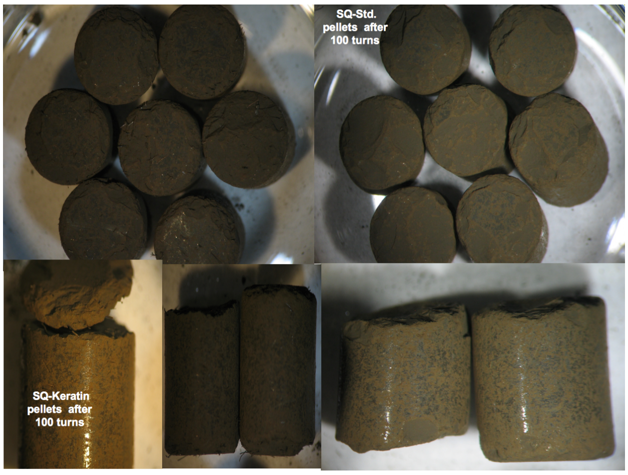

Figure 5.31: Keratin fiber and standard pellets after 100 turns.

were expected since the sharp edges were already abraded however the weight loss for both pellet types quite increased. In fact it almost doubled for the standard pellets and was 3 times higher for the keratin fiber pellets. The reason for this sudden increase was the end-capping of a pellet in both groups (see figure 5.31). As the keratin fiber pellets were less damaged than the standard ones the end-capping chip was also proportionally larger resulting in a higher weight loss increase than the standard ones. Even so the total weight loss of the standard pellets was higher than by the keratin fiber pellets.

At the end of the third phase the pellets are getting slightly rounded.

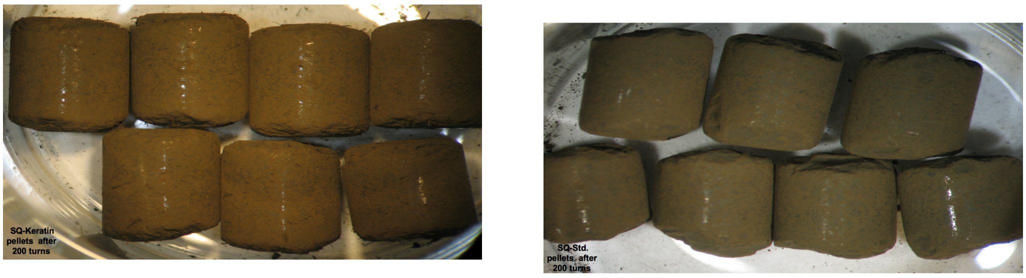

Figure 5.32: Both group of pellets after 200 turn testing.

The fourth testing level damaged the pellets for 200 turns. At the end of this level the pellets become more and more rounded by the abrasion among the other pellets and mainly by the contact to the cage net (see figure 5.32). Standard pellets lose again more mass than the keratin fiber pellets. The weight loss for both types increase in the same proportion than in the last phase.

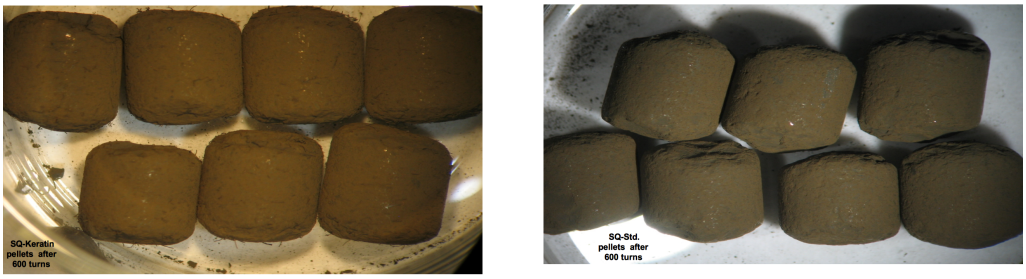

Figure 5.33: Keratin fiber and standard pellets after 600 turn testing.

By the end of the last testing level, which damaged the pellets for 600 turns both types were quite rounded (see figure 5.33). The mass loss for the standard pellets increased more than for the keratin fiber pellets.

5.4 Indentation Test

With the micro-indentation test two characteristics of the ceramic fuel, the hardness and the toughness, can be determined as mentioned in section 4.3. The test was just applied for the $GP3$ pellets.

Before jumping to the obtained results it is important for their interpretation and understanding that some theoretical explanation be given.

The Griffith theory is extensively discussed in Wachtman et al [5] (see also subsection 2.2). Among others it is explained that in the Griffith theory a crack will be stable under the application of a uniform stress and will heal for smaller stress values as well as when the stress is removed. However, this stable crack propagation under the conceptual framework of the Griffith theory can just happen in adequate circumstances:

1. Materials with a constant critical stress intensity factor. Combinations of specimen geometry and details of load application leading to a decreasing of the stress intensity factor as the crack increases. This is the basis for methods of creating a controlled crack.

2. In materials that have a not constant critical stress intensity factor, which increases faster than the applied stress stress intensity factor as the crack elongates. These materials show the R-curve behavior.

Obtained results of the present work fit to the first exception of the Griffith theory, i.e. with the decrease of the critical stress intensity factor (K_{Ic}) there will be an increase of the crack length.

For the determination of the pellet group properties in table 5.13 the pellet groups indentation characteristics after the indentation test needed to be determined. Figure 5.36 presents a microindentation imprint where the crack length (c) and the diagonal imprint (d) are presented. It is important to mention that the diagonal imprints were performed in the central part of the pellets. At least two, in most of the cases at least three, microindentation imprint were used for the determination of constants. In table 5.12 the measured constants diagonal imprint and crack length are presented. Unfortunately, for the standard pellets M and N it was not possible to determine the crack length, which also did not allow the determination of the fracture toughness.

From the measured constants in table 5.12 we can observe that the diagonal imprints of the pellets prepared with keratin fibers are smaller than the ones from standard pellets. In addition to that the crack length of the standard pellet N is greater than the crack length from the keratin fiber pellets. A larger diagonal imprint means that the Vickers pyramid penetration depth is greater in the standard pellets than in the keratin fiber ones. The deeper penetration consequently lead to a larger crack length.

The graphic in figure 5.34 shows the correlation between the diagonal imprint and the crack length. Due to the difficulty in measuring the exact crack length, some scatter in data was observed. Even though a reasonable dependence was obtained. A linear correlation factor of $R^2 = 0.68$ was obtained.

Another graphic is presented in figure 5.35 showing the correlation between the pellet porosity and the crack length. The obtained linear correlation factor of $R^2 = 0.84$ indicates that there is a good interdependence between these two factors in the analyzed data.

With the measured constants it was possible to calculate the fracture properties for each pellet type. Equations for calculations of the hardness and critical stress intensity factor can be found in subsection 2.2. The property fracture surface energy was here introduced and can be calculated by equation 5.1. Similarly to the fracture toughness the surface energy can also be used to predict the mechanical behavior of fuel pellets with reported values varying from 0.4 to $8\,J\,m^{-2}$ [139]. The surface energy depending on the sample temperature was already presented in chapter 2. However, the one here presented as a function of the toughness was reported by Matzke et al [140]. The Young's modulus as a function of porosity (E_p) for uranium dioxide was reported by [141], whereas the Poisson's ratio for uranium dioxide as a function of the porosity

Table 5.12: GP3 pellets indentation test characteristics.

Type	Additive	Diagonal imprint [μm]	Crack length [μm]
M	—	71.25	—
N	—	71.25	102.1
P	—	74.17	—
Q	Keratin (0.3 $wt\%$)	62.92	88.1
R	Keratin (0.2 $wt\%$)	70.00	95.8
S	Keratin (0.3 $wt\%$)	66.67	88.9
T	B-U_3O_8	70.00	93.3
U	Keratin (0.3 $wt\%$)	67.92	91.7
V	Keratin (0.2 $wt\%$)	70.42	97.2
X	Keratin (0.3 $wt\%$)	67.50	95.8

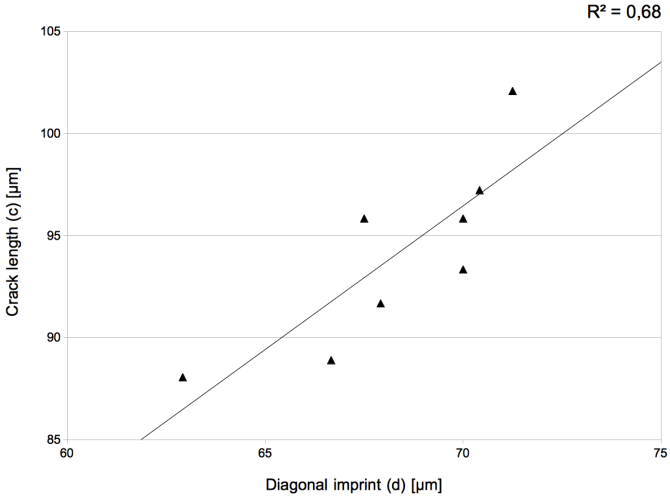

Figure 5.34: Graphic showing the linear correlation between the diagonal imprint (d) and the crack length (c).

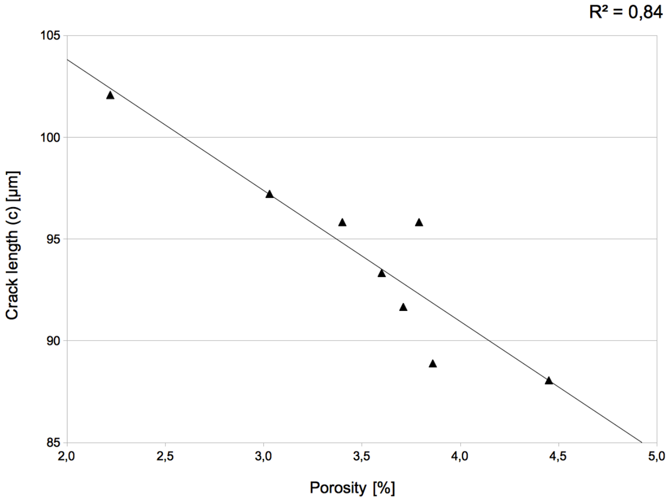

Figure 5.35: Graphic presenting the linear interdependence between the pellet porosity and the crack length (c).

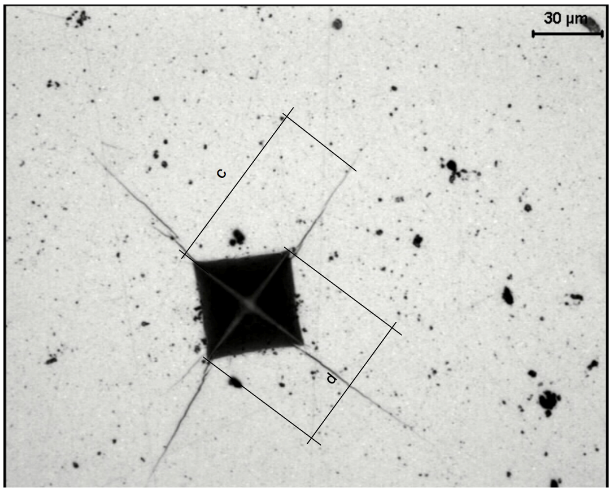

Figure 5.36: Microindentation imprint showing the crack length (c) and the diagonal imprint (d).

fraction (ν_p) was presented by [142]. For the calculation of these constants equations 5.2 and 5.3 were used, where E_0 is the Young's modulus of nonporous polycrystalline UO_2 ($224\,GPa$) and ν_0 is the Poisson's ratio for nonporous polycrystalline UO_2 (0.32).

$$\gamma_s = \frac{(1-\nu_p^2)}{2E_p}(K_{Ic})^2 \tag{5.1}$$

$$E_p = E_0 - 514p \tag{5.2}$$

$$\nu_p = \nu_0 - 0.34p \tag{5.3}$$

In ceramic technology hardness can be defined as the material resistance to a deformation, which can be permanent or not. The fracture toughness, on the other hand, can be defined as the ability of a material to resist crack propagation. A higher hardness and a higher toughness are quite desired in ceramics.

The summarized results are presented in table 5.13. The calculated hardness for the standard pellets is slightly lower when compared to the values obtained by the pellets with keratin fibers. Also the pellets containing OS when compared to the keratin fibers pellets have in most of the cases a lower hardness. These results clearly reflex the characteristics in table 5.12.

The calculated fracture toughness and fracture surface energy values in table 5.13 show also a better mechanical behavior for the keratin fiber pellets than for the standard pellets. Pellets with OS presented better values than some types of pellets with keratin fibers.

It was said above that the diagonal imprints were preformed in the central part of the pellets. The keratin fiber pellets have the bi-modal microstructure having larger grains at the pellets borders and smaller grains in its central part. The other pellet types presented a more uniform grain size distribution all over the pellet matrix. The average grain size in this central part of the keratin fiber pellets varied from 3 to 6 μm, while in the other pellet types it varied from 12 to 22 μm. It was already reported elsewhere [143, 43, 144] that materials with smaller grain sizes present a higher plasticity than those with larger grains. For sure the porosity influence on the fracture toughness, however the difference in grain size among the tested pellet types was also a great influencing factor to the fracture properties.

The fracture toughness interdependence to crack length was presented in figure 5.37. The obtained linear correlation factor $R^2 = 0.76$ shows the reported data is in good agreement to the first exception of the Griffith theory for a stable crack propagation.

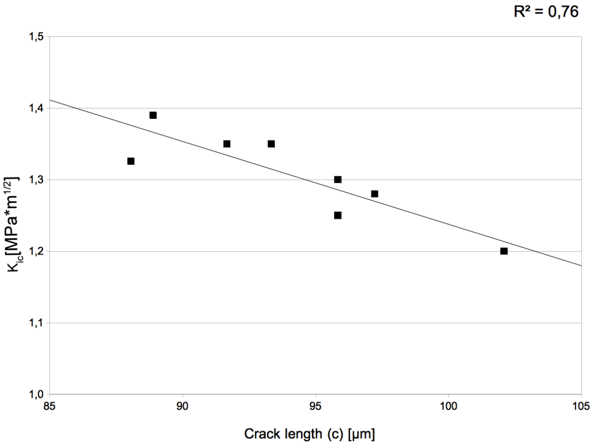

Figure 5.37: Graphic showing the linear correlation between the diagonal imprint (d) and the crack length (c).

Table 5.13: GP3 pellets fracture properties.

Type	Additive	Hardness $[MPa]$	Fracture toughness (K_{Ic}) $\left[MPa * m^{1/2}\right]$	Surface energy (γ_s) $[J/m^2]$
M	—	37.26	—	—
N	—	37.26	1.20	2.71
P	—	34.39	—	—
Q	Keratin $(0.3\,wt\%)$	47.78	1.33	3.56
R	Keratin $(0.2\,wt\%)$	38.60	1.30	3.20
S	Keratin $(0.3\,wt\%)$	42.56	1.39	4.13
T	B-U_3O_8	38.60	1.35	4.40
U	Keratin $(0.3\,wt\%)$	41.01	1.35	4.22
V	Keratin $(0.2\,wt\%)$	38.15	1.28	2.77
X	Keratin $(0.3\,wt\%)$	41.51	1.25	2.53

5.5 Creep Behavior

In chapter 2 the creep behavior was first introduced. It was explained that the yield strength of the material is not overcome by the testing stresses, which are applied for long periods of time for producing strains.

Sample characteristics prior testing were presented in section 4.4. General characteristics such as the creep rate and the stress exponent are presented for all samples in figure 5.38 and table 5.14. Pictures of the keratin fiber samples after creep are presented in figures 5.39 and 5.40.

A higher creep rate means that the analyzed material is more prone to deform permanently. The most important part of the creep deformation is concentrated at the secondary or stationary creep step. At this stage the creep rate is determined as can be shown in the graphic of figure 5.38. From these results we can determine the stress exponent, which is determined from the curve power law variation. With this constant it is possible to determine the creep mechanism acting at lower and higher stresses.

From the first two stresses of each tested sample it was determined the stress exponent for lower stresses. As example we can use the calculation of the stress exponent for the UO_2-keratin fiber pellet. From the straight line between $15\,MPa$ and $30\,MPa$ we have determined n from the equation $\dot{\varepsilon} = \sigma^n$. In the case of the higher stresses the stress exponent was determined from the straight line between the second stress value and the highest one. Using again the UO_2-keratin fiber as example we determine n from the straight line between $30\,MPa$ and $90\,MPa$.

In table 5.14 the stress exponents are presented. UO_2-keratin fiber and standard pellets have the same creep mechanism, grain boundary diffusion (Coble creep type). Pellets with $30\,\%\,OP$ present a value slightly lower than the unit, which means that the temperature has a greater influence on the creep behavior than the applied stress [45, 138]. Pellets with chromium oxide presented the same creep mechanism, which is a characteristic of pellets with this type of additive. At higher stresses the creep mechanism presented for all pellet types was the dislocational creep.

The creep rate can now be analyzed. The displayed results in the graphic from figure 5.38 show that pellets with $30\,\%\,OP$ present the highest creep rate at lower stresses. The other two pellet types containing the additives keratin fibers and chromium oxide in their previous fabrication process present a similar behavior, which is a better behavior than the standard pellets.

The pellets with $30\,\%\,OP$ are those with smallest grain size (2μ). On the other hand keratin fiber pellets with their bi-modal microstructure presented a better behavior than the standard pellets and a similar creep rate when compared to the chromium oxide pellets, which have the largest grain size. Among the pellets prepared with additives the comparison clearly shows that under low stresses pellets with smaller grains have a better creep rate. For sure the additives previously added to the fuel contribute to the creep behavior, however the determining factor at our analysis was the pellet grain size.

Table 5.14: Creep samples stress exponent at lower and at higher stresses.

Stress type	Stress exponent			
	UO_2 + Keratin fibers	Std. UO_2*	UO_2 + Cr_2O_3*	UO_2 + U_3O_8**
Low stresses	1.58	1.95	3.45	0.86
High stresses	3.84	4.91	2.31	3.23

* Courtesy AREVA NP GmbH
** Vidal [138]

By increasing the applied stresses we observe an improvement of the creep rate of the pellets with chromium oxide and keratin fiber by even slightly overcoming the pellets with $30\,\%\,OP$ at the highest applied stress ($90\,MPa$). It is important to mention that at the extreme severe environment in a nuclear reactor at elevated temperatures (the fuel reaches about $2000\,°C$ at its central part during the reactor operation) and long periods of operation at higher burnup a higher creep behavior is desired.

At higher stresses we see that the pellet with additives converge to a similar creep rate values. The standard one substantially increase its creep rate, however it is still about 40 % lower than by keratin fiber pellets, the highest one. The explanation for this behavior can not be explained with the grain size alone. In this case the additive type and concentration need to be taken into consideration. However, since the creep test at the present work was used for understanding and determine the creep mechanism at the UO_2-keratin fiber pellets as well as for showing that the creep behavior of theses pellets is comparable to other pellet types, no further analysis will be done.

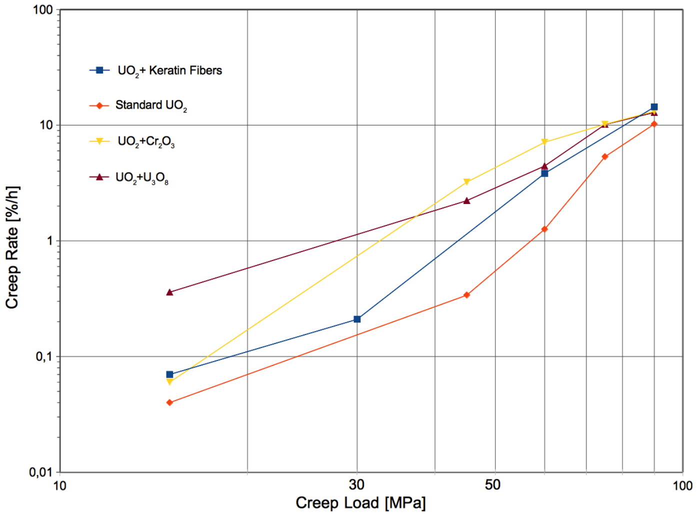

Figure 5.38: Creep load vs. creep rate from different types of UO_2 fuel.

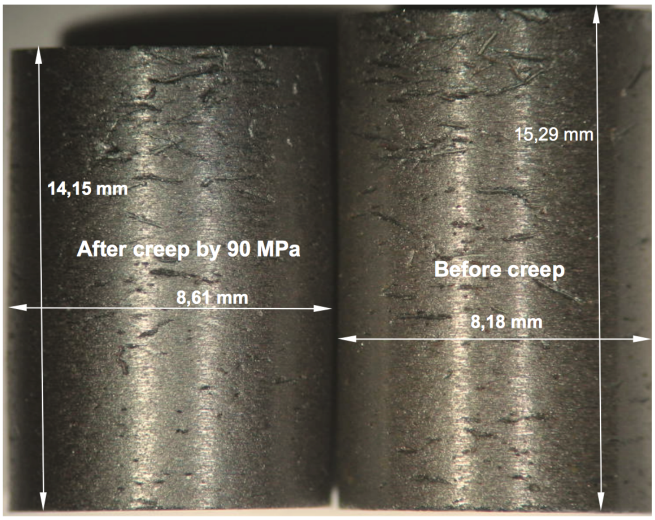

Figure 5.39: UO_2-keratin fiber samples before and after test by $90\,MPa$. It is easily observed a strong reduction in length and an increase of the pellet diameter.

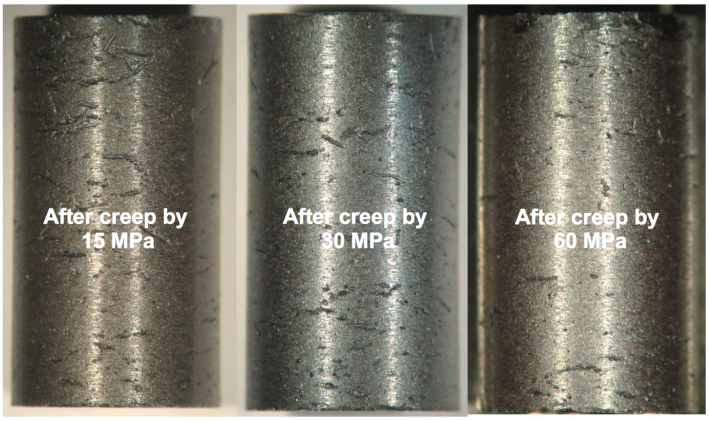

Figure 5.40: UO_2-keratin fiber samples before after test by $15\,MPa$, $30\,MPa$ and $60\,MPa$ respectively. At the first two pellets a light reduction in length and an increase in diameter was measured, whereas by the last one the diameter increased 2.7 % and the length reduced 4.1 %.

Chapter 6

Conclusions

6.1 General conclusions

The ceramic nuclear fuel fabrication is a complex process, which involves several production steps. These steps were extensively studied, analyzed and detailed in the present work. The objective of such investigation was to understand and analyze the influence of the variation of the production process steps on the microstructure and consequently on the mechanical strength of the nuclear fuel pellet. Moreover, an improvement of the qualitative characteristics of the ceramic fuel pellets was also aimed. This was reached by means of elevating the pellets reliability and mechanical resistance through the introduction of a new fuel additive.

These objectives were reached by using the keratin fibers as a new fuel additive. It has proved its efficiency by considerably improving the reliability of both green and sintered UO_2 pellets. In addition to that it also proportionated an increment on the mechanical resistance of the green pellets.

6.2 Microstructure analysis

The final pellet microstructure is defined by a series of influencing factors such as the presence of additives in the powder mixture, the pressing green density and the powder mixing process. The sintering temperature, sintering dwell time and sintering atmosphere also bring influence to the final microstructure, however just the influence of the sintering dwell time was analyzed at this work.

From the additives added to the UO_2 powder the UO_2 oxidized powder (OP) was the one with the biggest particle, about $79\,\mu m$, due to their easy particle agglomeration. The other additives presented finer particles bellow $10\,\mu m$.

Pellets D and L were prepared with the same additive AZB. The AZB was added to pellets

D at the blending step while by pellets L it was added after the granulation step. This slight change in the production process developed two different microstructures. Pellets L presented larger grains than pellets D, larger pores, porosity free grains and a granulate structure instead of a homogeneous one.

Pellets E and F were respectively prepared with oxidized pellet scrap (OS) and oxidized powder (OP). The particles forming the OS are hard and fine, whereas the OP particles are softer and easy to agglomerate. Because of these additive particle characteristics, pellets with OS present fine porosity distributed all over the pellet matrix with some porosity clusters whereas pellets containing OP show in its matrix porosity agglomerated in form of hooks. As for the grain size, a more uniform grain size distribution can be observed in pellets E than in F. In pellets F microsections it can be observed that the grains closer to the porosity clusters are smaller than the farther ones. In both pellet types the grain size is similar since they had the same green density and were sintered for the same sintering dwell time of 3 hours.

Pellets T have the same additive type as pellets E, and were pressed with a higher green density, which is the main factor reducing their final porosity. The grain size remained practically the same since their sintering dwell time was the same.

Pellets G, Q, R, S, U, V and X had as additive keratin fibers. The variations in the amount of keratin fibers added, sintering dwell time and green density resulted indeed in different microstructures. Nevertheless, some common characteristics among them were observed such as the presence of elongated pores, porosity clusters and larger grains located at the pellet borders while the smaller ones were concentrated more in the central part of the pellet. This distribution of grains was identified as bi-modal structure. A higher amount of additive resulted in a lower porosity volume, and consequently in a higher TD, and in a smaller grain size. A higher green density produced larger grains and a lower porosity volume. A longer sintering dwell time produced larger grains and a higher TD.

Pellets A, B, C, H, K, M, N and P are the standard samples, i.e., no additive was added to their microstructure. Because of the absence of additives the final TD of these pellets was much higher than by those with additives. The higher density also resulted in smaller and finer pores and in some cases, for instance in pellets N and P, the presence of porosity free grains was observed. In addition to that, another common characteristic of these pellets is the presence of spherical pores. The grain size varied according to the sintering dwell time, i.e., a higher dwell time produced larger grains.

6.3 Strength Tests

The squirrel cage, together with the diametral compression test, were the experiments used for analyzing the mechanical strength of the not sintered UO_2 pellets.

Standard and UO_2-keratin fiber pellets were positioned in the squirrel cage and rotated. By the end of each test step the pellets were externally analyzed and weighted. From these analysis we have obtained that pellets with keratin fibers were much more mechanically resistant than the standard ones.

The diametral compression test was used for evaluating the influence of the L/D ratio influence, of the different additives mixed to the UO_2 powder and the different pellet production processes on the mechanical strength of the pellets. In the $GP1$ pellet group the L/D ratio influence was analyzed. In the $GP2$ and $GP3$ the different additives and production processes were studied.

$GP1$ results show that if one fixes the pellet diameter and increase the pellet length the Weibull modulus will also increase. Another interesting observation is that the maximal Weibull modulus is reached for the largest volume of each reference diameter tested. Hence, the obtained values for $D10L13$ and $D10L18$ are very expressive (Weibull modulus = 9.7) if it is considered that ceramics with a Weibull modulus between 10 and 20 are considered ceramics of good quality.

The great contribution of the fibers to the green pellet structure was the fact that they helped to keep the particles together minimizing the damage coming from the inherent contact or chock among pellets.

In the $GP2$ the standard pellets A, B and C, which were sintered for 3, 9 and 27 hours respectively, presented a quite low porosity volume having a higher amount of pores smaller than $10\,\mu m$. Pellets A with the shortest sintering dwell time and the highest amount of pores larger than $20\,\mu m$ presented the lowest Weibull modulus and the lowest Weibull strength. From the comparison of these experiments results we can conclude that by increasing the TD there will be an improvement of the Weibull modulus and strength.

Pellets E had OS as additive, pellets F were prepared with OP as additive and pellets G had the 0.3 % keratin fibers added. Pellets E present the highest volume of pores smaller than $10\,\mu m$ while pellets F and G present the highest volume of pores larger than $20\,\mu m$. It seems that this relevant characteristic favored to the highest Weibull strength value for pellets E, $35\,MPa$. On the other hand, pellets F and G presented quite similar values in Weibull strength respectively $25\,MPa$ and $27\,MPa$. Pellets E presented the lowest value for the Weibull modulus, 4.1, whereas pellets F and G presented the highest values 5.0 and 4.9 respectively.

Sintered pellets with different lengths were also analyzed. Pellets H, A and K were respectively $7.26\,mm$, $10.81\,mm$ and $14.48\,mm$ long and their production process was same. The Weibull modulus increased with the length, i.e., for the longest pellets, K, it was the highest and for the smallest pellets, H, it was the smallest. However, the Weibull strength for the pellets K was the smallest, $26\,MPa$, whereas for pellets A and H it was the same, $32\,MPa$. Most likely the smaller grain size from pellets A and H favored to their higher Weibull strength value. We also can conclude that the longer pellets are more reliable than the shorter ones.

Pellets $SQ - Std$ and $SQ - Ker$, which were damaged in the squirrel cage and afterwards sintered for 3 hours, were also tested with the diametral compression test. The test results show that the $SQ - Ker$ pellets with their bi-modal structure have a much more expressive Weibull modulus than the standard $SQ - Std$ pellets. This means that the pellets with fibers have a lower scatter in their failure mode, which allows a control of the production process as a whole. On the other hand the Weibull strength for the $SQ - Std$ pellets presented a better result than for the $SQ - Ker$ pellets. The higher value of the Weibull strength for the $SQ - Std$ pellets maybe because of the smaller presence of larger pores than in pellets $SQ - Ker$.

The $GP3$ contained most of the UO_2 keratin fiber pellets. These pellets differ among them in their green density, in the amount of additive added to their powder mixture and in the sintering dwell time.

Pellets R and S having the same green density and sintered for the same sintering dwell time differ in the amount of additive added to their powder mixture. Pellets R had $0.2\,wt\%$ of keratin fibers and pellets S had $0.3\,wt\%$. The lower amount of additive in pellets R produced pellets with a higher TD, also a greater amount of larger grains and a lower quantity of smaller grains than in pellets S. The smaller grains in the bi-modal structure is a direct consequence of the keratin fiber, which delayed the grain growth. It seems that the smaller grains conferred some stability to the group of pellets allowing them to have a more similar fracture mechanism, which can be seen by their Weibull modulus values. Pellets S presented a higher value than pellets R most likely because they presented a higher amount of smaller grains.

The porosity analysis of pellets R and S show that because of the higher volume of additive, pellets S have a larger amount of pores greater than $20\,\mu m$, which most likely negatively influenced on the Weibull strength. Pellets R have a Weibull strength of $34\,MPa$ and pellets S of $31\,MPa$.

The comparison between pellets V and X is similar to the last one. The difference between them is the fact that pellets V and X were sintered for 9 hours. Pellets V have $0.2\,wt\%$ of keratin fibers and pellets X had $0.3\,wt\%$, which produced higher density for pellets V. The influence of the slightly higher porosity volume, because of the higher amount of keratin fibers added, of pellets X can be seen in their lower Weibull strength.

Pellets V presented a greater amount of larger grains than pellets X. The amount of smaller grains is practically the same for both pellet types, which could explain the similar Weibull modulus values obtained, 5.6 for pellets V and 5.5 for pellets X.

Pellets U and X differ in their green densities, pellets U had $\sim 5.8\,g/cm^3$ and pellets X had

$\sim 6.2\, g/cm^3$. This lower green density of pellets U produced a higher porosity volume than in pellets X. This characteristic determined the higher Weibull strength value for pellets X. On the other hand, the greater amount of smaller grains presented by pellets U conferred a higher reliability to them than for pellets X. Pellets U obtained a Weibull modulus of 6.9 and pellets X a value of 5.5.

Both pellets Q and S had the same keratin fiber amount, $0.3\, wt\%$, added to their powder mixtures. They were also sintered for the same sintering time, 3 hours, however pellets Q had a green density of $5.8\, g/cm^3$and pellets S had $\sim 6.2\, g/cm^3$.

The higher density of pellets S produced pellets with a lower porosity volume, which seems to be the determining factor for the better performance of this pellet type when compared to pellets Q. Pellets S had a Weibull strength of $31\, MPa$ and pellets Q had a value of $29\, MPa$.

The Weibull modulus results were influenced by the grain size. Pellets S presented a greater amount of smaller grains than pellets Q, which conferred them a reliability value of 6.9 and 5.0 for pellets Q.

The indentation test was performed on the $GP3$ samples. The results showed that the calculated hardness for the standard pellets is slightly lower when compared to the values obtained by the pellets with keratin fibers. Also the pellets containing OS when compared to the keratin fibers pellets have in most of the cases a lower hardness. The calculated fracture toughness and fracture surface energy values show also a better mechanical behavior for the keratin fiber pellets than by the standard pellets. The pellets with OS, however presented better values than some types of pellets with keratin fibers.

The creep test in the present work was used for understanding and determining the creep mechanism in the UO_2-keratin fiber pellets as well as for showing that their creep behavior is comparable to other pellet types.

Pellets with $30\,\%\, OP$, which had the smallest grain size, presented the highest creep rate at lower stresses. The other two pellet types containing as additive keratin fibers and chromium oxide in their previous fabrication process present a similar behavior, which is a better behavior than the standard pellets. Among the pellets prepared with additives the comparison clearly showed that under lower stresses pellets with smaller grains have a better creep rate. For sure the additives previously added to the fuel contribute to the creep behavior, however the determining factor at our analysis was the pellet grain size.

By increasing the applied stresses we observe an improvement of the creep rate of the pellets with chromium oxide and keratin fiber even slightly overcoming the pellets with $30\,\%\, OP$ at the highest applied stress ($90\, MPa$). It is important to mention that at the extreme severe environment in a nuclear reactor at elevated temperatures (the fuel reaches about $2000\,^{\circ}C$ at its central part during the reactor operation) and long periods of operation at higher burnup a higher creep behavior is desired.

6.4 Future Developments

The introduction of the keratin fibers as additive brought some contributions to the pellet strength and reliability. As future development works the following activities could be performed:

- Further improvements at the fiber type would certainly help at the after sintering fuel microstructure. The used keratin fiber was complete eliminated during sintering just by $1500°C$ and left behind ash formed by carbon, hydrocarbons and by inorganic compounds present in the fibers. Reducing the eliminating temperature and the final ash content would be very beneficial to the pellet microstructure.
- The study of the L/D influence on the pellet reliability showed that for the green pellets this ratio had a great impact. Such study and fuel development should be also done for the sintered pellets.
- The green pellet strength was quite improved with the keratin fibers. However, the extra porosity introduced to the pellet microstructure (due to the keratin fibers) also brought some drawback to the mechanical strength of the sintered pellets. A fine tuning of the additive amount added to the powder mixture would bring benefits to the pellet strength.
- Using the keratin fibers as both particle binder and die lubricant could be a solution for reducing the overall additive content in the powder mixture.

Bibliography

[1] Nuclear Fuel Indutries. Nuclear fuel cycle schematic.

[2] D. Menesier H. Bailly and C. Prunier. *The Nuclear Fuel of Pressurized Water Reactors and Fast Neutron Reactors: Design and Behavior*. Intercept Ltd, 1999.

[3] S.G. Popov et al. Thermophysical properties of mox and uo_2 fuels including the effects of irradiation. Technical Report ORNL/TM-2000/351, OAK RIDGE NATIONAL LABORATORY, 2000.

[4] M.W. Barsoum. *Fundamentals of ceramics*. Inst Of Physics Pub, 2003.

[5] W.R. Cannon J.B. Wachtman and M.J. Matthewson. *Mechanical properties of ceramics*. Wiley, 2nd edition, 2009.

[6] W.D. Pilykey. *Peterson's Stress Concentration Factors*. Wiley-Interscience, 2nd edition, 1997.

[7] R.W. Rice. *Mechanical properties of ceramics and composities: Grain and particle effects*. Marcel Dekker Inc, 2000.

[8] C. Barry Carter and M. Grant Norton. *Ceramic materials: Science and engineering*. Springer Verlag, Berlin, 2007.

[9] W.G. Keith R. A.-Kenari J.C. Colter, D.B. James. Process for producing uranium oxide rich compositions from uranium hexafluoride using fluid injection into the reaction zone, June 1977.

[10] Oxford Science Publications. *The Nuclear Fuel Cycle: From Ore to Waste*. OUP Oxford, 1996.

[11] I.E. Knudsen. Production of uranium dioxide, April 1977.

[12] M. Zemek. *Influence of the Conversion of UF_6 to UO_2 powder and its preparation on quality of UO_2 fuel pellets*. PhD thesis, Bratislava Technical University, February 2003.

[13] H. Unkel. The mechanism of the pressing of metal powders. *Arch. Eisenhuttenw.*, 7:161–167, 1945.

[14] R.A. Thompson. Mechanics of powder pressing: I, model for powder densification. *American Ceramic Society*, 60(2):237–243, 1981.

[15] Höganäs. Handbook for sintered components. Technical report, Höganäs, 2011.

[16] T.J. Gray. Sintering of zinc oxide. *Journal of American Ceramic Society*, 37(11):534–538, 1954.

[17] R.M. German. *Sintering theory and practice.* John Wiley and Sons, 1996.

[18] R. L. Coble. Sintering crystalline solids. i. intermediate and final state diffusion models. *Journal of Applied Physics*, 32(5):787–792, May 1961.

[19] M.F Ashby. A first report on sintering diagrams. *Acta Metallurgica*, 22(3):275 – 289, 1974.

[20] Powder metal sintering. Technical report, ASM Desk Edition online, 2008.

[21] J.-F. Baumard C. Salle Y. Rabinovitch R. Boulesteix, A. Maitre. Mechanism of the liquid-phase sintering for nd:yag ceramics. *Optical Materials*, 31(5):711 – 715, 2009.

[22] J. Vidal. Particle size distributions by dry laser diffraction method of uranium oxide powders and additives. Master's thesis, Faculté des Sciences et Techniques de Limoges, 2009.

[23] Fluorite crystal structure, June 2011.

[24] M. K. Fahad. Stresses and failure in the diametral compression test. *Journal of Materials Science*, pages 3723–3729, 1996.

[25] Vickers hardness test, May 2011.

[26] T. Fett D. Munz. *Ceramics: Mechanical properties, failure behaviour, materials selection.* Springer, 2001.

[27] J.S. Hirshhorn. *Introduction to powder metallurgy.* American Powder Metllurgy Institute, 1969.

[28] World Nuclear Association. Nuclear power in the usa.

[29] J. Fachinger. Nuclear fuel cycle. Class notes, 2006.

[30] H. Moon M. Billaux. Pellet cladding mechanical interaction in boiling water reactors. *Nuclear Science, Seminar Proceedings, Aix-en-Provence, France 9-11 March 2004.*

[31] D.R. Uhlmann W.D. Kingery, H.K. Bowen. *Introduction to Ceramics.* John Wiley, 1976.

[32] S. Somiya. *Advanced Technical Ceramics.* Academic Press Inc, 1989.

[33] M.N. Rahaman. *Ceramic Porcessing and Sintering.* Marcel Dekker Inc, 1 edition, 1995.

[34] N. Ichinose. *Introduction to Fine Ceramics: Applications in Engineering.* John Wiley and Sons, 1987.

[35] Y.S. Touloukian et al. *Thermophysical properties of matter - thermal conductivity*, volume 2. IFI/Plenum, 1970.

[36] H. Assmann et al. The behavior of uranium oxide fuels in nuclear reactors. In K.-C. Buschbeck et al, editor, *Gmelin Handbook of Inorganic Chemistry*, volume A4. Springer Verlag, Berlin, 1982.

[37] R. Peierls. Zur kinetischen theorie der wärmeleitung in kristallen. *Annalen der Physik*, 5(3):1055–1101, 1929.

[38] J. K. Fink. Thermophysical properties of uranium dioxide. *Journal of Nuclear Materials*, (279):1–18, 2000.

[39] C. Ronchi et al. *Nucl. Sci. Eng.*, 113(1), 1993.

[40] C. Ronchi et al. *Journal of Applied Physics*, 85(776), 1999.

[41] P.G. Lucuta et al. *Journal of Nuclear Materials*, 223(51), 1995.

[42] J.A. Pask A.E. Gorum, E.R. Parker. Effect of surface condition on room temperature ductility of ionic crystals. *Journal Am Ceramic Society*, 41(5):161–164, 1958.

[43] A.E. Conti P.E. Bohaboy, R.R. Asamoto. Compressive creep characteristics of stoichiometric uranium dioxide. Technical Report GEAP-10054, General Electric, 1969.

[44] D.W. Richerson. *Modern ceramic engineering: Properties, processing, and use in design.* CRC Press, 2005.

[45] G.L. Reynolds B. Burton. Creep process in uranium dioxide. Technical report, CEGB, Berkeley Nuclear Laboratories.

[46] R. W. Rice. Relation of tensile strength-porosity effects in ceramics to porosity dependence of young's modulus and fracture energy, porosity character and grain size. *Materials Science and Engineering*, A 112:215–224, 1989.

[47] A. Brückner-Foit und T. Fett. Discrimination of multiaxiality criteria with the brazilian disc test. *European Ceramic*, pages 689 – 696, November 1995.

[48] S.C. Carniglia. Petch relation in single-phase oxides ceramics. *Journal of American Ceramic Society*, 48(11):580–583, 1965.

[49] S.C. Carniglia. Reexamination of experimental strength-vs-grain-size data for ceramics. *Journal of American Ceramic Society*, 55(5):243–249, 1972.

[50] I.J. McColm. *Ceramic hardness*. Springer, 1990.

[51] S.J. Bennison and B.R. Lawn. Role of interfacial grain-bridging sliding friction in the crack-resistance and strength properties of nontransforming ceramics. *Acta Metallurgica*, 37(10):2659 – 2671, 1989.

[52] G. Vekinis, M.F. Ashby, and P.W.R. Beaumont. R-curve behaviour of al_2o_3 ceramics. *Acta Metallurgica et Materialia*, 38(6):1151 – 1162, 1990.

[53] L.D. Monroe and J.R. Smith. Grain size dependence of fracture energy of y_2o_3. *Journal of American Ceramic Society*, 66:538–539, 1978.

[54] Walter Krenkel, editor. *Ceramic matrix composities: Fiber reinforced ceramics and their applications*. Wiley-VCH, 2008.

[55] Ceramic matrix composite, August 2011.

[56] E. Orowan. *Z. Physik*, 89:362, 1934.

[57] R. Becker and E. Orowan. *Z. Physik*, 79:566, 1932.

[58] V.A. Lubarda D.J. Benson E.M. Bringa M.A. Meyers, S. Traiviratana. The role of dislocations in the growth of nanosized voids in ductile failure of metals. *JOM*, 61(2):35–41, 2009.

[59] M.J. Mortimer R.O.A. Hall and D.A. Mortimer. Surface energy measurements on uo_2- a critical review. *Journal of Nuclear Materials*, 148(3):237 – 256, 1987.

[60] H. Miemczyk. Festelegun des elastizitätsmodul für uo_2. Technical Report 54.1529, IA-Notiz, 1974.

[61] V. Trimarco D. Marchi A.G. Leyva, D. Vega. Homogeneity characterisation of sintered $(u, gd)o_2$ pellets by x-ray diffraction. *Journal of Nuclear Materials*, 303:29–33, March 2002.

[62] H. H. S. Santana. Influence of the sintering atmosphere, the sintering time, and the annealing step on the mechanical resistance of uranium dioxide pellets. Master's thesis, University of Applied Sciences Aachen, May 2007.

[63] A. A. Griffith. The phenomena of rupture and flow in solids. *Philosophical Transactions of the Royal Society of London, Sereis A*, 221:163–198, February 1920.

[64] Fracture mechanics, August 2011.

[65] S. Ribeiro K. Strecker and M.-J. Hoffmann. Fracture toughness measurements of lps-sic: a comparison of the indentation technique and the sevnb method. *Materials Research*, 18(2):121–124, 2005.

[66] E. H. Toscano J. Spino, W. GOLL. Indentation techniques in nuclear applications: A review paper. *HOTLAB plenary Meeting*, pages 95–105, 2004.

[67] A. Tricoteaux D. Chicot. Mechanical properties of ceramics by indentation: Principle and applications. *Ceramic Materials*, pages 115–154.

[68] C. Ganguly T.R.G. Hutty, A.K. Sengupta. Indentation technique for mechanical property evaluation of ceramic nuclear fuels. *Nucl. Sci. Technol*, 7:1473–1486, 1990.

[69] P. Felines V. Basini, F. Bruguier. Indentation vickers sur combustibles uo_2 et uo_2 dopés. April 2004.

[70] J.E. Hart K. Radford, W.L. Lyon. Fluid-bed conversion of uf_6 to uo_2. *American Ceramic Society Bulletin*, 52:219–222, 1979.

[71] W.R. DeHollander and C.P. Fenimore. Process for producing uranium oxide rich compositions from uranium hexafluoride, May 1978.

[72] I. N. Toumanov. *Plasma and High Frequency Processes for Obtaining and Processing Materials in the Nuclear Fuel Cycle*. Nova Science Pub Inc, 2001.

[73] I.J. Urza. Conversion of uranium hexafluoride to uranium dioxide, May 1989.

[74] R. Warren C. H. Anderson. Silicon carbide fibers and their potential for use in composite materials, part 1. *Composities*, 15:16–23, 1984.

[75] G. Hondros. Evaluation of poisson ratio and the modulus of materials of low tensile resistance by the brazilian (indirect tensile) test with particular references to concrete. *Australian Journal of Applied Science*, 10(3):243 – 268, January 1959.

[76] T. Hasegawa J. Mazars Z.P. Bazant, M.T. Kazemi. Size effect in brazilian split-cylinder test: measurements and fracture. *ACI Materials Journal*, 88(3):332, 1991.

[77] Members ASCE G. M. Sabnis, S. M. Mirza. Size effects in model concretes. *Journal of the Structural Division*, 106(ST6):1007–1021, June 1979.

[78] R. L. Yuan W. F. Chen. Tensile strength of concrete: Double-punch test. *Journal of The Structural Division*, 106(ST8):1673–1693, August 1980.

[79] J. W. Tedesco C. Ross, P. Y. Thompson. Split-hopkinson pressure- bar tests on concrete and mortar in tension and compresion. *ACI Materials Journal*, 86(5):255–264, 1989.

[80] T. Okada T. Hasegawa, T. Shioya. Size effect on splitting tensile strength of concrete, proceedings. In *Japan Concrete Institute 7th Conference*, pages 309–312, 1985.

[81] H.M. Macleod and U. Marshall. The determination of density distribution in ceramic compacts using autoradiography. *Powder Technology*, 16(1):107 – 122, 1977.

[82] A. Michrafy, D. Ringenbacher, and P. Tchoreloff. Modelling the compaction behaviour of powders: application to pharmaceutical powders. *Powder Technology*, 127(3):257 – 266, 2002.

[83] D.C. Drucker and W. Prager. Soil mechanichs and plastic analysis or limit design. pages 22 –59, Nov 1951.

[84] A.N. Schofield and C.P. Wroth. *Critical state soil mechanics*. McGraw-Hill London, 1968.

[85] F.L. DiMaggio and I.S. Sandler. Material model for granular soils. *Journal of the Engineering Mechanics Division*, 97(3):935–950, June 1971.

[86] I. C. Sinka, J. C. Cunningham, and A. Zavaliangos. The effect of wall friction in the compaction of pharmaceutical tablets with curved faces: a validation study of the drucker-prager cap model. *Powder Technology*, 133(1-3):33 – 43, 2003.

[87] Alan C. F. Cocks. Constitutive modelling of powder compaction and sintering. *Progress in Materials Science*, 46(3-4):201 – 229, 2001.

[88] W.E. Smith. The need for non-destrutive testing of green p/m parts. *American Society of Manufacturing Engineers*, (EM70-580), 1970.

[89] H. Leuenberger and W. Jetzer. The compactibility of powder systems - a novel approach. *Powder Technology*, 37(1):209 – 218, 1984.

[90] M. Zemek. Influence of conversion of uf_6 to uo_2 powder and treatment on quality data of nuclear fuel. Master's thesis, Bratislava Technical University, 1999.

[91] C.T. de Freitas. *Uranium dioxide sintering kinetics and mechanisms under controlled oxygen potentials*. PhD thesis, Instituto de Energia Atômica, 1980.

[92] J.H. Yang K.S. Kim, K.W. Song. Effect os sintering gas on the grain size of uo_2 pellets derived from different powder routes. In IAEA International Atomic Energy Agency, editor, *Advanced fuel pellet materials and designs for water cooled reactors*, IAEA-TECDOC-1416, 2003.

[93] M. Peehs H. Assmann, W. Dörr. Control of uo_2 microstructure by oxidative sintering. *Journal of Nuclear Materials*, 140:1–6, April 1986.

[94] R. L. Coble. Sintering alumina: Efect of atmospheres. *Journal of the American Ceramic Society*, 45(3):123–127.

[95] Standard test methods for density of compacted or sintered powder metallurgy (pm) products using archimedes' principle. Technical report, ASTM B962-08, 2008.

[96] M. Coster J.-L. Chermant. Use of saltykov corrective method with a semi-automatic and automatic image analyzers. *Practical Metallography*, 14, 1977.

[97] T. Ishikawa J. Ishizaki H.Saitoh K. Yanai, M. Hirai. An analysis of density distribution in uo_2 green pellet by finite element method. *Journal of Nuclear Materials*, 257(3):318 – 330, 1998.

[98] M. Djuric et al. Particle size range as a influencing compressibility of ceramic powder. *Ceramics Internacional*, 21:227–230, 1995.

[99] M. Radeka Pedja Jovanic J. Ranogajec, M. Djuric. Influence of particle size and furnace atmosphere on the sintering of powder for tiles production. *Ceramics-Silikaty*, 44(2):71–77, 2000.

[100] L.G. Bunville. *Modern methods of particle size analysis*, page 28. Wiley, 1984.

[101] R. Demchak and E. Matijevic. Preparation and particle size analysis of chromium hydroxide hydrosols of narrow size distributions. *Journal of Colloid and Interface Science*, 31(2):257 – 262, 1969. Papers Presented at the 43rd National Colloid Symposium.

[102] J.W. Bauder G. Gee. *Methods of soil analysis. Part 1. Physical and mineralogical methods*, pages 383–411. American Society of Agronomy-Soil Science Society of America, 2nd edition, 1986.

[103] M. Kerker, E. Matijevic, W. F. Espenscheid, W. A. Farone, and S. Kitani. Aerosol studies by light scattering. i. particle size distribution by polarization ratio method. *Journal of Colloid Science*, 19(3):213 – 222, 1964.

[104] T. A. Kettler, John W. Doran, and T. L.. Gilbert. Simplified method for soil particle-size determination to accompany soil-quality analyses. *Publications from USDA-ARS / UNL Faculty*, 2001.

[105] Fluorite, June 2011.

[106] H. Bairiot, Y. Vanderborck, and G. Dumbruch. Performance-related characteristics of water reactor fuel. *Journal of Nuclear Materials*, 106(1-3):35 – 43, 1982.

[107] D.R. Lide, editor. *Handbook of chemistry and physics*. CRC Press, 1997-1998.

[108] P.H. Emmett S. Brunauer and E. Teller. Adsorption of gases in multimolecular layers. *Journal of the American Chemical Society*, 60(2):309–319, 1938.

[109] Determination of the specific surface area of solids by gas adsorption using the bet method. Technical report, ISO 9277:1995, 1995.

[110] E. Bertrand P. Sornay. Process for the manufacture of a particulate material and particulate material obtained by this process. Patent 20100032504, COMMISSARIAT A L'ENERGIE ATOMIQUE, 2010.

[111] Dilatometer, May 2011.

[112] D.L. Johnson H. Su. Master sintering curve: A practical approach to sintering. *Journal Am Ceramic Society*, 79(12):3211–3217, December 1996.

[113] D. Uskokovic S. Markovic. The master sintering curves for ba$ti_0.975sn_0.025o_3$/ba$ti_0.85sn_0.15o_3$ functionally graded materials. *Journal of the European Ceramic Society*, 29:2309–2316, 2009.

[114] D. Li H. Cao S. Zhang W. Shao, S. Chen. Construction of the master sintering curve for submicron size $\alpha - al_2o_3$ based on non-isothermal sintering containing lower heating rates only. *Materials Science-Poland*, 27(1):97–107, 2009.

[115] Test method for compressive (crushing) strength of fired whiteware materials. Technical report, ASTM C773-88, 2006.

[116] Test method for splitting tensile strength of cylindrical concrete specimens. Technical report, ASTM C496-96, 1996.

[117] A. Shukla, editor. *Dynamic Fracture Mechanics.* World Scientific Pub Co Inc, 2006.

[118] F. Jiang and K.S. Vecchio. Hopkinson bar loaded fracture experimental technique: A critical review of dynamic fracture toughness tests. *Applied Mechanics Reviews*, 62(6):39, 2009.

[119] J. Ródenas H. H. S. Santana, G. Maier. Ceramic nuclear fuel mechanical resistance development by means of dynamic impact testing. *Appl Radiat Isot.*, 68(8):1159–1161, 2010.

[120] D.Rittel A. Belenky, I.Bar-On. Static and dynamic fracture of transparent nanograined alumina. *Journal of the Mechanics and Physics of Solids*, 58(4):484–501, 2010.

[121] P.I.S. Peres. Determinacao do lote mínimo em ensaios de compressao diametral. *SBM*, pages 01 – 05, Setembro 2003.

[122] B. W. Darvell. Review uniaxial compression tests and the validity of indirect tensile strength. *Journal of Materials Science*, pages 757 – 780, 1990.

[123] F. L. L. B. Carneiro. Tensile strength of concrete. *RILEM Bulletin No. 13, Union of Testing and Research Laboratories for Materials and Structures*, 13:97–123, 1953.

[124] E.R. Hoskins J.C. Jaeger. Rock failure under the confined brazilian test. *JOURNAL OF GEOPHYSICAL RESEARCH*, 71(10):2651–2659, 1966.

[125] R. Berenbaum and I. Brodie. Measurement of the tensile strength of brittle materials. *British Journal of Applied Physics*, 10(6):281, 1959.

[126] H.L. Price and K.H. Murray. Finite element analysis of the diametral test of polymer moldings. *Journal of Engineering Materials and Technology*, 95(3):186–191, 1973.

[127] P. M. Braiden M. C. Shaw and G. J. Di Salvo. The disk test for brittle materials. *J . Engrg.for Ind.*, 96:77–87, 1975.

[128] U. W. Scherer J. Ródenas H. H. S. Santana, G. Maier. Analysis of mechanical strength in ceramic pellets of nuclear fuel. *Radiation Effects and Defects in Solids*, 164(5):313–318, May 2009.

[129] S.P. Timoshenko and J.N. Goodier. *Theory of elasticity.* McGraw-Hill New York, 1970.

[130] M.M. Frocht. *Photoplaticity. The selected scientific papers of M. M. Frocht.* John Wiley, 1947.

[131] Test method for splitting tensile strength for brittle nuclear waste forms. Technical report, ASTM C1144-89, 2004.

[132] C. Santos et al. A contribution of x ray diffraction analysis in the determination of creep of si_3n_4 ceramics. *Materials Research*, 9:1–8, March 2006.

[133] W. Weibull. A statistical distribution function of wide applicability. *Journal of Applied Mechanics*, 18:293–297, 1951.

[134] Advanced technical ceramics - mechanical properties of monolithic ceramics at room temperature - part 4: Vickers, knoop and rockwell superficial hardness. Technical report, DIN EN 843-4, 2005.

[135] Standard test method for vickers indentation hardness of advanced ceramics. Technical report, ASTM C1327-08, 2008.

[136] Hardness testing of ceramics, May 2011.

[137] J. B. Wachtman. *Ceramic films and coatings*. William Andrew, 1993.

[138] J. Vidal. *Nuclear Fuels with a Fine Grain Microstructure. Innovative Processes for High Plasticity and Strength*. PhD thesis, l'Université de Limoges, November 2012.

[139] J.P. Panakkal T.R.G. Kutty, K.N. Chandrasekharan and J.K. Ghosh. Fracture toughness and fracture surface energy of sintered uranium dioxide fuel pellets. *Journal of Materials Science Letters*, 6(3):260–262, 1987.

[140] R. Warren H. Matzke, T. Inque. *Journal of Nuclear Materials*, 91(205), 1980.

[141] A. S. Furzer J. Boocock and J. R. Matthews. *Report No. AERE - M 2565*, 1972.

[142] *Internation Symposium of Nuclear Fuels*. American Ceramic Society, 1969.

[143] R.H. Martinson W.M. Armstrong, W.R. Irvine. Creep deformation of stoichiometric uranium dioxide. *Journal of Nuclear Materials*, 7(2):133 – 141, 1962.

[144] J.P. Barnes B. Burton, G.L. Reynolds. The influence of grain size on the creep of uranium dioxide. *Journal of Materials Science*, 8:1690–1694, 1973.

Appendix A

Particle size distribution

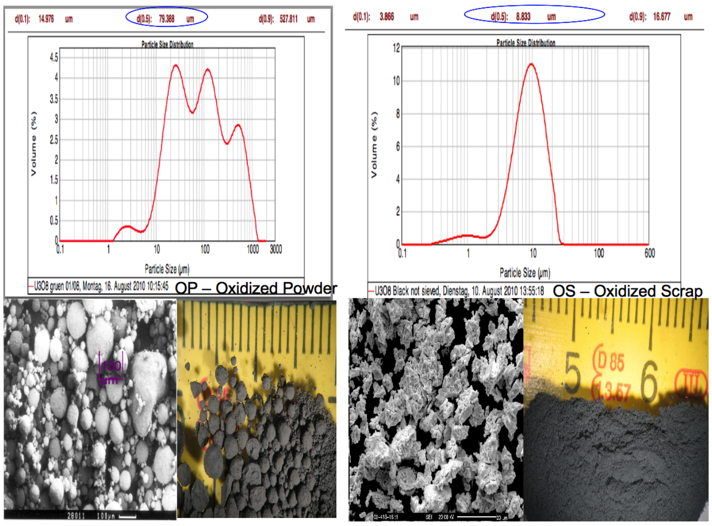

Figure A.1: Oxidized urania particle size distribution. On the left the oxidized powder is shown whereas on the right side the oxidized scrap particle size distribution is shown.

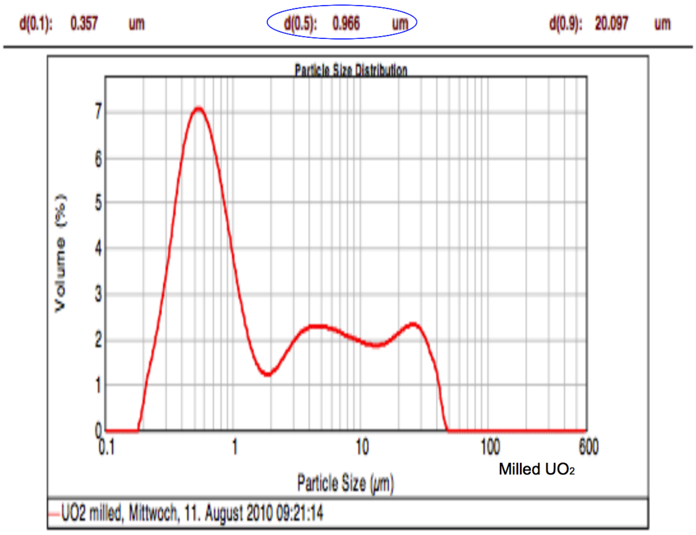

Figure A.2: Milled UO_2 particle size distribution.

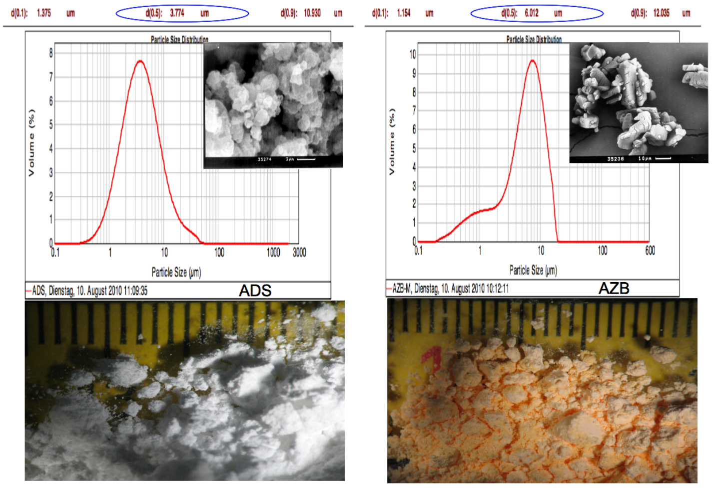

Figure A.3: $ADS$and AZB particle size distribution. SEM microsections are also presented.

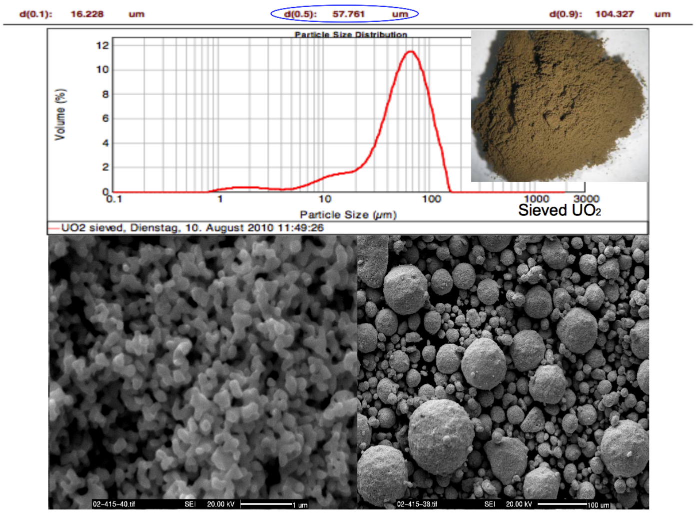

Figure A.4: Sieved UO_2 particle size distribution and SEM microsections.